The Pennsylvania State University

The Graduate School

IMPROVING TROPICAL CYCLONE FORECASTS FROM FORMATION TO MATURITY USING ENSEMBLE-BASED DATA ASSIMILATION

A Dissertation in

Meteorology and Atmospheric Science

by

Christopher Hartman

Submitted in Partial Fulfillment
of the Requirements
for the Degree of

Doctor of Philosophy

May 2024

The dissertation of Christopher Hartman was reviewed and approved by the following:

Xingchao Chen
Assistant Professor of Meteorology
Dissertation Advisor
Chair of Committee

Eugene E. Clothiaux
Professor of Meteorology and Atmospheric Science

Steven J. Greybush
Associate Professor of Meteorology
Associate Director, Center for Advanced Data Assimilation and Predictability Techniques
Co-Hire, Institute for Computational and Data Sciences

Manzhu Yu
Assistant Professor of Geography

Paul Markowski
Distinguished Professor of Meteorology
Department Head of Meteorology and Atmospheric Science

ABSTRACT

The studies comprising this dissertation use a state-of-the-art ensemble-based data assimilation (DA) system developed at The Pennsylvania State University to improve forecasts of tropical cyclones (TCs) during two of the least predictable stages of their lifecycle: formation (i.e., tropical cyclogenesis; hereafter TCG) and rapid intensification (RI). These improvements are realized by assimilating infrared (IR) brightness temperatures (BTs) observed by geostationary satellites under both clear and cloudy conditions. The all-sky IR BTs assimilated by the DA system help to constrain the initial moisture estimates within the core of the developing system in analyses via the strong ensemble correlations that exist between moisture content and simulated BTs. It is shown that forecasts initialized from these analyses exhibit a more realistic convective evolution, which translates to improved prediction of TCG and RI.

For the case of TCG, the assimilation of upper-tropospheric water vapor channel BTs observed by the Meteosat-10 Spinning Enhanced Visible and InfraRed Imager (SEVIRI) instrument improves the timing of TCG in forecasts of Hurricane Irma (2017). In an experiment that withheld the BTs, TCG was premature by at least 24 hours due to an overestimation of the spatial coverage of deep convection within the African Easterly Wave (AEW) that Irma formed from. Spurious convection led to stronger low-level convergence and the earlier spin-up of a low-level meso-β-scale (i.e., 20 – 200 km) vortex. This was ameliorated by assimilating all-sky IR BTs. Furthermore, the substantial impact of initial moisture uncertainty within the incipient disturbance is revealed by initializing ensemble forecasts with only the initial moisture perturbations retained. Relative to an ensemble with initial perturbations to all variables, at least half of the intensity forecast uncertainty is attributed to initial moisture uncertainty within the AEW. These results show the importance of targeting the incipient disturbance with high spatio-temporal water vapor observations for ingestion into DA systems.

For the case of RI, the assimilation of upper-tropospheric water vapor channel BTs observed by the GOES-16 Advanced Baseline Imager (ABI) led to significant improvements in the intensity forecasts of Hurricane Dorian (2019) at lead times of 48 hours and longer. These improvements are shown to be a result of better analyzed cloud fields as well as more intense initial primary and secondary circulations. Despite these improvements, the vortex exhibited an unrealistically broad structure that was fine-tuned by the additional assimilation of tail Doppler radar (TDR) radial velocities collected by NOAA P-3 aircraft. The simultaneous assimilation of all-sky IR BTs and radar observations therefore resulted in realistic forecasts of the track, structure, and RI of Dorian. These results underscore the potential of TDR observations to complement the benefits gained by assimilating all-sky IR BTs.

TABLE OF CONTENTS

List of Figures

List of Acronyms and Symbols

ABEI: Adaptive Background Error Inflation

ABI: Advanced Baseline Imager

AEW: African Easterly Wave

AMV: Atmospheric Motion Vector

AOEI: Adaptive Observation Error Inflation

BT: Brightness Temperature

CRTM: Community Radiative Transfer Model

CSF: Column Saturation Fraction

DA: Data Assimilation

DKE: Difference Kinetic Energy

EnKF: Ensemble Kalman Filter

EnSRF: Ensemble Square Root Filter

GFS: Global Forecast System

GPM: Global Precipitation Measurement

GTS: Global Telecommunications System

HCC23: Hartman, Chen, and Chan 2023 (i.e., Hartman et al. 2023)

HPI: Hurricane Position and Intensity

HRD: Hurricane Research Division

HWRF: Hurricane Weather Research and Forecasting

IR: InfraRed

MAE: Mean Absolute Error

MCS: Mesoscale Convective System

MCV: Mesoscale Convective Vortex

METAR: METeorological Aerodrome Report

MW: MicroWave

NCEP: National Centers for Environmental Prediction

NHC: National Hurricane Center

OFCL: Official Forecast of the National Hurricane Center

OmF: Observation minus Forecast

NCAR: National Center for Atmospheric Research

PRIMER: Pouch-Relative Initial Moisture Ensemble-perturbation Reduction

PSU: Pennsylvania State University

Q_v: Water vapor mixing ratio

QVAPOR: Water vapor mixing ratio

RI: Rapid Intensification

ROI: Radius Of Influence

RMW: Radius of Maximum Wind

RRTM: Rapid Radiative Transfer Model

SCL: Successive Covariance Localization

SFMR: Stepped Frequency Microwave Radiometer

SEVIRI: Spinning Enhanced Visible and InfraRed Imager

SLP: Sea Level Pressure

TC: Tropical Cyclone

TCG: Tropical Cyclogenesis

TDR: Tail Doppler Radar

VHT: Vortical Hot Tower

WMO: World Meteorological Organization

WRF: Weather Research and Forecasting

Preface

This dissertation is a compilation of publications where Christopher Hartman is the lead author. Christopher gratefully acknowledges the co-authors of these journal articles. Some figures and text have been modified slightly where appropriate. Below is the list of references for the two published articles and the one that is currently under review, along with the chapter of this dissertation they can be found within.

Chapter 2:

Hartman, C.M., X. Chen, and M.-Y. Chan, 2023: Improving Tropical Cyclogenesis Forecasts of Hurricane Irma (2017) through the Assimilation of All-Sky Infrared Brightness Temperatures. *Mon. Weather Rev.*, **151**, 837-859, https://doi.org/10.1175/MWR-D-22-0196.1.

Chapter 3:

Hartman, C.M., F. Judt, and X. Chen (under review): Influence of Local Water Vapor Analysis Uncertainty on Ensemble Forecasts of Tropical Cyclogenesis Using Hurricane Irma (2017) as a Testbed. *Mon. Weather Rev.*

Chapter 4:

Hartman, C.M., X. Chen, E.E. Clothiaux, and M.-Y. Chan, 2021: Improving the Analysis and Forecast of Hurricane Dorian (2019) with Simultaneous Assimilation of *GOES-16* All-Sky Infrared Brightness Temperatures and Tail Doppler Radar Radial Velocities. *Mon. Weather Rev.*, **149**, 2193-2212, https://doi.org/10.1175/MWR-D-20-0338.1.

Acknowledgements

As I write this dissertation, I realize how very much I am grateful to:

- Xingchao Chen … for his patience.
- Eugene Clothiaux, Steven Greybush, and Manzhu Yu … for their guidance.
- Fuqing Zhang … for giving me the opportunity of a lifetime.
- Jerry Harrington and Hans Verlinde … for believing in me.
- Zhu ("Judy") Yao … for making me laugh.
- Scott Sieron … for not killing me.
- My parents … for pointing out my passion for Meteorology.
- My funding sources (see below) … for keeping me fed.
- Pumpkin … for keeping me sane.
- Most of all, my husband Man Yau Chan … for making me the happiest man alive!

Funding for this dissertation work was provided by:

- ONR Grant N00014-18-1-2517
- NASA Grant 80NSSC22K0613
- NOAA Grant NA18NWS4680054
- NGGPS and HFIP through Subcontract 3004628721 with the University of Michigan
- U.S. Department of Energy, Office of Science, Biological and Environmental Research, as part of the Regional and Global Climate Modeling program.

Any opinions, findings, conclusions, or recommendations expressed in this publication are those of the authors and do not necessarily reflect the views of ONR, NASA, NOAA, NGGPS, HFIP, or the U.S. Department of Energy.

The experiments and analysis in this dissertation were done on the Stampede2 supercomputer at the Texas Advanced Computing Center (TACC).

Chapter 1

Introduction

1.1 Background and Motivation

Tropical cyclones (TCs) have caused more fatalities and impacted the economy more than any other billion-dollar weather-related disaster in the United States since 1980 (Smith 2020). At the same time, intensity and tropical cyclogenesis (TCG) forecasts of TCs were quite slow to improve (Cangialosi 2020). We therefore must improve our forecasts of these phenomena so that the public can be better informed. The goal of this dissertation research is to improve forecasts of TCs during two of the most intractable stages of their lifetime: 1) TCG and 2) rapid intensification (RI). RI is defined as an intensification rate exceeding 15 m s^{-1} in a 24 hour period (Kaplan and DeMaria 2003) and TCG is typically defined as the formation of a tropical depression from a pre-existing tropical disturbance. The complexity of these stages has limited our understanding of them and challenged our ability to predict them.

Our understanding of TCG, especially the precise mechanisms by which a cold-core mid-level vortex transforms into a warm-core low-level vortex that eventually becomes a TC, is incomplete at best. While TCs appear to form from multiscale interactions between a pre-existing synoptic-scale disturbance and convection within the disturbance, it is still not entirely clear how. Ritchie and Holland (1997) and Simpson et al. (1997) proposed that the mesoscale convective vortices (MCVs) in the stratiform region of mesoscale convective systems (MCSs) collectively reinforce the mid-level circulation of the larger-scale disturbance. This mid-level circulation was believed to subsequently lower toward the surface via evaporatively-cooled downdrafts, thereby leading to TCG (Bister and Emanuel 1997). This theory, referred to as the "top-down" pathway, was formulated based on observations from then recent field campaigns of

the early 1990s. Unfortunately, the "top-down" pathway did not provide a convincing argument for how the mid-level vortex lowered toward the surface since a downward transport of vertical vorticity is an apparent violation of the laws of fluid dynamics (Raymond et al. 2011). Eventually, the "top-down" hypothesis was abandoned in favor of the "bottom-up" hypothesis, whereby the low-level tropical depression vortex is built by the successive merging of convective towers containing strong cyclonic vorticity anomalies named "vortical" hot towers (VHTs; Hendricks et al. 2004; Montgomery et al. 2006). This insight was made possible by cloud-resolving simulations and was reinforced by several modeling studies (e.g., Tory et al. 2006a,b; Shin and Smith 2008; Van Sang et al. 2008; Braun et al. 2010). Observational studies around that time (Reasor et al. 2005; Sippel et al. 2006; Houze et al. 2009) also documented the prevalence of VHTs. Although the "top-down" versus "bottom-up" debate had seemingly been laid to rest, our understanding of the specific role of the mid-level vortex remained unclear.

The two main competing theories in contemporary literature for how the warm-core low-level vortex forms and becomes a TC disagree over the role of the mid-level vortex. These two competing theories, both of which support a "bottom-up" pathway to TCG, are depicted in the schematic diagram of Figure 1.1. In the first theory (Figure 1.1a), the mid-level vortex plays an instrumental role in TCG by promoting low-level spin-up (Raymond et al. 2011; Gjorgjievska and Raymond 2014). The aforementioned observational studies argue that the mid-level circulation contained within the stratiform precipitation region of MCSs increases the static stability of the troposphere through thermal wind balance. The increased static stability, they contend, favors a bottom-heavy mass flux profile and horizontal convergence of mass at low levels due to continuity. With greater horizontal convergence of mass, the circulation at low levels is increased to the point of TCG. Competing with this theory is the notion that the mid-level vortex merely plays a supporting role in the spin-up of the low-level vortex (Figure 1.1b). This concept was hinted at by Nolan (2007) and Houze et al. (2009) when pointing out that the mass flux profile at low levels is dominated by VHTs. More recently, Bell and Montgomery (2019) used observations of pre-Karl (2010) to argue how the mid-level vortex merely supports the development of the low-level vortex. In that study, they paint a picture of TCG as an episodic building of both the low and mid-level vortices via a positive feedback loop (Figure 1.1b). In that feedback loop, deep convective bursts add moisture to the mid-levels while increasing the low-

level circulation through the horizontal advection, and subsequent stretching, of vertical vorticity. Once the deep convection matures, a stratiform precipitation region forms within the MCSs that promotes a strengthening of the mid-level vortex. This mid-level vortex helps protect the mid-level moisture from lateral intrusions of dry air. At the same time, the low levels are moistened by the evaporation of precipitation. With a higher column saturation fraction (CSF), the troposphere is primed for a new round of deep convection. Eventually, the low-level vortex strengthens to the point of TCG. In the future, more detailed case studies of developing and non-developing storms are necessary to determine the specific role of the mid-level vortex. Until then, it remains a point of contention.

Regardless of the precise mechanisms by which convection leads to a TC, the community's consensus is that convective-scale processes play an important role in TCG. Accurately predicting TCG is a very difficult but exciting problem. At this point in time, operational guidance provided by the National Hurricane Center (NHC) only predicts the probability of TCG within favorable regions over the next two and five days. The reliance on probabilities is testament to this challenge. Even with a seedling disturbance present within a favorable environment, accurate predictions of TCG timing elude the community. This problem stems from the fact that TCG is intimately determined by the intricacies of moist convective processes and their nonlinear interactions with the proto-vortex they are embedded within (Emanuel 2018; Tang et al. 2020; Núñez Ocasio 2021). More specifically, when latent heating from moist convection overlaps with low-level vorticity maxima within the proto-vortex, VHTs can form (Hendricks et al. 2004; Montgomery et al. 2006). The subsequent aggregation of these rotating plumes ultimately forms the TC vortex. Without an accurate representation of the spatial pattern of the initial low and mid-level moisture concentration with respect to the low-level vorticity maxima, this process will not be adequately captured. Moreover, these small-scale convective differences, which begin as position errors of individual convective cells, can quickly grow upscale to contaminate the vortex-scale flow (Zhang et al. 2003; Tan et al. 2004; Zhang et al. 2007; Sun and Zhang 2016). Consequently, accurate TCG forecasts require a realistic representation of the initial moisture content for input to models. Unfortunately, there is a dearth of moisture observations over the open ocean where TCs form. This is a major hindrance to the accurate initialization of TCG forecasts, which ultimately degrades their quality.

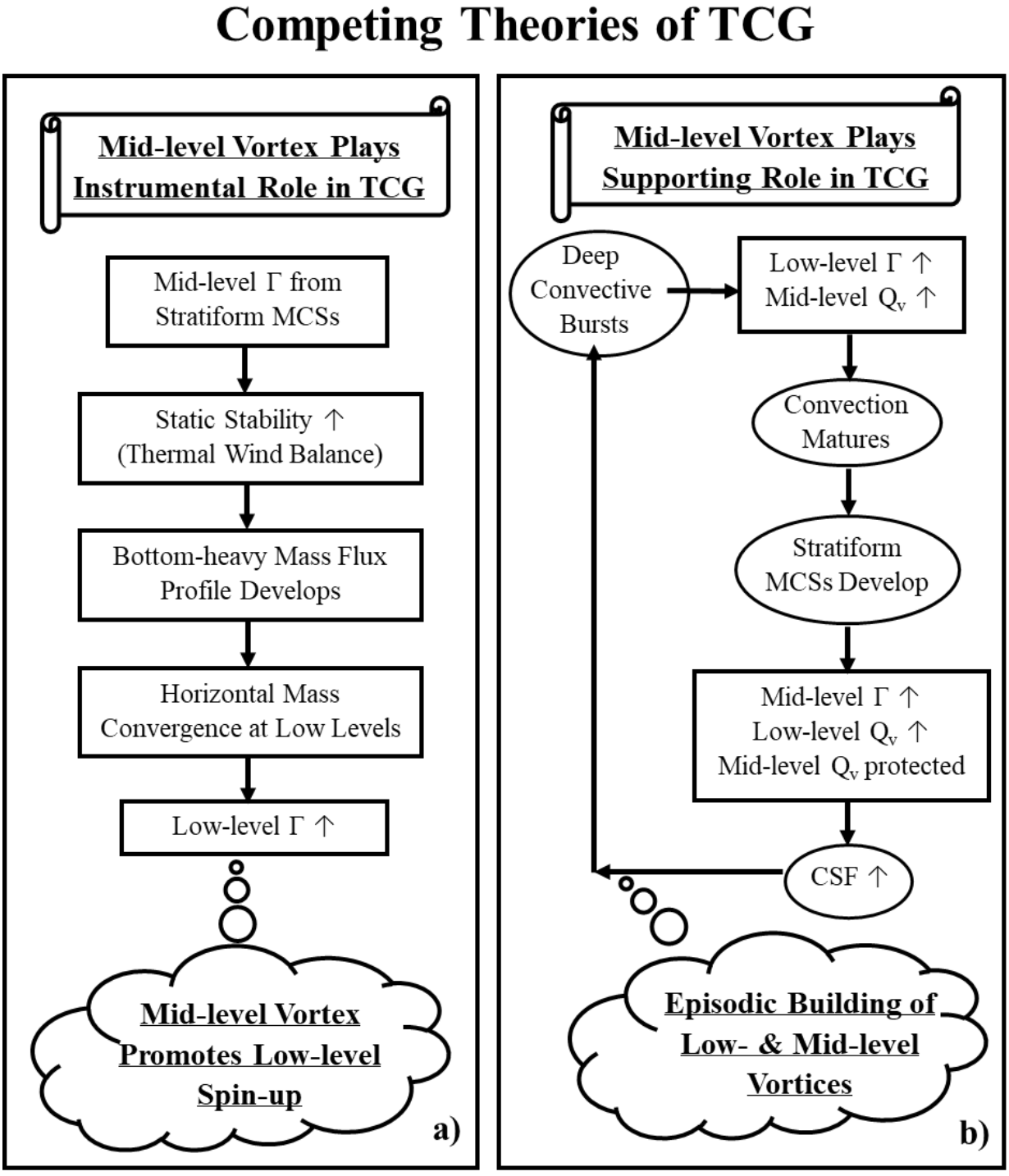

Figure 1.1. Schematic diagram showing the two competing theories of the relative roles of the low and mid-level vortices in TCG. In (a), the mid-level vortex plays an instrumental role in TCG by promoting low-level spin-up while in (b) the mid-level vortex merely plays a supporting role. See text for more details.

The limitations imposed by moist convective processes extend to the subsequent intensification of TCs, especially ones that undergo RI. For example, small uncertainties in the initial moisture content can quickly and chaotically grow to vortex-scale convective asymmetries (Van Sang et al. 2008; Taraphdar et al. 2014). These convective asymmetries affect the vertical tilt of the vortex, which influences the vortex-scale flow and subsequent convection (Jones 1995; Corbosiero and Molinari 2002; Hence and Houze 2011; Reasor et al. 2013; DeHart et al. 2014). If, and when, the vortex will align depends on the complicated nonlinear interactions between the vortex-scale flow and convection. In the presence of moderate vertical wind shear, this can be a major limiting factor in the predictability of RI timing (Zhang and Tao 2013; Tao and Zhang 2014; Judt and Chen 2016). Based on the sensitivity of RI forecasts to moist convective processes, it is not surprising that multiple studies have stressed the importance of accurate initialization of inner-core moisture within TCs that are about to rapidly deepen (e.g., Emanuel and Zhang 2017; Minamide and Zhang 2018; Minamide et al. 2020). Unfortunately, there is a lack of inner-core moisture observations within developing TCs (Pu et al. 2016). This is limiting our ability to accurately predict RI.

To improve both TCG and RI forecasts, this dissertation will investigate the potential of using another observation type to constrain the initial conditions for forecasts: IR BTs observed by geostationary satellites under all-sky (i.e., both clear and cloudy) conditions. These underutilized observations have been shown to improve the forecasts of RI in case studies (e.g., Zhang et al. 2016; Honda et al. 2018; Minamide and Zhang 2018; F. Zhang et al. 2019); however, it is important to confirm the robustness of these results with other storms. Furthermore, no studies to date have explored the potential of all-sky IR BTs to improve the forecasts of TCG.

1.2 Overarching Methodology

To reduce the initial condition uncertainty in forecasts, this dissertation makes use of an ensemble-based DA system known as The Pennsylvania State University (PSU) ensemble Kalman filter (EnKF) system (hereafter PSU-EnKF). This system has been used to assimilate operationally-available observations since 2008 (Meng and Zhang 2008). The EnKF (Evensen 1994) translates information contained within observations to state variable updates through

error covariances that are estimated by a forecast ensemble. Since this ensemble evolves with time, the EnKF can capture the "errors of the day" (i.e., it is flow-dependent). By weighing the relative uncertainty of the state variable being updated against the uncertainty of the observation being assimilated, the EnKF provides an analysis with less uncertainty than both the observation and the original values of the state variable. This analysis can then be used to initialize forecasts.

Although the EnKF has been around for quite some time, the ability to assimilate all-sky IR BTs is a relatively new and novel concept. As a matter of fact, this observation type is not yet assimilated by any operational center, mostly due to the challenges of assimilating cloudy-sky BTs. Perhaps the biggest challenge that comes with assimilating cloudy-sky BTs is the situation in which the observed cloud scene for a column is cloudy, but the ensemble mean is simulated to be clear. In that situation, the DA system has trouble producing clouds in the analysis because the covariances between hydrometeor mixing ratios and simulated BTs are zero. The zero covariance is a result of the fact that both the ensemble mean and perturbations (i.e., difference from the ensemble mean) of the hydrometeor mixing ratios are zero in this situation because the presence of a nonzero hydrometeor mixing ratio value for any one member would turn the ensemble mean value nonzero. Consequently, the hydrometeor mixing ratios cannot be updated by the EnKF in this situation, since the EnKF uses a form of linear regression that is based on the error covariances. The PSU-EnKF handles this issue by employing an adaptive inflation technique that is described in chapter 2. Another major challenge of assimilating cloudy-sky BTs is the representativeness errors that can easily develop due to a mismatch between the observed and simulated cloud scene (either spuriously modeled clear-sky columns or spuriously modeled cloudy-sky columns). In other words, clouds have distinct edges. A slight displacement of the modeled cloud edge relative to observations can cause a large difference between the simulated and observed BT value for that location. Consequently, this large "innovation" can shock the DA system if not handled appropriately. The PSU-EnKF is currently able to reduce the shock of such situations by employing another adaptive inflation technique that is described in chapter 2. In summary, the DA system used in this dissertation has the capability to assimilate BTs observed under both clear and cloudy conditions. Its novelty is its ability to reduce the negative side effects oftentimes associated with cloudy-sky observations.

1.3 Dissertation Overview

This dissertation is composed of three main chapters, each of which contains a detailed literature review in its introduction. In chapter 2, the potential improvements brought to TCG forecasts by assimilating all-sky IR BTs is explored in the context of Hurricane Irma (2017), a classic Cape Verde storm. Chapter 3 extends the work of chapter 2 by assessing the gains that can be brought to TCG forecasts through the further reduction of initial moisture uncertainty in ensemble forecasts of Irma. In chapter 4, the improvement brought to RI forecasts by assimilating all-sky IR BTs is evaluated in the context of Hurricane Dorian (2019). The additional value brought to RI forecasts by simultaneously assimilating the all-sky IR BTs with TDR radial velocity observations collected by NOAA P-3 aircraft is also quantified. Finally, the dissertation ends with a conclusion that summarizes the main findings of these chapters, points out their limitations, and suggests directions for future research.

Chapter 2

Improving Tropical Cyclogenesis Forecasts of Hurricane Irma (2017) through the Assimilation of All-Sky Infrared Brightness Temperatures

ABSTRACT

The assimilation of satellite all-sky IR BTs has been shown in previous studies to improve intensity forecasts of TCs. In this study, the potential of assimilating all-sky IR BTs to improve TCG forecasts by constraining the pre-TCG cloud and moisture fields is explored. By using an ensemble-based DA system, it is shown that the assimilation of upper-tropospheric water vapor channel BTs observed by the Meteosat-10 SEVIRI instrument two days before the formation of a tropical depression improves the TCG forecast of Hurricane Irma (2017), a classic Cape Verde storm, by up to 24 hours while also capturing its later RI in deterministic forecasts. In an experiment that withholds the assimilation of all-sky IR BTs, the assimilation of conventional observations from the Global Telecommunications System (GTS) leads to the pre-mature TCG of Hurricane Irma by at least 24 hours. This pre-mature TCG is shown to result from an overestimation of the spatial coverage of deep convection within the AEW from which Irma eventually forms. The gross overestimation of deep convection without all-sky IR BTs is accompanied by higher CSF, stronger low-level convergence, and the earlier spin-up of a low-level meso-β-scale vortex within the AEW that ultimately becomes Hurricane Irma. Through its adjustment to the initial moisture and cloud conditions, the assimilation of all-sky IR BTs leads to a more realistic convective evolution in forecasts and ultimately a more realistic timing of TCG.

2.1 Chapter Introduction

The formation of a tropical depression from a pre-existing tropical disturbance (i.e., TCG) is an inadequately understood phenomenon. Details of this early stage in the lifecycle of a TC have been challenging to uncover and forecast due to 1) difficulties in understanding the complex nonlinear interactions that occur across scales ranging from the convective up to synoptic scales (Emanuel 2018; Tang et al. 2020; Núñez Ocasio 2021), and 2) a lack of in-situ observations over the open ocean.

The environmental conditions favorable for TCG have been known for years. Aside from high sea surface temperatures, these conditions include low vertical wind shear, plentiful mid-level moisture, and high vertical instability (Gray 1968; DeMaria et al. 2001). Observational studies have also pointed out that TCG is usually related to a pre-existing synoptic-scale tropical disturbance (e.g., Reed et al. 1977; Gray 1968; Briegel and Frank 1997; Ritchie and Holland 1997). For example, the most common synoptic-scale disturbance involved in the TCG of Atlantic TCs is the AEW – at least 70% of Atlantic TCs form in association with AEWs (Russell et al. 2017). In short, it is possible to locate approximate preferred regions of TCG based on the large-scale environmental conditions and pre-existing synoptic-scale tropical disturbances.

The strong association between AEWs and TCG is particularly interesting. Dunkerton et al. (2009) proposed that TCG preferentially occurs in regions where the lower-tropospheric AEW-relative streamlines exhibit a closed circulation (specifically, the center of this meso-α-scale (i.e., 200 – 1000 km) circulation, also known as the "marsupial pouch", or "pouch" in short). Their reasoning is that the pouch not only provides a region of cyclonic rotation and weak strain/shearing deformation, but also protects the tropical disturbance within it from potentially harmful environmental conditions (e.g., dry air intrusion). This "marsupial pouch" paradigm has gained traction over the last decade as it has been reinforced by multiple modeling studies (e.g., Wang et al. 2010; Li and Pu 2014; Asaadi et al. 2016, 2017; Rajasree et al. 2016a,b) and field campaigns, including the Tropical Cyclone Structure 2008 field experiment (TCS-08; Montgomery et al. 2010), the Pre-Depression Investigation of Cloud-Systems in the Tropics experiment (PREDICT; Montgomery et al. 2012), and NASA's Genesis and Rapid

Intensification Processes field experiment (GRIP; Braun et al. 2013). Ultimately, the "marsupial pouch" paradigm adds extra layers of complexity to the "bottom-up" pathway of TCG described in chapter 1.

Despite our ability to locate probable areas of TCG (i.e., areas along the forecasted AEW track that have favorable large-scale environments), it is still an unmet challenge to accurately forecast whether the TCG will happen and/or the exact TCG timing. This is due to uncertainties in convective-scale processes and their nonlinear interactions with the vortex they are embedded within. As detailed in chapter 1, it is still not entirely clear how a mid-level cold-core vortex transforms into a low-level warm-core vortex that eventually spins-up to form a TC.

Given the important role convection plays in the TCG process, it stands to reason that we must adequately capture its evolution in forecasts if we wish to accurately predict the timing of TCG. Over the last decade, studies have investigated potential connections between the temporal evolution of spatial patterns of convection in pre-depression tropical disturbances and subsequent TCG. Reanalysis-based (Leppert et al. 2013a,b) and observation-based (Zawislak and Zipser 2014) studies have suggested that the convective intensity near the circulation center might be much less of a factor than the convective area in the hours and days leading up to TCG. Wang (2018) stressed the importance of looking at the spatial pattern of convection in TCG studies – they observed that TCG was more likely to occur when convective intensity increased in the inner pouch region but stayed the same or decreased in the outer pouch region in the hours leading up to TCG. The spatial pattern and evolution of multiday convective bursts was analyzed in several recent observational studies (Kerns and Chen 2013; Chang et al. 2017; Bell and Montgomery 2019). These studies indicate that vigorous multiday convective bursts that are conducive to TCG occur in both developing and non-developing disturbances. These studies collectively reinforce the notion that the occurrence of TCG has a complicated dependence on pre-TCG convection.

Since the convective evolution of pre-TCG disturbances is quite complex, the accurate prediction of TCG depends on an accurate representation of it. Since in-situ and aircraft observations are sparse over the open ocean, one way to achieve a better representation of convection in forecasts is to assimilate high resolution (>1 pixel 30-km^{-2}) all-sky IR BTs. At this

point in time, a number of real-data studies have shown the benefits of assimilating all-sky IR BTs in the forecasts of severe thunderstorms (e.g., Zhang et al. 2018, 2021b; Sawada et al. 2019; Jones et al. 2020), tropical convection (e.g., Chan et al. 2020b; Chan and Chen 2022), and TC RI (e.g., Honda et al. 2018; Minamide and Zhang 2018; F. Zhang et al. 2019; Minamide et al. 2020; Hartman et al. 2021). These studies unanimously found that the assimilation of all-sky IR BTs improved the evolution of clouds in forecasts. It is thus possible that assimilating all-sky IR BTs could improve TCG forecasts.

In this study, this possibility is examined in the context of Hurricane Irma (2017). This storm was chosen because it is a classic Cape Verde storm that ultimately impacted many areas in the Caribbean and continental United States. In addition, this particular storm formed well before the expectation of NHC operational guidance (Cangialosi et al. 2018).

This chapter is organized as follows. Section 2 provides a brief meteorological history of Irma and section 3 describes the experimental setup and DA system used. The results of deterministic forecasts initialized with the DA system are presented in section 4. Finally, the conclusions of this study and avenues of future research are presented in section 5.

2.2 Brief Overview of Hurricane Irma (2017)

Before proceeding, a brief description of Hurricane Irma (2017) is warranted. As a classic Cape Verde storm, Hurricane Irma formed from an AEW that moved into the eastern Atlantic Ocean late in the day on 27 August. On that day, despite favorable environmental conditions, the operational NHC guidance projected no chance of TC development over the next 48 hours and a 20% chance of TC development over the next 5 days. At 00 UTC 28 August (48 hours before TCG), these probabilities were relatively unchanged even though deep convection persisted within the northern portion of the wave trough (Figure 2.1a). Over the next 48 hours this deep convection organized (Figure 2.1b) faster than anticipated, and by 00 UTC 30 August (hereafter "TCG time") the NHC classified the resulting convective system as a tropical depression when a well-defined surface circulation was detected.

The track and intensity of Irma after TCG are shown for reference in Figures 2.1e and 2.1f, respectively. After forming roughly 150 miles west of the Cabo Verde Islands, it moved westward into favorable environmental conditions and underwent RI. Irma became a hurricane within the next 30 hours and a major hurricane within 48 hours. The cloud fields and lower tropospheric streamlines are shown during RI (Figure 2.1c) and at major hurricane stage (Figure 2.1d). These subplots illustrate the axisymmetrization of the convection that occurred within the increasingly well-defined low-level vortex during Irma's path to maturity.

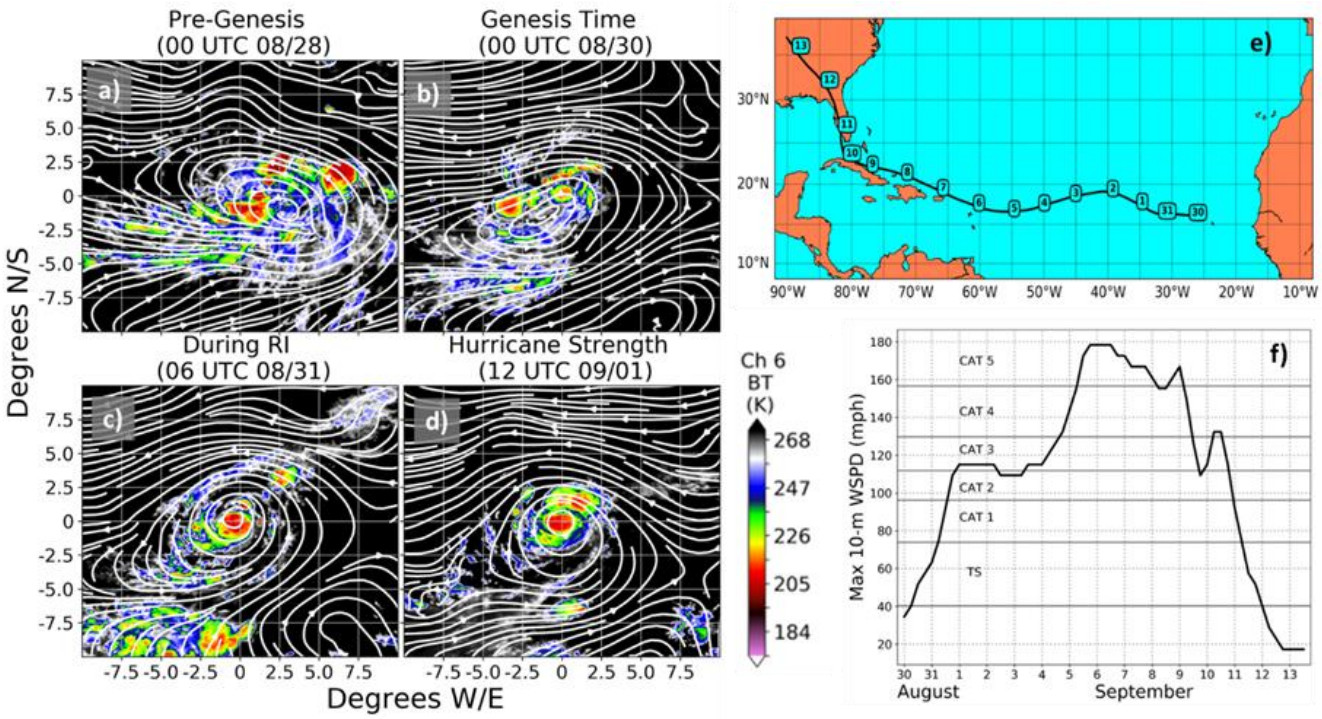

Figure 2.1. Meteosat-10 Ch 6 BT overlayed with ERA5 850-hPa streamlines of Irma (a) 48 hours pre-TCG (00 UTC 28 August), (b) at TCG time (00 UTC 30 August), (c) during RI (06 UTC 31 August), and (d) at major hurricane strength (12 UTC 01 September). Also shown is the (e) track and (f) maximum 10-m wind speed of Irma from the NHC HURDAT2 database starting from TCG time. Note that for this study TCG time (00 UTC 30 August) is defined as the first occurrence of a tropical depression in the HURDAT2 database. Numbers within rounded squares in (e) represent the day of the month.

This study will focus on improving deterministic forecasts initialized during a 12-hour period centered on 48 hours pre-TCG. This period (from 18 UTC 08/27 to 05 UTC 08/28) was chosen because the operational NHC guidance called for low probabilities of development over the next 48 hours (0%) to 5 days (< 50%), which indicates a low practical predictability of TCG during this period. Although the focus of this study is on TCG, the impacts of assimilating all-sky IR BTs on the later RI of Irma will also be examined.

2.3 Methodology

This section describes the DA system and forecast model used, the experimental design, and the observations assimilated.

2.3.1 DA and Forecast System

The DA system used for this study is the PSU-EnKF system. This system converts observations into model state variable updates using the ensemble square root filter (EnSRF) of Whitaker and Hamill (2002). The ensemble is then integrated to the next DA analysis time point using the Advanced Research version of the Weather Research and Forecasting (WRF) Model version 3.6.1 (Skamarock et al. 2008). The PSU-EnKF system has been used for real-data case studies since 2008 (Meng and Zhang 2008). For ease of parallelization, it performs DA in a joint state-observation space (Tarantola 1987; Anderson 2001) using the high latency parallel implementation of Anderson and Collins (2007). Sixty ensemble members were used in this study and 80% relaxation to prior perturbations (Zhang et al. 2004) was applied to avoid filter divergence. Finally, the Community Radiative Transfer Model (CRTM; Han et al. 2006, 2007; Weng 2007) version 2.1.3 served as the observation operator when assimilating all-sky IR BTs.

Throughout this study, the WRF model was applied on a single stationary domain with a 9-km horizontal grid spacing over the area indicated by the black rectangle in Figure 2.2b. This domain size (865 grid points in the east-west direction and 371 grid points in the north-south direction) was chosen to ensure that it was large enough to contain both the storm and its parent AEW, and to reduce the potential impacts of boundary effects. The 9-km spacing was chosen as a compromise between the model domain size and horizontal resolution. In the vertical, there

were 43 model levels extending to 10 hPa. Parameterization schemes used include: the Thompson double-moment microphysics scheme (Thompson et al. 2008), the Yonsei University planetary boundary layer scheme (Hong et al. 2006); and the Rapid Radiative Transfer Model (RRTM) longwave and shortwave radiation schemes (Iacono et al. 2008). Finally, surface fluxes of momentum, as well as sensible and latent heat, were parameterized following Green and Zhang (2013).

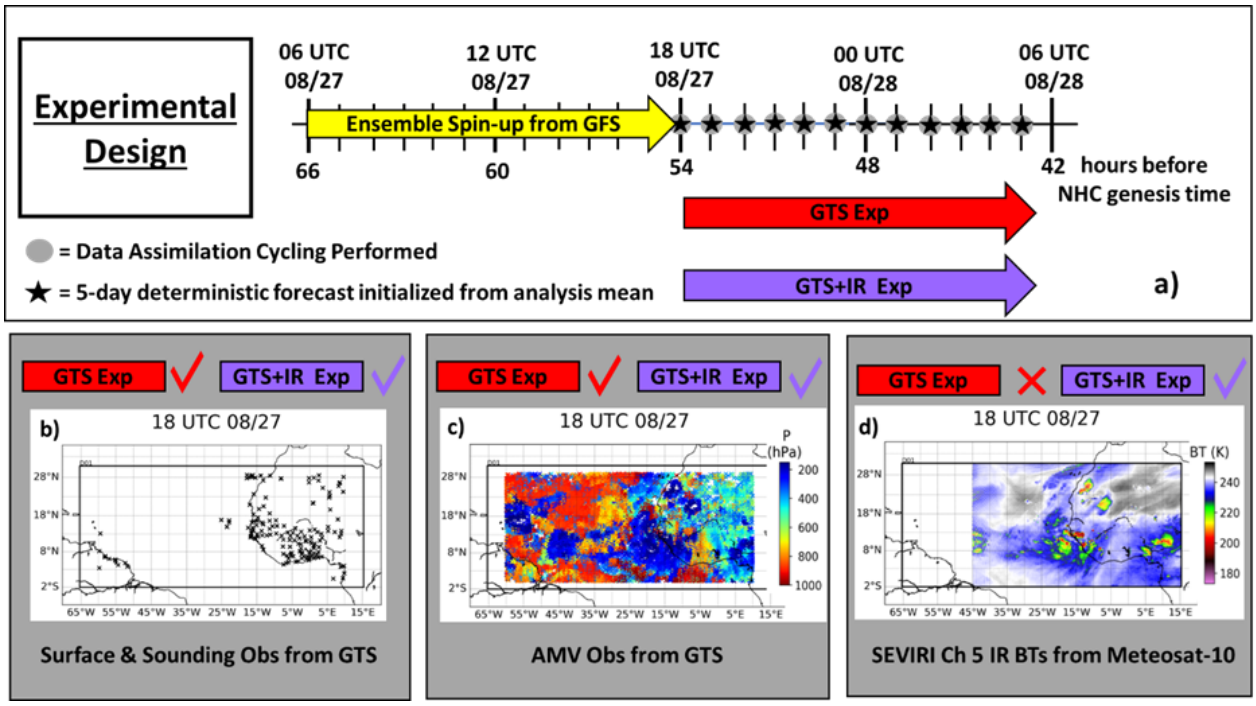

Figure 2.2. (a) Overview of the experimental design including (b-d) the locations of each type of observation assimilated during the first DA cycle. See text for more details.

No cumulus parameterization scheme was used in this study. While the 9-km grid spacing used here cannot well resolve individual convective cells, previous studies have shown that such a gray-zone grid spacing is capable of resolving MCSs and TCs without using a cumulus parameterization scheme (e.g., He et al. 2019; Wang et al. 2015; Ying and Zhang 2018; J. Zhang et al. 2017; Chen et al. 2018a,b; Chen and Zhang 2019; Ying and Zhang 2017; Chan et al. 2020b; Ou et al. 2020; Chen et al. 2021a,b; Chan and Chen 2022; Chen et al. 2022a,b).

Recent studies also indicate that regional simulations using such a grid spacing can capture the primary physical processes related to TCG (e.g., Montgomery et al. 2010b) and MCS energetics (e.g., Chen et al. 2021a).

2.3.2 Experimental Design

A brief overview of the experimental design is provided in Figure 2.2a. Beginning at 66 hours pre-TCG (06 UTC 27 August), a 60-member ensemble was created by adding perturbations to the National Centers for Environmental Prediction (NCEP) Global Forecast System (GFS) analysis using WRFDA's CV3 background error covariance matrix (Barker et al. 2004). The ensemble was then integrated forward for twelve hours using the WRF model to develop flow-dependent ensemble statistics before the first observations were assimilated at 18 UTC 27 August. At that time, the ensemble served as the background for two DA cycling experiments: GTS and GTS+IR. The GTS experiment assimilated surface and upper-level observations from the World Meteorological Organization (WMO) GTS. The GTS+IR experiment assimilated the GTS observations as well as all-sky BTs observed by channel 5 of the SEVIRI instrument onboard the Meteosat-10 satellite. Channel 5 is sensitive to upper-tropospheric water vapor. Both experiments assimilated observations hourly for twelve hours. As mentioned in section 2, this twelve-hour period represents the time during which the operationally predicted probabilities of TCG are low. More details about each type of observation assimilated will be discussed in the next sub-section.

To see the impact of assimilating all-sky IR BTs on the TCG forecasts of Irma, 5-day (120-h) deterministic forecasts were initialized from the analysis mean of each hourly DA cycle. These forecasts used the same WRF physics options described in the previous subsection. To prevent the drift of the regional WRF model during the DA cycling, analogous to the setup of the operational PSU-EnKF TC forecast system (e.g., Zhang and Weng 2015; Hartman et al. 2021), the large-scale features (horizontal wavelengths >1000 km) in the ensemble means of the first (18 UTC 27 August) and seventh (00 UTC 28 August) cycles were replaced with the large-scale features of the GFS analysis at those times. In other words, the large-scale component of the ensemble was recentered on the large-scale component of the GFS analysis. The large-scale

features were isolated using a low-pass filter via the fast Fourier transform. This recentering was done for the zonal (U) and meridional (V) wind fields, as well as perturbation potential temperature (T), water vapor mixing ratio (QVAPOR), perturbation pressure (P), and perturbation geopotential (PH) at all model levels.

2.3.3 Observations Assimilated

This subsection will provide more details about each type of observation assimilated, including choices of quality control, data thinning, and localization procedures.

The GTS observations assimilated in this study include surface observations from synoptic reports and Meteorological Aerodrome Report (METAR) data as well as upper-air observations from soundings and atmospheric motion vectors (AMVs) derived from a mixture of geostationary and polar-orbiting satellites. Figure 2.2b shows the locations of the assimilated surface and sounding observations during the first cycle. These observations, which were not thinned, are confined to the landmasses. During the remaining eleven cycles, the spatial distribution of the surface and sounding observations remained similar to the first cycle. Figure 2.2c shows the locations of the assimilated AMVs during the first cycle. A quick glance at the spatial structure of the pressure levels of these AMV observations reveals the presence of the AEW from which Irma would later evolve (lower pressure level implies higher cloud top). Note that these observations were not thinned before assimilation. All GTS observations underwent the same quality control procedure. Namely, an observation was discarded during the assimilation process if the absolute value of the observation increment (also known as the "innovation") was greater than five times the prescribed observation error, where the prescribed observation error was obtained using version 3.6.1 of the WRFDA package.

All-sky IR BTs assimilated in this study were observed by the SEVIRI instrument onboard the Meteosat-10 satellite. The SEVIRI instrument, with its twelve spectral imaging channels, provides continuous high density (3 km resolution at sub-satellite point) observations over much of the Atlantic Ocean, Europe, and Africa with a temporal frequency of one full-disk scan every 15 minutes (Schmid 2000). Eight of the twelve spectral channels are sensitive to IR wavelengths. Some notable channels include the upper-tropospheric water vapor channel

(channel 5; central wavelength of 6.2 μm), the lower-tropospheric water vapor channel (channel 6; central wavelength of 7.3μm), and the longwave window channel (channel 9; central wavelength of 10.8 μm). To be consistent with F.Zhang et al. (2019), the upper-tropospheric water vapor channel was assimilated in this study. The IR BTs assimilated during the first cycle are shown in Figure 2.2d. Once again, the AEW from which Irma evolved is clearly visible. Note that these observations were not assimilated west of 45°W. This decision was made because Meteosat-10 observations west of that longitude are quite far from the footprint of the satellite. Since that region is very far from the area of concern during the assimilation process, the decision was made to disregard them. In the area east of 45°W, the raw IR BTs have a horizontal resolution of approximately 3 km. These observations were thinned such that every eighth observation was assimilated, or one roughly every 24 km. This results in a horizontal resolution of assimilated IR BTs that was comparable to that of the AMVs.

One of the challenges associated with assimilating all-sky IR BTs is the presence of large representativeness errors that can result from a mismatch between the observed and simulated cloud scenes. To reduce the magnitude of these representativeness errors, and thereby suppress potentially unphysical analysis increments, the observation errors were adaptively adjusted via the adaptive observation error inflation (AOEI) method introduced by Minamide and Zhang (2017). AOEI inflates the observation error when the square of the difference between the observed and simulated BTs exceeds the sum of the uninflated observation error variance and simulated observation error variance. The inflated observation error is thus the observation error variance that maintains the optimal statistical relationship pointed out by Desroziers et al. (2005). This study did not reject any IR observations because it adaptively adjusted the observation error using AOEI.

To deal with under-dispersive situations where the forecast ensemble erroneously predicts clear skies despite cloudy observations, the adaptive background error inflation method (ABEI) introduced by Minamide and Zhang (2019) was employed. This method inflates the ensemble spread in such problematic regions by applying an empirically derived multiplicative inflation factor over said regions, and then propagating the inflation factor to surrounding areas through the method of Anderson (2009). ABEI is thus a spatially varying multiplicative inflation

scheme. Note that ABEI is not designed to create cloud particles during the analysis step, rather it increases the likelihood of producing clouds in the next DA cycle by increasing the ensemble spread over regions where the ensemble is spuriously clear.

Based on the innovation statistics (not shown here), and considering that only twelve DA cycles were executed, it was determined that bias correction of the IR BTs was not necessary. This is consistent with previous studies (e.g., Zhang et al. 2018, 2019b; Hartman et al. 2021; Chan and Chen 2022) that have shown that only small IR BT biases are present in the EnKF system. Future work can investigate if bias correction can further enhance the impacts of all-sky IR BT DA.

When assimilating observations in this study, ensemble covariances were localized using the Gaspari and Cohn (1999) fifth-order piecewise polynomial to eliminate the effects of spurious long-distance correlations. The localization radius of influence (ROI) used in the horizontal was 300 km for surface GTS observations (consistent with F. Zhang et al. (2019) and Hartman et al. (2021)), 100 km for upper-air GTS observations (similar to F. Zhang et al. (2019) and Hartman et al. (2021)), and 100 km for all-sky IR BTs. The choice of 100 km ROI in the horizontal for all-sky IR BTs was to make their impact comparable to that of the AMVs. Consistent with F. Zhang et al. (2019) and Hartman et al. (2021), the vertical ROI for all GTS observations was 43 vertical levels. In light of recent studies that have shown complex and non-negligible vertical correlation structures between upper-tropospheric water vapor channel BTs and state variables extending to the lower-troposphere (e.g., Chan and Chen 2022; Zhang et al. 2022), the IR BTs were not vertically-localized. It is possible that other localization ROIs may prove to be more optimal than the ones chosen - this can be explored in future work. Furthermore, adaptive localization (e.g., Lei et al. 2020; Wang et al. 2020) of all-sky IR BT observations is a very interesting topic that may be explored in future studies.

2.4 Results

This section is divided into three parts. In the first part, the tracking algorithm that was used to objectively determine the center of the TC or pre-TC disturbance at each time in the deterministic forecasts is described. The performance of the deterministic forecasts in each

experiment are compared in the second part. Finally, in the third part, a pouch-centric view of the evolution of dynamic and thermodynamic variables in the forecasts is provided to investigate the potential physical reasons that lead to the forecast improvements.

2.4.1 Tracking Algorithm

Before comparing the results of individual forecasts, it is necessary to describe the algorithm used to objectively determine the center location of the TC or pre-TC disturbance at each time. This algorithm is loosely based on the study of Majumdar and Torn (2014) in that the same quantities were used. The quantities chosen are motivated by the fact that a TC is a warm core cyclonic disturbance with a closed circulation pattern around a local minimum of sea level pressure (SLP). As such, the location of the TC's or pre-TC disturbance's center can be identified using 1) the local maxima in the 700-850 hPa layer-averaged circulation, 2) the local maxima in the 200-850 hPa thickness anomaly (i.e., difference between thickness and domain-averaged thickness), and 3) the local minima in the SLP. Circulation at any grid point was computed by horizontally averaging relative vorticity within a 100-km by 100-km square centered on said point. Note that prior to identifying the local extrema, the thickness anomaly and SLP fields were smoothed via a 2D boxcar kernel with a length scale of 100 km.

To illustrate the TC tracking algorithm, a snapshot of these three quantities (circulation, smoothed thickness anomaly, and smoothed SLP) and the simulated cloud fields (all 4 quantities are from the last hour of a forecast) are shown in Figure 2.3. Based on the three smoothed quantities in this figure, the apparent location of the TC is indicated by the white 'x' in each subplot. Since the post-TCG location of a TC is easier to identify compared to the pre-TCG location, the algorithm starts at the end of each simulation and tracks the TC or pre-TC disturbance backwards in time. This was feasible because every forecast developed a relatively strong system by the end of its simulation. Specifically, at the end of a forecast the circulation-thickness-SLP trio of local extrema was determined such that 1) all extrema within the trio were within 300 km of one another and 2) the circulation maximum in that trio was the global maximum of circulation. The location of the SLP minimum in the trio was labeled as the TC or pre-TC disturbance center at that last hour of the forecast. To find the TC or pre-TC disturbance

center at each subsequent hour working backwards in time, the locations of the maximum 700-850 hPa layer-averaged circulation, maximum 200-850 hPa thickness anomaly, and minimum SLP within 100 km of the previously found TC or pre-TC disturbance center were identified. The location of the centroid of the triangle having vertices at these locations was labeled the TC or pre-TC disturbance center at that time. The performance of this tracking algorithm was visually checked and validated with the simulated cloud fields for each hour of every forecast. Results show that the algorithm can successfully track the storm from before its TCG to the end of the 5-day forecast (not shown).

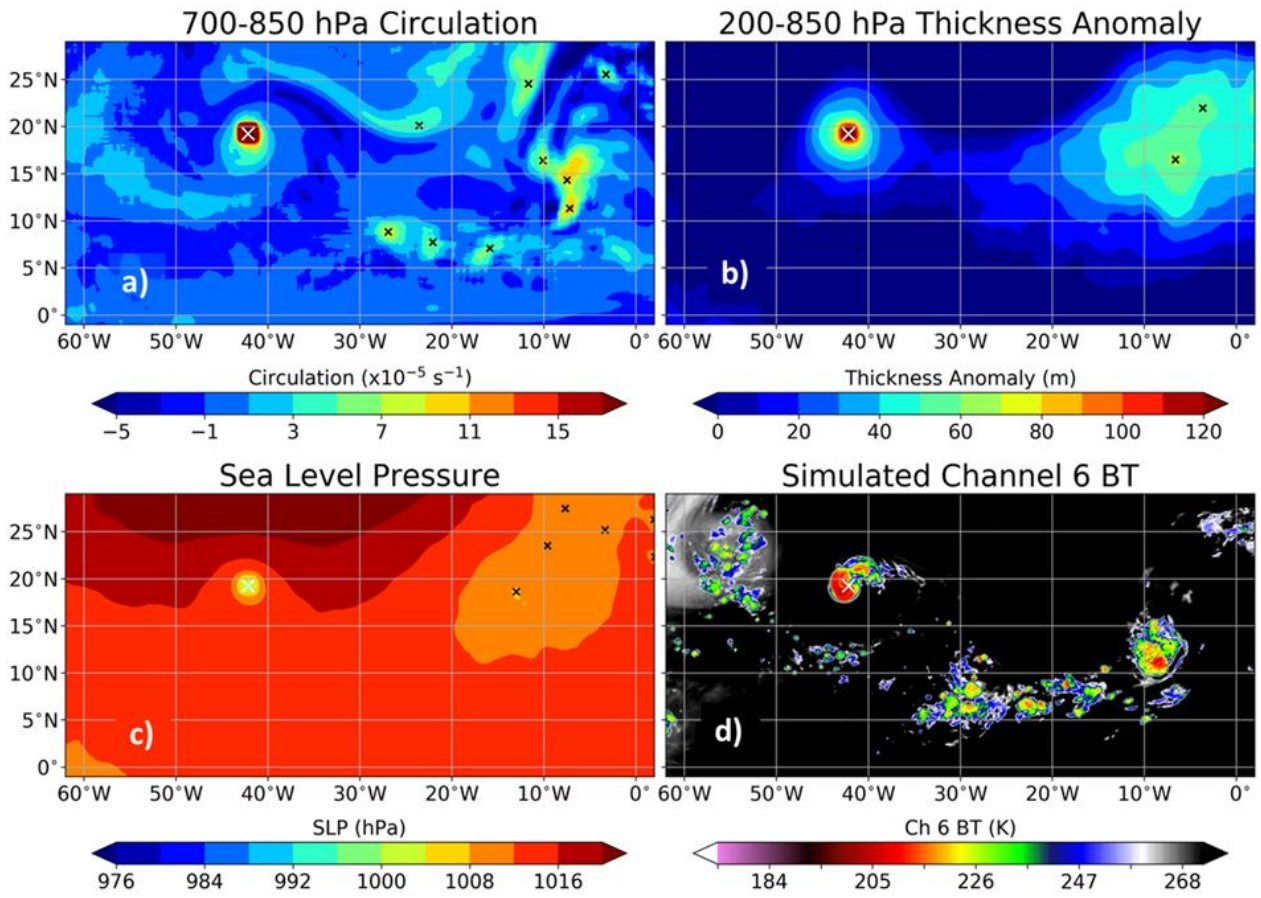

Figure 2.3. Snapshot from the last hour of the GTS deterministic forecast initialized 05 UTC 28 August of the (a) 700-850 hPa layer-averaged circulation, (b) 200-850 hPa thickness anomaly, (c) SLP, and (d) simulated SEVIRI channel 6 BT fields. Each black 'x' indicates the location of a local extremum within 150 km while the white 'x' shows the location of the TC center at this time as determined by the tracking algorithm described in the text.

2.4.2 Comparison of Deterministic Forecast Performance

In this subsection, the performance of the deterministic forecasts for each experiment are compared. The track and intensity forecasts for each experiment are provided in Figure 2.4. Note that to quantify intensity, the maximum 10-m wind speed within 300 km of the TC or pre-TC disturbance center provided by the tracking algorithm that was described in the previous subsection was found. Although a threshold wind speed for TCG was not defined in this study, it is safe to say that both the GTS (Figure 2.4b$_1$) and GTS+IR (Figure 2.4b$_2$) experiments capture the TCG of Irma since all forecasts attain at least tropical storm strength. Furthermore, both experiments predict the RI that occurred in the 48 hours after TCG. Additionally, forecasts initialized after 03 UTC August 28 in both experiments predict the plateau of Irma's intensity in the 48 to 72 hours after TCG.

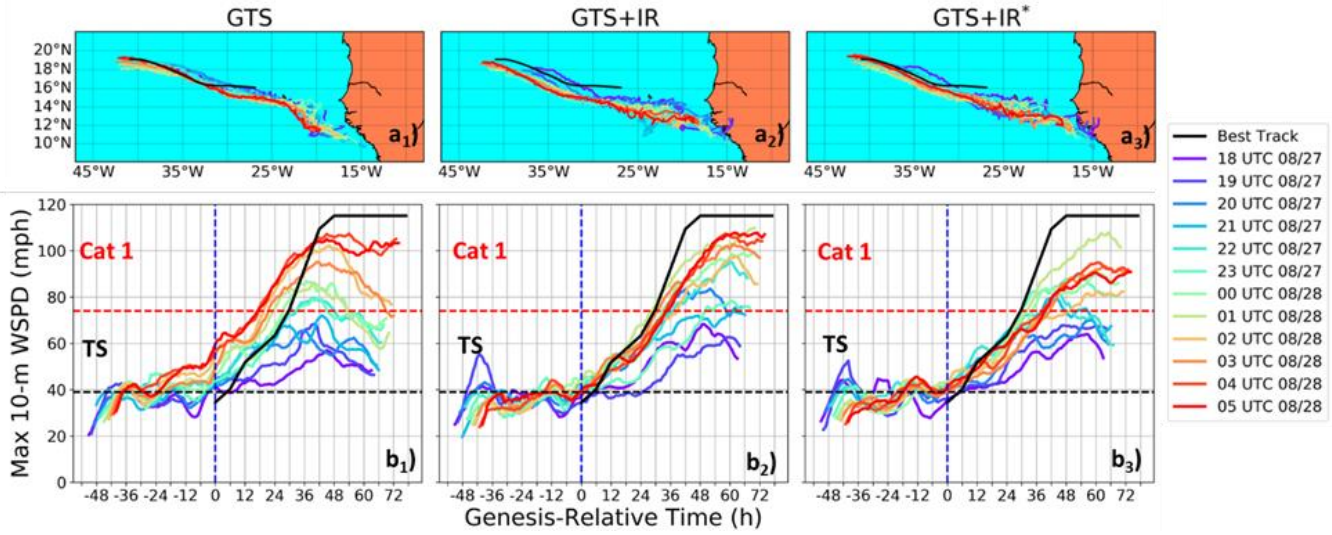

Figure 2.4. Deterministic forecasts of (a$_1$-a$_3$) track and (b$_1$-b$_3$) maximum 10-m wind speed within 300 km of the TC center for the (a$_1$,b$_1$) GTS, (a$_2$,b$_2$) GTS+IR, and (a$_3$,b$_3$) GTS+IR* experiments. In each subplot, the solid lines plotted in cool colors are the forecasts initialized from the analysis mean of the earlier cycles while the warm colors are those initialized from the analysis mean of the later cycles. Additionally, the solid black line shows the best track values from the NHC HURDAT2 database and the vertical blue dashed line denotes the time at which Irma entered the best track as a tropical depression. Refer to the text for more details on the GTS+IR* experiment.

The most salient difference between the intensity forecasts of the GTS and GTS+IR experiments is the overly premature intensification in the GTS forecasts. This difference grows as you move from the forecasts initialized from the earlier cycles (coolest colors) to the forecasts initialized from the later cycles (warmest colors) and is most prominent for forecasts initialized after 01 UTC August 28. By the last few cycles, the GTS forecasts predict a tropical storm as much as 24 hours before Irma entered the NHC's HURDAT2 best track database as a tropical depression (vertical blue dashed line). On the other hand, the assimilation of all-sky IR BTs delays the intensification such that most of the GTS+IR forecasts attain tropical storm status very close to the time of TCG in the best track. Based on this, the assimilation of all-sky IR BTs improved the timing of TCG in forecasts of Irma without degrading the forecasts of RI. This conclusion can be drawn without defining a TCG time in the forecasts since a disturbance that has reached tropical storm status and continues to intensify thereafter has clearly undergone TCG at some time prior.

Although the assimilation of all-sky IR BTs improved the timing of TCG, it degraded the track forecasts after TCG relative to the best track (Figures 2.4a_1 and 2.4a_2). A southward bias of the GTS+IR forecasts relative to the best track is evident (Figure 2.4a_2), whereas the GTS forecasts track quite close to the best track (Figure 2.4a_1). This implies that assimilating all-sky IR BTs might degrade the large-scale steering flow. One potential reason is that the ensemble error correlations between upper-tropospheric clear-sky IR BTs and the dynamical fields are weak (not shown). Hence, the limited ensemble size might lead to an unrealistic update of the large-scale circulation from assimilating upper-tropospheric clear-sky IR BTs. However, the exact reason and potential methodologies to improve the performance of all-sky IR BT DA deserves future studies, which are out of the scope of the current study.

To determine the potential impact of these track differences on the forecasted TCG timing differences, another set of twelve forecasts was initialized. The initial conditions for these new forecasts were the EnKF analysis means of the GTS+IR experiment with the environmental features replaced with those of the analysis means of the GTS experiment. To do this, a low-pass filter was used to replace the features larger than 1000 km in the zonal (U) and meridional (V) wind fields, as well as perturbation potential temperature (T), water vapor mixing ratio

(QVAPOR), perturbation pressure (P), and perturbation geopotential (PH) at all model levels. The results of these new forecasts (GTS+IR*) are shown in Figures 2.4a$_3$ and 2.4b$_3$.

Replacing the large-scale environment of the GTS+IR analyses with the large-scale environment of the GTS analyses substantially reduced the differences between the tracks of the GTS and GTS+IR experiments. Despite this, the timing of TCG in the GTS+IR* forecasts are relatively unchanged relative to the GTS+IR experiment. Furthermore, analysis (along the tracks) of SSTs, 850-200 hPa environmental shear, and average relative humidity in the layer between 950 and 700 hPa reveal no systematic differences that could explain the intensity differences between the GTS and GTS+IR forecasts (not shown). Based on these findings, it is likely that the improved TCG timing in the GTS+IR forecasts is not simply a result of differences in the large-scale environment or tracks.

2.4.3 Pouch-Centric View of Deterministic Forecasts

As discussed in the chapter introduction, TCG is a process that involves multiple scales. In this subsection, the differences between the GTS and GTS+IR forecasts on sub-synoptic scales are explored to elucidate the main reasons why assimilating all-sky IR BTs improved the timing of TCG in forecasts of Irma. To do so, the evolution of dynamic and thermodynamic quantities in a frame of reference that is moving with the AEW from which Irma formed is examined. In the analysis that follows, a separate westward phase speed of the AEW at the 850-hPa level was found for each forecast by plotting Hövmoller diagrams of meridional wind speed at those levels. The Hovmoller diagrams were constructed via averaging over the 5°N-15°N latitudinal band (similar to Figure 5 of Wang et al. 2010). On each Hövmoller diagram, the longitude-time slope of the zero-contour line separating negative (to the west) and positive (to the east) meridional velocities from forecast initialization time through 20 hours pre-TCG were found. This slope was defined as the mean phase speed of the AEW. The meridional velocities after 20 hours pre-TCG were not used in the calculation of the phase speed since many forecasts had formed a TC by this point which had likely "shed" from the AEW itself (Dunkerton et al. 2009). The AEW phase speed was then subtracted from the simulated flow fields to provide a pouch-centric view of deterministic forecasts.

As seen by the 850-hPa streamlines in Figure 2.5, a closed meso-α-scale circulation (the "pouch") becomes visible after the westward phase speed of the AEW has been subtracted from the flow. The center of this recirculation region, at the intersection of the wave trough and critical latitude (i.e., line of zero AEW-relative zonal wind), is the preferred location for TCG for both dynamic and thermodynamic reasons. Dynamically, it is the focal point for the

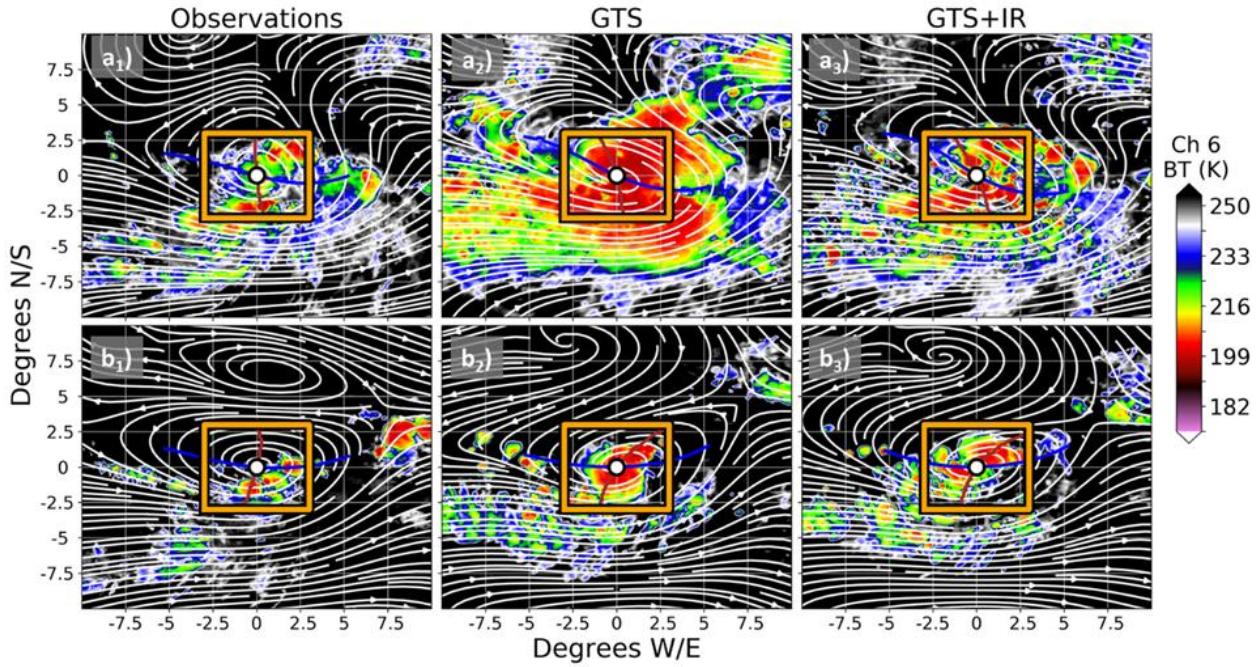

Figure 2.5. Meteosat-10 Ch 6 BT overlayed with 850-hPa AEW-relative streamlines, surface trough axis (brown line), wave critical latitude (blue line), and 850-hPa pouch center (white circle) from (a_1) observations and (a_2,a_3) EnKF analysis mean of each experiment valid 04 UTC 28 August (44 hours pre-TCG) as well as (b_1) observations and (b_2,b_3) forecasts initialized from the analyses in row 1 valid 04 UTC 29 August (20 hours pre-TCG). The streamlines, trough axis, critical latitude, and pouch center plotted in (a_1,b_1) were identified using the ERA5 reanalysis. The orange box centered on each pouch center is 6° latitude by 6° longitude.

aggregation of low-level vorticity anomalies and experiences less strain deformation (Montgomery and Enagonio 1998; Schecter and Dubin 1999; Dunkerton et al. 2009). Thermodynamically, moisture lifted above the boundary layer by deep convection accumulates near the pouch center since it is a stagnation point (Wang 2012). A positive feedback loop between the deep convection and meso-α-scale circulation was therefore postulated by Wang (2012) to lead to the formation of an enhanced meso-β-scale vortex near the pouch center that

ultimately becomes a tropical depression. More specifically, deep convection strengthens the cyclonic circulation near the pouch center through updrafts' combined influence of vortex stretching and low-level convergence, which accelerates vorticity aggregation. With a stronger circulation to retain moisture, deep convection is amplified. MCVs associated with more organized MCSs may also play a role in the TCG process (Bister and Emanuel 1997; Houze 2009). Considering this feedback loop, TCG timing is therefore determined by the details of the deep convection and its interaction with the meso-α-scale pouch circulation. In the analysis that follows, it will be shown how differences in the deep convective evolution inside the meso-α-scale pouch led to different TCG timings in the GTS and GTS+IR forecasts.

This analysis is begun by looking at simulated cloud fields within the 850-hPa pouch. Snapshots of the lower-tropospheric water vapor channel (SEVIRI Channel 6) BTs and 850-hPa wave-relative streamlines are shown in Figure 2.5 at two times as an example. Note that the ERA5 reanalysis was used to locate the "observed" pouch and pouch center in this example. At 04 UTC 28 August, the simulated channel 6 BTs of the GTS analysis mean (Figure 2.5a_2) reveal a much larger area of low BTs in the pouch compared to the observed channel 6 BTs at the same time (Figure 2.5a_1). In fact, the vast majority of the 6° latitude by 6° longitude orange box in the GTS analysis is filled with channel 6 BTs less than 210 K. The GTS+IR analysis at 04 UTC 28 August (Figure 2.5a_3) features a much-reduced area of low simulated channel 6 BTs relative to the GTS analysis as well as finer details in the simulated cloud structures. Although the simulated channel 6 BTs of the GTS+IR analysis are more realistic than the GTS analysis, they still overestimate the areal coverage of low BTs. After 24 hours of integration, the simulated channel 6 BTs of the GTS forecast (Figure 2.5b_2) are once again less realistic with a greater spatial coverage of low BTs that are more concentrated within the pouch than those of observations (Figure 2.5b_1) and the GTS+IR forecast (Figure 2.5b_3).

Not only does the GTS simulation produce more clouds than GTS+IR within the 850-hPa pouch at the times selected in Figure 2.5, but it also does so at most times leading up to TCG. In Figure 2.6, as well as all remaining figures, the forecasts initialized from the last four cycles (02 UTC through 05 UTC 28 August) are focused on since these are the forecasts that feature the most obvious pre-mature TCG in the GTS experiment (Figures 2.4b_1; 2.6a_1 – 2.6a_4). Although

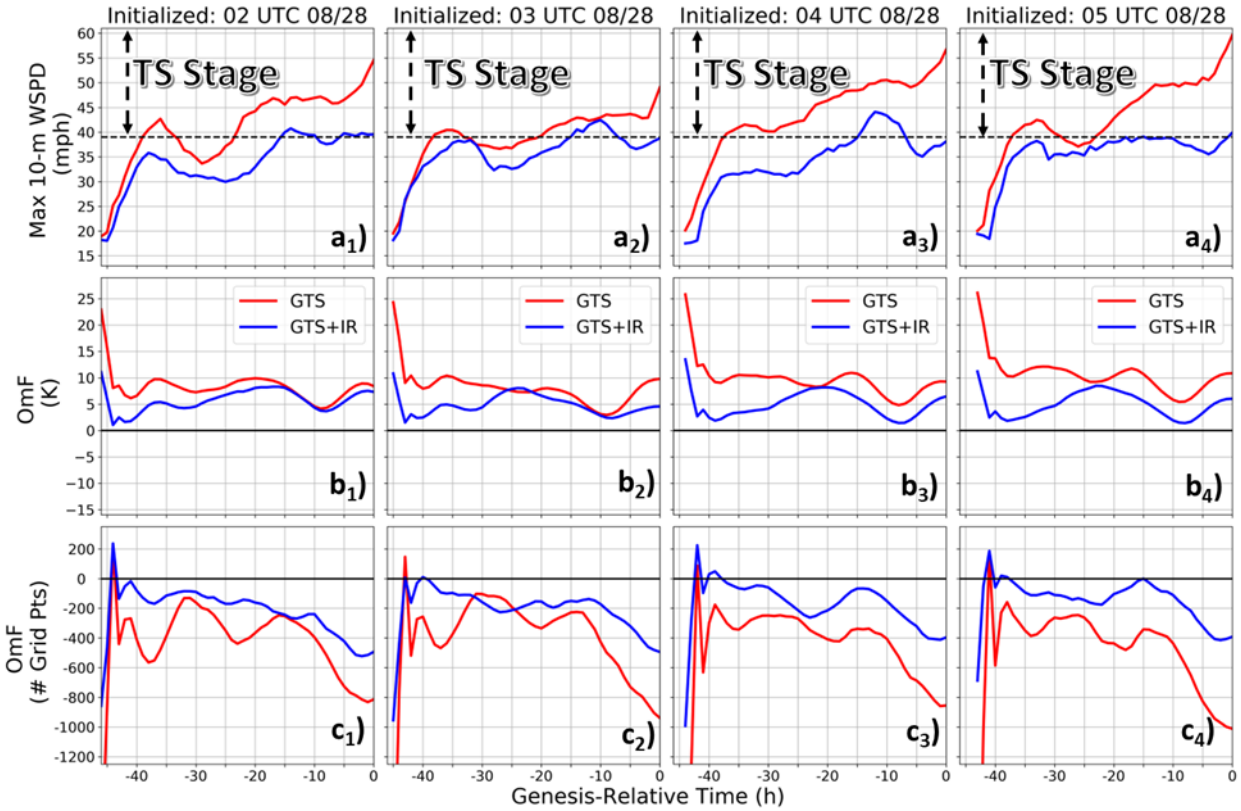

Figure 2.6. Comparison of the (a_1-a_4) maximum 10-m wind speed within 300 km of the pre-TC center, (b_1-b_4) average of Meteosat-10 Ch 6 BT OmF, and (c_1-c_4) average of cold cloud top area OmF for forecasts initialized from the 02 UTC 28 August (column 1) through 05 UTC 28 August (column 4) EnKF analysis means. Observed 850-hPa pouch center locations were approximated using the ERA5 reanalysis. Grid points in (c_1-c_4) were identified as cold cloud tops if the Meteosat-10 Ch 6 BT was less than 205 K. All averages were found over a 6° latitude by 6° longitude box centered on the 850-hPa pouch center.

the average channel 6 BT OmF ("Observation minus Forecast") value within a 6° latitude by 6° longitude box centered on the pouch center is always positive leading up to TCG (Figures 2.6b_1 – 2.6b_4) for both experiments, the average BT OmF of the GTS forecasts substantially exceeds that of the GTS+IR forecasts at most times because the all-sky IR observations helped to constrain cloud features. Furthermore, the OmF of the number of grid points having a channel 6 BT less than 205 K within those same boxes is noticeably more negative in the GTS forecasts than the GTS+IR forecasts at most times (Figures 2.6c_1 – 2.6c_4). This indicates that the GTS forecasts have more cold cloud tops than the GTS+IR forecasts. Although both experiments overproduce clouds and overpredict the spatial coverage of cold cloud tops within the pouch

relative to the observations at most times, the assimilation of all-sky IR BTs helps to alleviate these biases in the forecasts.

Since the presence of a cold cloud top does not necessarily indicate the presence of deep convection, the composite reflectivity within the 850-hPa pouch is analyzed. Here, convective area is defined as the number of grid points within the 6° latitude by 6° longitude box centered on the pouch center having a composite reflectivity exceeding 35 dBZ. A quick inspection of Figure 2.7 reveals a larger convective area at most times of the forecasts initialized from the last four EnKF analyses in the GTS experiment than the GTS+IR experiment. In summary, the GTS forecasts that undergo the most obvious pre-mature TCG feature a larger convective area and larger overproduction of cold cloud tops within the pouch than the GTS+IR forecasts. As pointed out by the previous studies, more widespread deep convection within the pouch might be more conductive to TCG (e.g., Leppert et al. 2013a,b; Zawislak and Zipser 2014).

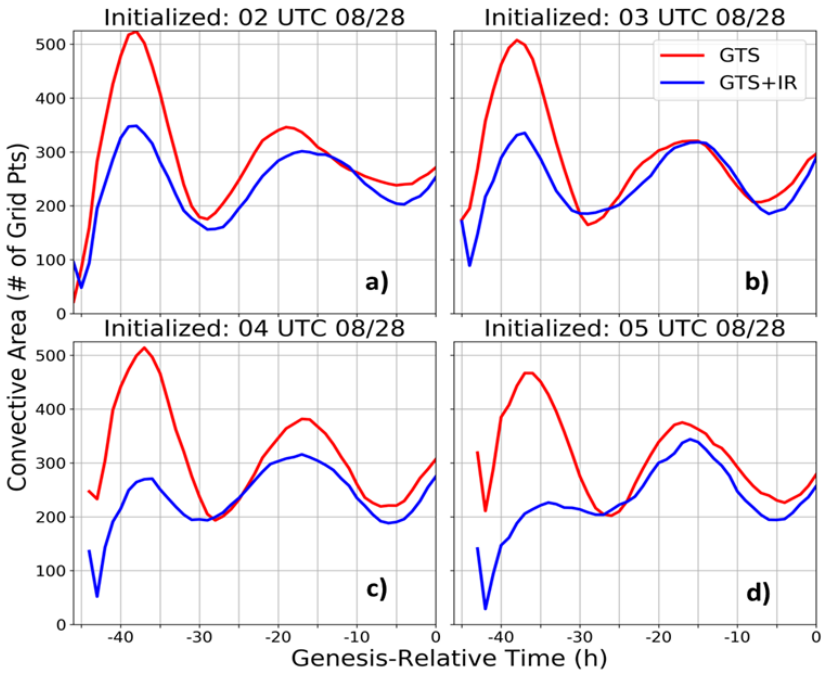

Figure 2.7. Convective area within a 6° latitude by 6° longitude box centered on 850-hPa pouch center for forecasts initialized from the (a) 02 UTC, (b) 03 UTC, (c) 04 UTC, and (d) 05 UTC 28 August EnKF analysis means, where convective core area is the total number of model grid points exceeding a composite reflectivity value of 35 dBZ.

To gain a better understanding of why the GTS forecasts produce a larger convective area within the pouch than the GTS+IR forecasts, the evolution of CSF within the pouch leading up to TCG (Figure 2.8) is revealed. CSF is calculated as the ratio of total precipitable water to saturated precipitable water. A larger CSF is favorable for sustained deep convection because it reduces the effects of entrainment of dry air into convective plumes and limits the development of evaporatively-cooled downdrafts (Neelin et al. 2009; Chen et al. 2022b). For the forecasts initialized from the last four EnKF analyses, Figure 2.8 shows the GTS ones are generally closer to saturation inside the pouch than the GTS+IR ones. The largest CSF values, which are closest to the pouch center, extend farther outward from the pouch center in the GTS forecasts than in the GTS+IR forecasts. In fact, the GTS pouch features CSF values greater than 90% at radii oftentimes beyond 100 km (Figures 2.8a_1 – 2.8a_4), whereas CSF values greater than 90% in the GTS+IR pouch are mostly confined to within 50 km of the pouch center (Figures 2.8b_1 – 2.8b_4). The larger close-to-saturated area led to more widespread deep convection within the pouch in the GTS experiment. On the other hand, all-sky IR observations provide additional information on cloud and moisture fields. As a result, the initial cloud and moisture fields are better constrained in the GTS+IR experiment.

Now that it is clear that a larger portion of the pouch in the GTS forecasts is closer to saturation than the GTS+IR forecasts, attention is turned to the meso-β-scale region near the pouch center from which the tropical depression likely forms. Figure 2.9 shows the vertical distribution of relative humidity averaged within a 2° latitude by 2° longitude box centered on the pouch in the hours leading up to TCG. The difference plots (Figures 2.9c_1 – 2.9c_4) reveal a noticeably moister inner pouch at all vertical levels in the GTS forecasts compared to the GTS+IR forecasts, especially in the forecasts initialized from the last three EnKF analyses. This is consistent with the CSF values shown in Figure 2.8.

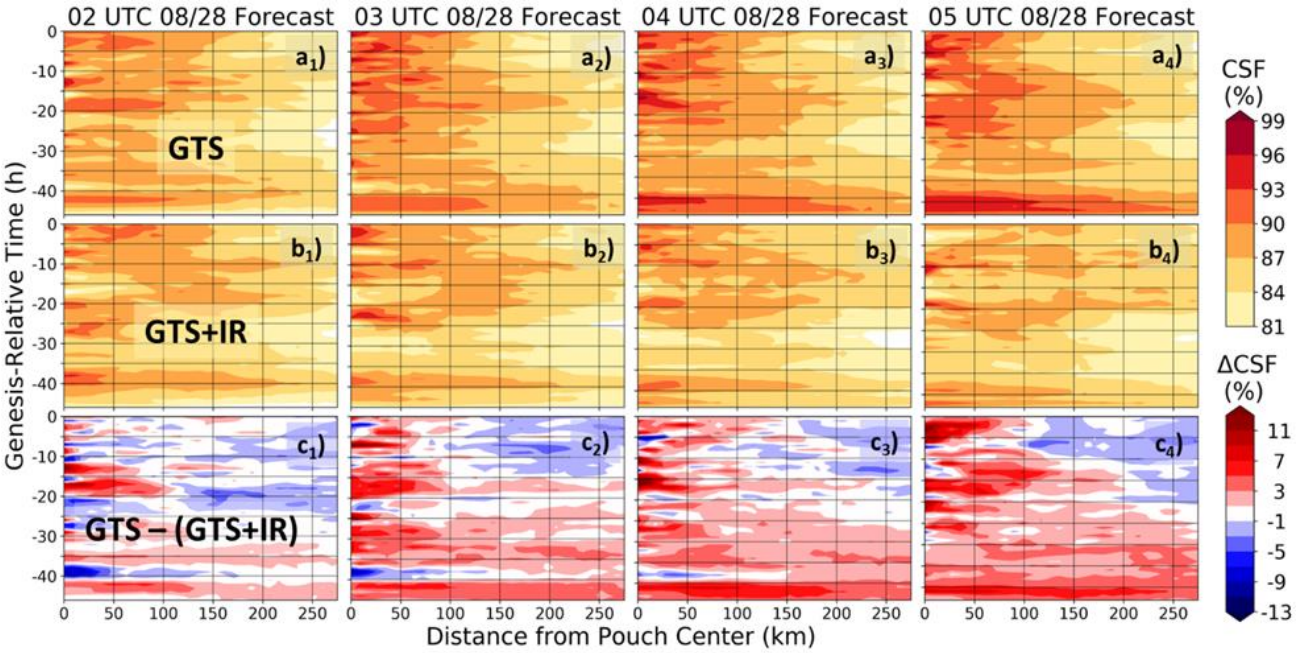

Figure 2.8. CSF as a function of distance from the 850-hPa pouch center and TCG-relative time for forecasts initialized from the 02 UTC 28 August (column 1) through 05 UTC 28 August (column 4) EnKF analysis means of the (a_1-a_4) GTS and (b_1-b_4) GTS+IR experiments as well as the (c_1-c_4) difference between the two.

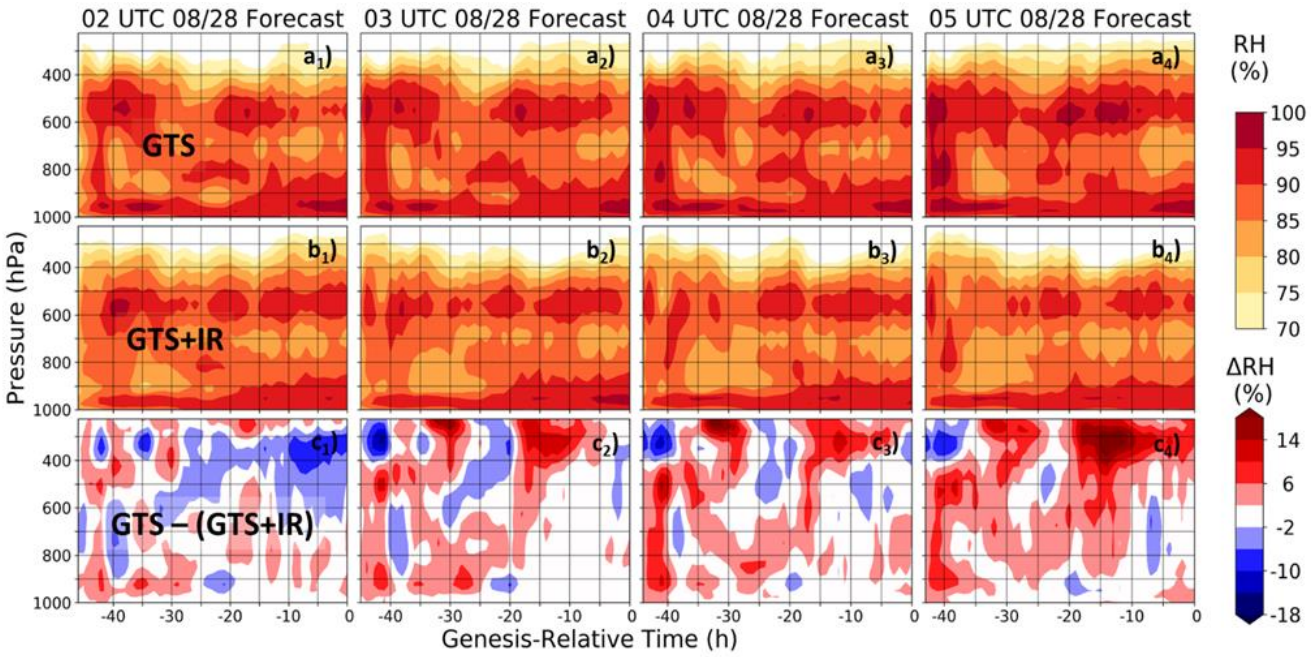

Figure 2.9. Temporal evolution of the relative humidity averaged within a 2° latitude by 2° longitude box centered on the 850-hPa pouch center for forecasts initialized from the 02 UTC 28 August (column 1) through 05 UTC 28 August (column 4) EnKF analysis means of the (a_1-a_4) GTS and (b_1-b_4) GTS+IR experiments as well as the (c_1-c_4) difference between the two.

The noticeably moister pouch in the GTS forecasts is not surprising when you consider the vertical profile of the average EnKF analysis increments to QVAPOR during the DA cycling experiments (Figure 2.10). These averages were taken over the whole domain for each cycle and then averaged over the twelve cycles. Although Figure 2.10 does not show the spatial features of the analysis increments, it reveals that the accumulated impact of the assimilation of the GTS observations in this study is to add moisture to the large-scale environment at all vertical levels. Furthermore, Figure 2.10 shows that assimilating all-sky IR BTs removes moisture from the large-scale environment at all vertical levels. Despite the large-scale drying effect of the all-sky IR BT assimilation in this study, the GTS+IR cycling experiment exhibits average QVAPOR increments that indicate an overall moistening of the large-scale environment between 700 and 925 hPa and an overall drying above 700 hPa and below 925 hPa. The precise details of why the assimilation of GTS observations resulted in moistening of the environment and the assimilation of all-sky IR BTs resulted in drying of the environment is beyond the scope of this study; however, it suffices to say that the pouch in the GTS analyses was moister than the pouch in the GTS+IR analyses (Figures 2.8 and 2.9) and that pouch was likely embedded in a moister environment (Figure 2.10). A consequence of the moister GTS pouch and environment is the development and sustenance of widespread deep convection in the forecasts.

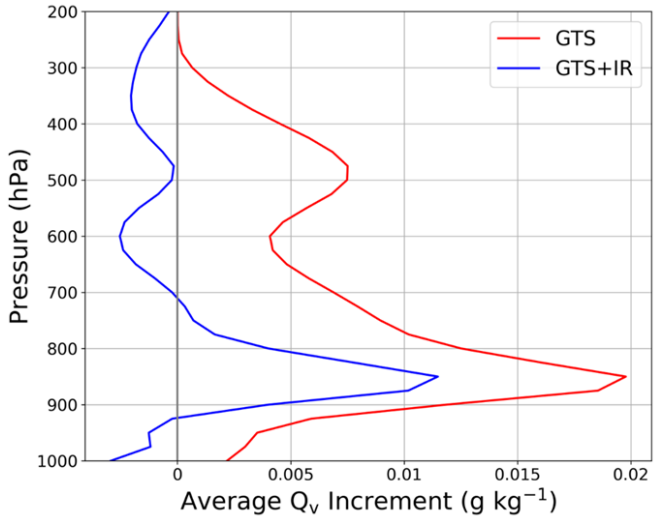

Figure 2.10. Vertical variation of the average QVAPOR increment during the EnKF analyses of each experiment.

Consistent with the moisture differences, there are also differences in dynamic fields within the meso-β-scale region near the pouch center. Figure 2.11 shows the average relative vorticity in that region surrounding the pouch center for the forecasts initialized from the last four EnKF analyses. Both the GTS (Figures 2.11a_1 – 2.11a_4) and the GTS+IR (Figures 2.11b_1 – 2.11b_4) forecasts feature the spin-up of a low-level meso-β-scale vortex well before the time at which the NHC declared TCG. Both forecasts also show the subsequent upward building of the meso-β-scale vortex in the hours after it developed. Despite these similarities, there are some striking differences. Most notably, the spin-up of the low-level vortex in the GTS forecast generally occurs approximately ten hours earlier than the GTS+IR forecast. This can be seen by referring to the time between 20- and 30-hours pre-TCG in Figures 2.11c_1, 2.11c_3, and 2.11c_4 and between 10- and 20-hours pre-TCG in Figure 2.11c_2. Not only do the GTS forecasts feature the earlier spin-up of a low-level vortex, but they also project the subsequent upward building of a stronger, deeper vortex at the meso-β-scale (Figures 2.11c_1 – 2.11c_4) relative to the GTS+IR forecasts.

In both the GTS and GTS+IR forecasts, low-level convergence precedes the spin-up of the low-level meso-β vortex (Figure 2.12). This is consistent with Wang et al. (2010), who showed that deep convective processes and their associated divergence profile can be the main player in the spin-up of a surface vortex. More specifically, low-level convergence induced by convective updrafts helps to spin-up the low-level vortex through the aggregation of positive vorticity anomalies as well as vortex stretching near the pouch center. A close inspection of Figure 2.12 reveals that the low-level convergence in the GTS forecasts is stronger than in the GTS+IR forecasts. The enhanced low-level convergence in the GTS forecasts occurs in conjunction with stronger updrafts (not shown). In short, the GTS forecasts developed a stronger layer of low-level convergence in conjunction with stronger updrafts and an earlier spin-up of the low-level meso-β-scale circulation surrounding the more saturated pouch center than the GTS+IR forecasts.

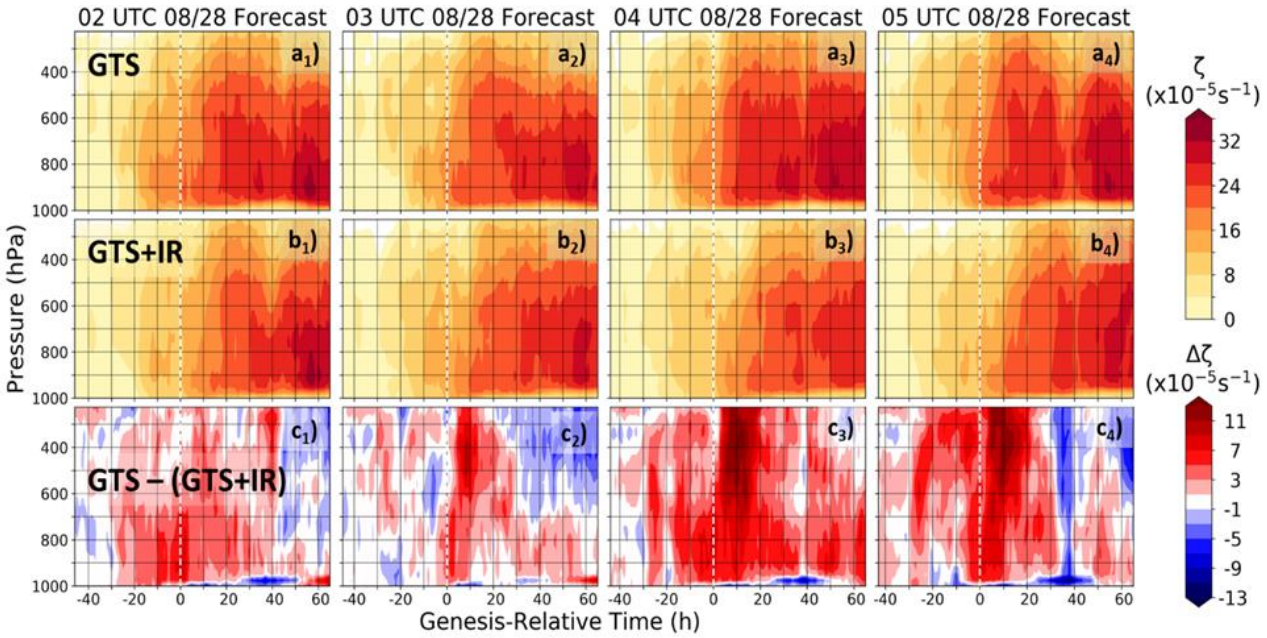

Figure 2.11. Temporal evolution of the relative vorticity averaged within a 2° latitude by 2° longitude box centered on the 850-hPa pouch center for forecasts initialized from the 02 UTC 28 August (column 1) through 05 UTC 28 August (column 4) EnKF analysis means of the (a_1-a_4) GTS and (b_1-b_4) GTS+IR experiments as well as the (c_1-c_4) difference between the two.

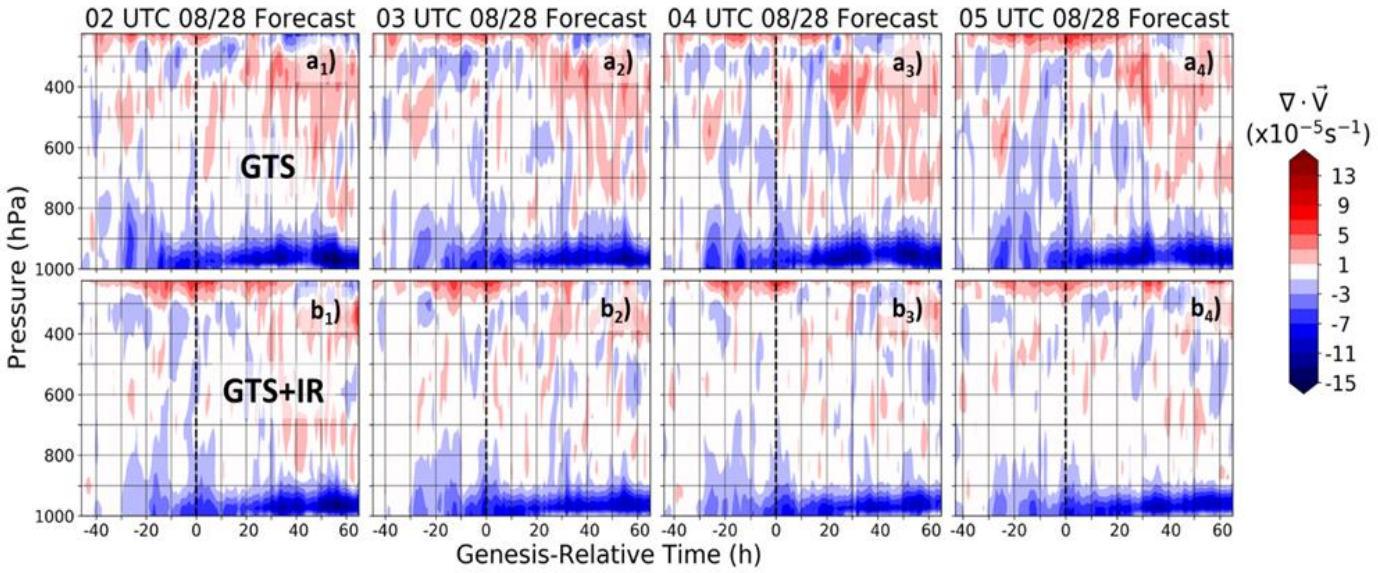

Figure 2.12. Temporal evolution of the divergence averaged within a 2° latitude by 2° longitude box centered on the 850-hPa pouch center for forecasts initialized from the 02 UTC 28 August (column 1) through 05 UTC 28 August (column 4) EnKF analysis means of the (a_1-a_4) GTS and (b_1-b_4) GTS+IR experiments.

2.5 Discussion and Conclusions

In the foregoing section, it was shown that assimilation of all-sky IR BTs improves the timing of TCG in forecasts of Hurricane Irma (2017) by up to 24 hours. This improvement is made possible by the removal of presumably excess water vapor at all model levels during the EnKF cycling. Without the assimilation of all-sky IR BTs (GTS), forecasts are initialized with a large-scale environment, as well as meso-α-scale pouch, that is moister and closer to saturation than forecasts that assimilate all-sky IR BTs (GTS+IR). Consequently, the GTS forecasts produce larger areas of deep convection within the pouch, much of which is spurious. The GTS+IR forecasts, on the other hand, produce less spurious deep convection within the pouch owing to less moisture within it and the large-scale environment. With a larger area of deep convection within the pouch, the GTS forecasts produce a stronger layer of low-level convergence relative to the GTS+IR forecasts. This enhanced low-level convergence acts to spin-up the low-level meso-β-scale vortex quicker compared to the GTS+IR forecast, ultimately leading to a TC sooner.

Recall that the NHC's Tropical Weather Outlook predicted no chance of TCG within 48 hours of the times these forecasts were initialized. On the other hand, the baseline experiment (GTS) in this study predicted TCG in all forecasts. This discrepancy is likely because the regional model used in this study has a finer grid spacing relative to those of the operational models used to produce the NHC outlook. Additionally, the baseline experiment in this study assimilated high resolution AMVs, whereas the operational models likely assimilated thinned AMVs (e.g., ECMWF (2021)).

The results of this study show that TCG timing is very sensitive to the initial moisture content within the pre-existing disturbance. The strong EnKF updates to the moisture content of the environment that ultimately led to improved TCG timing in the case of Irma are made possible by the ensemble correlations that exist between IR BTs and water vapor. Such moisture updates have been shown to dramatically improve forecasts of TC intensification, which is highly sensitive to initial moisture conditions (Emanuel and Zhang 2017). Since deep convection is sensitive to environmental moisture content, it is not surprising that assimilation of all-sky IR

BTs improved the timing of TCG in this study through its modulation of the initial moisture conditions. For this specific case, the model simulation without assimilating all-sky IR observations likely overestimated the moisture content within the pre-existing disturbance, thereby leading to pre-mature TCG. Unfortunately, high spatiotemporal in-situ observations of moisture content over the open ocean that could be used to constrain the initial moisture content well are not available. Thus, the substantial degradation in the timing of TCG in forecasts will result from either overestimation (e.g., the current case) or underestimation of the initial moisture content. All-sky IR BTs from geo-stationary satellites are arguably the only observation that can provide high resolution observations of clouds and moisture fields over most oceanic basins. Assimilating such information into models could be crucial for the future improvement of TCG forecasts.

As a pilot study, this study focused on one classic Cape Verde TC case to show the potential of all-sky IR DA to improve TCG forecasts and explored the possible physical reasoning that led to the improvement of the forecasts. Future work can and should examine more case studies to determine if the results of this study carry over to other storms. The sensitivity of TCG timing to initial moisture conditions can also be investigated in the future through a series of ensemble sensitivity experiments. Finally, the sources of the track errors that assimilation of all-sky IR BTs caused in the forecasts of Irma should be explored more.

Data Availability Statement

The EnKF analyses and WRF forecasts presented in this study can be freely downloaded from the Penn State Data Commons (https://doi.org/10.26208/sq9m-wf70). All assimilated GTS observations were obtained from datasets 351.0 and 461.0 of the National Center for Atmospheric Research's (NCAR) Research Data Archive (https://rda.ucar.edu). All assimilated Meteosat-10 SEVIRI Channel 5 BTs were ordered from the EUMETSAT Data Centre (https://www.eumetsat.int/eumetsat-data-centre).

Chapter 3

Influence of Local Water Vapor Analysis Uncertainty on Ensemble Forecasts of Tropical Cyclogenesis Using Hurricane Irma (2017) as a Testbed

ABSTRACT

Tropical cyclone formation is known to require abundant water vapor in the lower to middle troposphere within the incipient disturbance. In this study, the impacts of local water vapor analysis uncertainty on the predictability of the formation of Hurricane Irma (2017) are assessed. To this end, the magnitude of the incipient disturbance's water vapor perturbations obtained from an ensemble-based data assimilation system that constrained moisture by assimilating all-sky infrared and microwave radiances are reduced. Five-day ensemble forecasts are initialized two days before TCG using each set of modified analysis perturbations. Growth of convective differences and intensity uncertainty are evaluated for each ensemble forecast.

It is shown that when initializing an ensemble forecast with only moisture uncertainty within the incipient disturbance, the resulting intensity uncertainty at every lead time exceeds half that of an ensemble containing initial perturbations to all variables throughout the domain. Although ensembles with different initial moisture uncertainty amplitudes reveal a similar pathway to TCG, uncertainty in TCG timing varies substantially across ensembles since moister members exhibit earlier spin-up of the low-level vortex. These differences in TCG timing are traced back to the first six to twelve hours of integration, when differences in the position and intensity of mesoscale convective systems across ensemble members develop more quickly with greater initial moisture uncertainty. In addition, the rapid growth of intensity uncertainty may be greatly modulated by the diurnal cycle. Ultimately, this study underscores the importance of targeting the incipient disturbance with high spatio-temporal water vapor observations for ingestion into data assimilation systems.

3.1 Chapter Introduction

TCG, the formation of a TC, is the most challenging stage in the lifecycle of a TC to predict (Emanuel 2018). More than a decade ago, it was revealed that TCG forecasts had improved due to numerical modeling and data assimilation (DA) innovations (Halperin et al. 2013). Despite this progress, accurate TCG forecasts remain limited by highly nonlinear multi-scale interactions involving moist convective processes (Emanuel 2018; Tang et al. 2020; Núñez Ocasio 2021). This begs the question of how much TCG forecasts can be further improved in the future given their dependence on moist convection.

The rapid upscale growth of small-scale errors due to moist convective processes is a well-documented phenomenon. For example, Zhang et al. (2002) showed that release of latent heat caused mesoscale errors to grow more rapidly in simulations of a "surprise" snowstorm. Building on that study, Zhang et al. (2003) revealed that moist convective differences first manifest themselves in the form of timing and position errors of individual cells before eventually contaminating the meso- and synoptic scales. These early small-scale convective differences, Zhang et al. (2003) argue, limit the predictability of such events because they grow faster than large-scale errors. The rapid upscale growth of small-scale errors due to moist convection was also shown to influence the predictability of a baroclinic wave amplifying in a conditionally-unstable atmosphere (Tan et al. 2004; Zhang et al. 2007; Sun and Zhang 2016). In those studies, the convective differences eventually project onto the large-scale balanced flow, limiting the predictability of such phenomena. Predictability of mid-latitude severe convective and mesoscale weather is also limited by moist convective processes. These phenomena include extreme warm-season rain events (e.g., Zhang et al. 2006; Bei and Zhang 2007; Selz and Craig 2015), squall lines with bow echoes (e.g., Melhauser and Zhang 2012), and supercell thunderstorms (e.g., Snyder and Zhang 2003; Zhang et al. 2015). Finally, the rapid upscale growth of small-scale errors due to moist convection has been shown to influence the predictability of TC intensification through the rapid appearance of chaotic vortex-scale convective asymmetries (Van Sang et al. 2008; Taraphdar et al. 2014) that interact nonlinearly with the vortex flow (Zhang and Tao 2013; Tao and Zhang 2014, 2015; Judt and Chen 2016;

Fischer et al. 2023). Ultimately, rapid growth of small-scale convective differences has been shown to have a pervasive effect on the predictability of atmospheric phenomena.

Looking to the other end of the spectrum, a much more complicated picture of the predictability of atmospheric phenomena than conveyed by the previous paragraph becomes evident. Lorenz (1969) showed that small amplitude initial errors applied to the largest retained wavelength (experiment B) result in forecasts having a range of predictability comparable to that of forecasts where the same amplitude initial errors were applied at the smallest retained wavelength (experiment A). Experiment B of Lorenz (1969), combined with more recent studies (e.g., Nuss and Miller 2001; Durran et al. 2013; Surcel et al. 2015), points to the importance of large-scale initial errors on the predictability of atmospheric phenomena. Taking it a step further, Durran and Gingrich (2014) and Durran and Weyn (2016) hypothesized that small amplitude errors at larger scales (~100 – 400 km) might quickly cascade down to the smallest resolved features in a forecast. After reaching the smallest resolvable scales, those errors then quickly cascade upscale, making it look as though they originated from the smallest scales. In support of this concept, Lloveras et al. (2023) showed that midlatitude cyclone forecasts might be more sensitive to initial condition errors at the larger scales (in this case the synoptic scale) than at the smallest scales. Ultimately, numerous studies have shown that small initial condition errors at larger scales might play as much, if not more, of a role in limiting atmospheric predictability than similar errors at the smallest scales.

Regardless of how small amplitude initial errors propagate across scales, the predictability of TCG is impacted by its dependence on moisture and deep convection. It has been revealed by both observational studies (e.g., Smith and Montgomery 2012; Komaromi 2013) and modeling studies (e.g., Sippel and Zhang 2008; Zhang and Sippel 2009; Sippel and Zhang 2010; Torn 2010; Sippel et al. 2011; Doyle et al. 2012; Torn and Cook 2013; Poterjoy and Zhang 2014; Komaromi and Majumdar 2015) that TCG is sensitive to the moisture both within the incipient disturbance and in the environment through which it is moving. Although the specifics are still being debated, the complex interplay between moist convection and the circulation at low and mid-levels plays a role in TCG, as pointed out in chapter 1. From a larger-scale perspective, there is a growing body of research demonstrating that moist convection

present within the trough of an AEW can not only enhance the AEW vortex (Hall et al. 2006; Berry and Thorncroft 2012; Russell and Aiyyer 2020; Russell et al. 2020) but also make the AEW more favorable for TCG by impacting the distribution of moisture and future convection (Wang et al. 2010; Hopsch et al. 2010; Berry and Thorncroft 2012; Peng et al. 2012; Leppert et al. 2013a,b; Brammer and Thorncroft 2015; Brammer et al. 2018; Núñez Ocasio et al. 2020, 2021). Recent studies have also indicated that TCG might be more likely shortly after an AEW interacts with a Convectively Coupled Kelvin Wave in its active phase because both moisture and convective coverage are increased (Ventrice et al. 2012a,b; Schreck 2015, 2016; Lawton et al. 2022; Lawton and Majumdar 2023). Based on these studies, the impact of moisture and deep convection on the predictability of TCG cannot be understated.

In studying TCs that originate from AEWs, it is common to analyze the evolution of convection in a frame of reference moving with the wave. In this frame of reference, the preferred location of TCG is hypothesized to occur at the center of a meso-α-scale region of closed lower-tropospheric AEW-relative streamlines (Dunkerton et al. 2009). The center of this pouch is referred to as the sweet spot. Found at the intersection of the wave trough and its critical layer (i.e., where the wave-relative zonal wind is zero), the sweet spot serves as a focal point for aggregation of convection within a region of maximal relative vorticity and minimal strain/shearing deformation. In the absence of strong shear, the sweet spot is largely protected by the pouch from potentially damaging dry air intrusions. Furthermore, since the air within the pouch is continuously recirculated, the sweet spot typically has an abundance of moisture. Consequently, the area containing the sweet spot serves as an ideal location for the formation and aggregation of VHTs. The marsupial pouch paradigm described heretofore has been supported and reinforced by both modeling studies (e.g., Wang et al. 2010; Li and Pu 2014; Asaadi et al. 2016, 2017; Rajasree et al. 2016a,b) and field campaigns, including the Tropical Cyclone Structure 2008 field experiment (TCS-08; Montgomery et al. 2010a), the Pre-Depression Investigation of Cloud-systems in the Tropics (PREDICT; Montgomery et al. 2012), and NASA's Genesis and Rapid Intensification Process field experiment (GRIP; Braun et al. 2013). In short, the preferred location of TCG, in a wave-relative sense, is hypothesized to be near the intersection of the trough and critical layer of an AEW.

By using an AEW-relative framework for analysis, a recent study by Hartman et al. (2023) showed the improvements that can be brought to the timing of TCG forecasts by better capturing the convective evolution within the pouch region during the early hours of integration. That study (hereafter referred to as "HCC23") used an ensemble-based DA system to assimilate all-sky infrared (IR) radiances (hereafter brightness temperatures (BTs)) from a geostationary satellite. Through the assimilation of those BTs, the initial moisture content within the pouch and environment was modulated (in this scenario decreased; see Fig. 10 of HCC23) such that deterministic forecasts exhibited a more realistic convective evolution and TCG timing compared to an experiment that withheld them.

Motivated by the results of HCC23, this study seeks to shed light on how much improvement can be brought to the timing of TCG in forecasts by reducing errors in the initial moisture content within the pouch region. This study, which also employs an AEW-relative framework, differs from HCC23 in that it is focused entirely on the impacts of local initial water vapor uncertainty on the predictability of TCG. To demonstrate the sensitivity of TCG forecasts to initial moisture content within the pouch, sets of ensemble forecasts differing only in the amplitude of the initial moisture perturbations within it are conducted. Although convection also depends on the evolution of the wind fields, and thus initial condition errors of the wind, this study avoids artificially modifying the initial wind perturbations to avoid disrupting the gradient wind balance that may exist within the AEW vortex of the analysis. As in HCC23, Hurricane Irma (2017) is used as a test case. For a brief meteorological history of the storm, the interested reader is referred to section 2 of HCC23 as well as the National Hurricane Center's (NHC's) Tropical Cyclone Report (Cangialosi et al. 2018).

This chapter is organized as follows. Section 2 describes the DA system used to generate the initial ensemble for this study, as well as the method by which the initial moisture was modified within it. Section 3 presents the results of the moisture modification ensemble forecasts. Finally, section 4 provides a discussion of the results, including questions that remain.

3.2 Methodology

This section describes the DA system used to generate the initial ensemble of analyses for this study. After that, it details the observations assimilated by the DA system. Finally, it explains the method by which the moisture of the initial ensemble was modified.

3.2.1 DA and Forecast System

An initial 60-member ensemble of analyses for this study was created by using the Pennsylvania State University ensemble Kalman filter (PSU WRF-EnKF) DA system (Zhang et al. 2009, 2011, 2016; Weng and Zhang 2012, 2016; Chen and Zhang 2019b; Zhang et al. 2019a). To generate the ensemble, perturbations were applied to the National Center for Environmental Prediction's (NCEP) Global Forecast System (GFS) analysis using WRFDA's CV3 background error covariance matrix (Barker et al. 2004). This ensemble was then "spun up" for twelve hours using the Advanced Research version of the Weather Research and Forecasting (WRF) Model version 3.6.1 (Skamarock et al. 2008) to develop flow-dependent ensemble statistics before the first DA cycle. The DA component of this system followed the ensemble square root filter formulation of Whitaker and Hamill (2002), which updates the state via ensemble correlations that exist between simulated observations and state variables. During the assimilation of all-sky IR or microwave (MW) BTs, the Community Radiative Transfer Model (CRTM; Han et al. 2006, 2007; Weng 2007) was used as the observation operator that generated the simulated BTs. After assimilation, the ensemble of analyses was then integrated to the next DA cycle by the WRF model. In order to maintain sufficient ensemble spread during the DA cycling, relaxation to prior perturbations (Zhang et al. 2004) with a coefficient of 80% was applied. In other words, the final ensemble perturbations at each DA cycle were a mixture of 20 percent of the posterior perturbations and 80 percent of the prior perturbations.

The size and location of the domain for this study is indicated by the rectangle in Figure 3.1a. This domain size maintains sufficient distance between its boundaries and the disturbance of interest during all times of the DA cycling and subsequent forecasts. In the vertical, there were 43 levels with a top at 10-hPa. Due to the number of ensemble forecasts in this study, combined

with the size of the regional domain needed, computational constraints limited this study to a single, stationary 9-km domain.

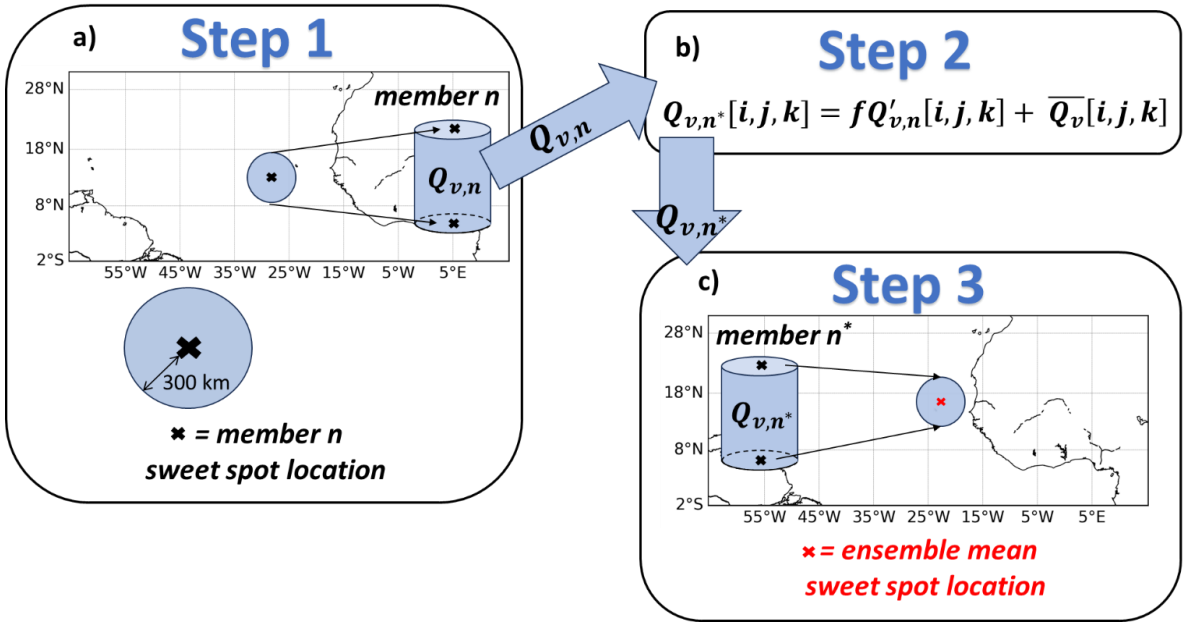

Figure 3.1. Schematic diagram showing the method by which each PRIMER (Pouch-Relative Initial Moisture Ensemble-perturbation Reduction) ensemble was generated in this study. (a) Step 1: The sweet spot locations of each of the n members in the PSU WRF-EnKF analysis were identified. The QVAPOR of each member ($Q_{v,n}$) was then extracted within a cylinder of radius 300 km surrounding its respective sweet spot. (b) Step 2: Using pouch-relative coordinates (i.e., the sweet spot for each member was the central axis of its cylinder), new QVAPOR values for each member (Q_{v,n^*}) were calculated within the cylinders by rescaling the perturbations from the ensemble mean by a factor f and then adding back the ensemble mean. (c) Step 3: The new PRIMER ensemble was generated by inserting each of the n modified cylinders into the grid of the PSU WRF-EnKF analysis mean such that their axes were co-located with the central axis of the analysis mean sweet spot location. The result was an n member ensemble having differences in only the QVAPOR within 300 km of the ensemble mean sweet spot location.

Several parameterization schemes were used during both the forecast step of the DA cycling and the ensemble forecasts. These included the following: Thompson double-moment microphysics scheme (Thompson et al. 2008), Yonsei University planetary boundary layer scheme (Hong et al. 2006), and the Rapid Radiative Transfer Model (RRTM) longwave and shortwave radiation schemes (Iacono et al. 2008). Surface fluxes of momentum, and sensible and

latent heat were parameterized via the method of Green and Zhang (2013). A cumulus parameterization scheme was not used since the grid spacing in this study has been shown to sufficiently resolve the main physical processes involved in TCG (e.g., Montgomery et al. 2010), as well as the maintenance of MCSs without the need for cumulus parameterization (e.g., He et al. 2019; Wang et al. 2015; Ying and Zhang 2018; Zhang et al. 2017; Chen et al. 2018a,b; Chen and Zhang 2019; Ying and Zhang 2017; Chan et al. 2020; Ou et al. 2020; Chen et al. 2021; Chan and Chen 2022; Chen et al. 2022a,b).

3.2.2 Observations Assimilated

Observations assimilated during hourly DA cycling fall into three categories: 1) surface and upper-level observations from the World Meteorological Organization (WMO) Global Telecommunication System (GTS), 2) all-sky IR BTs observed by the upper-tropospheric water vapor channel (channel 5) of the SEVIRI instrument on board the *Meteosat-10* satellite, and 3) all-sky MW BTs from NASA's Global Precipitation Measurement (GPM) mission network of satellites (Hou et al. 2014; Skofronick-Jackson et al. 2017). Ensemble covariances were localized using the Gaspari and Cohn (1999) fifth-order piecewise polynomial to eliminate the effects of spurious long-distance correlations. Following HCC23, the localization radius of influence (ROI) used in the horizontal was 300 km for surface GTS observations, 100 km for upper-air GTS observations, and 100 km for all-sky IR BTs. For more details about the quality control, data thinning, and localization, the interested reader is referred to section 3c of HCC 23.

This study supplemented the hourly assimilation of all-sky IR BTs with all-sky MW BTs. It assimilated one low frequency channel (19 GHz vertically-polarized) and one high frequency channel (183.31 ± 6.6 GHz; 89 GHz for sensors not having 183 GHz) to be consistent with Table B1 of Zhang et al. (2021). After thinning MW observations to a separation of 27 km (comparable to the IR BTs), an average of 400 low frequency observations were assimilated in eight of the twelve DA cycles and an average of 800 high frequency observations were assimilated in ten of the twelve DA cycles within 1000 km of the sweet spot location one would identify if they used the ERA5 zonal (U) and meridional (V) winds at 850 hPa. To be consistent with the assimilation of IR BTs, ensemble covariances when assimilating MW BTs were localized in the horizontal

with a radius of influence of 100 km for all variables. As with the assimilation of IR BTs, the adaptive observation error inflation (Minamide and Zhang 2017) method was employed to adaptively inflate the observation error when large mismatches occurred between observed and simulated cloud scenes. Consequently, none of the thinned MW BTs were rejected during the assimilation process. Finally, when calculating simulated MW BTs, non-spherical ice hydrometeor scattering properties developed by Sieron et al. (2017, 2018) were used to be consistent with the microphysics parameterization scheme.

3.2.3 Moisture Modification Ensembles

This subsection describes the method by which the initial ensemble of analyses (i.e., the analyses created by the DA system) was modified to produce new sets of ensembles (to be described shortly). Since the goal was to see the impact of initial moisture uncertainty within the pouch region on the predictability of TCG, it was natural to generate ensembles that differed only in the moisture content within the pouch region at initialization time. More specifically, the uncertainty of the initial moisture content varied systematically from ensemble to ensemble. To accomplish this, the water vapor mixing ratio (hereafter QVAPOR) perturbations of the original ensemble were shrunk while keeping the ensemble mean and spatial pattern of moisture unchanged. This process was performed in a pouch-relative sense, since each ensemble member had a different sweet spot location in the original ensemble. Hereafter, this new set of ensembles will be referred to as the PRIMER (Pouch-Relative Initial Moisture Ensemble-perturbation Reduction) ensembles.

Figure 3.1 outlines the three steps followed to generate the PRIMER ensembles. The first step in this figure shows the extraction of the QVAPOR values within a cylinder of radius 300 km centered on the initial sweet spot location of each member. These extracted cylinders were then aligned such that their central axes were collocated and each grid point within these cylinders was aligned based on its position relative to the central axis (in other words, sweet spot-relative coordinates are used such that the sweet spot is the origin/central axis). In the second step, the perturbations from the mean were shrunk at each grid point within the cylinders by rescaling them by a fraction f and then adding them back to the ensemble mean value at that

grid point. For the third step, the sweet spot location of the PSU WRF-EnKF analysis mean was identified and the QVAPOR values within 300 km of it were replaced with the values obtained in step two. This resulted in new ensembles, with the only difference across members being the QVAPOR within 300 km of the ensemble mean sweet spot location. It is important to note that all variables other than QVAPOR were set to the ensemble mean values at every location within the domain. Also, the QVAPOR values outside of the cylinders were also set to the ensemble mean values. Finally, the boundary conditions for all forecasts came from the NCEP GFS analysis of 00 UTC 28 August. This design enabled the impacts of initial moisture uncertainty within the pouch region to be isolated, disentangling it from other sources of uncertainty such as the environmental moisture and other variables.

A total of twelve moisture modification ensembles were produced – eleven PRIMER ensembles plus Stochastic Q_v'. In Stochastic Q_v', random perturbations drawn from a normal distribution ($\mu = 0$, $\sigma = 0.01$ g kg^{-1}) were added to the ensemble mean QVAPOR values at only the lowest model level within 300 km of the ensemble mean sweet spot location. This ensemble was created to show the intrinsic limit of predictability for this case. The eleven PRIMER ensembles (PRIMER-0.01, PRIMER-0.1, PRIMER-0.2 … PRIMER-1.0) differed only in the fraction *f* by which the QVAPOR perturbations were rescaled. Figure 3.2 shows the initial hour ensemble spread (i.e., standard deviation) of the lowest model level QVAPOR for two of the ensembles. Note the spread of Stochastic Q_v' (Figure 3.2a) is two orders of magnitude lower than PRIMER-1.0, which has the highest perturbation amplitude (Figure 3.2b). By design, the spatial pattern of QVAPOR spread for PRIMER-1.0 is identical to the other ten PRIMER ensembles (not shown). Consequently, the spread of PRIMER-0.01 is similar in magnitude to Stochastic Q_v' but has a spatial pattern identical to the other PRIMER ensembles. The spatial pattern of QVAPOR spread in the PRIMER ensembles (Figure 3.2b) reveals the pattern of inner-pouch moisture uncertainty that exists in this state-of-the-art DA system. Moisture uncertainty is greatest in the northeast quadrant of the pouch and generally decreases towards the southwest. This pattern of moisture uncertainty results from uncertainty in the positioning of a moisture gradient that exists to the northeast of each member's pouch combined with uncertainty in the positioning of those pouches (not shown).

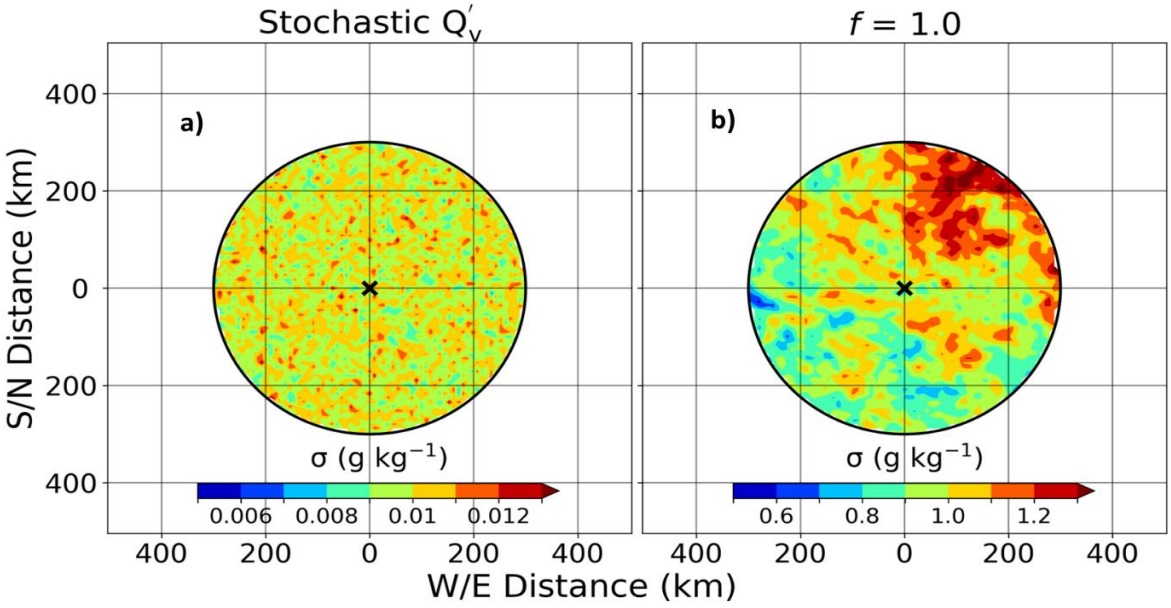

Figure 3.2. Initial-hour ensemble spread of the QVAPOR (g kg^{-1}) at the lowest model level for the (a) stochastic Q_v', and (b) PRIMER-1.0 ensemble forecasts. In each subplot, the black 'x' denotes the sweet spot location. Note that the color bars are different for each subplot.

3.3 Results

This section is divided into three subsections. The first subsection presents the results of the five-day ensemble forecasts and quantifies the impact of initial moisture uncertainty on the evolution of intensity uncertainty. The second subsection shows the impact of initial moisture uncertainty on the growth of convective differences during the early hours of the forecasts. Finally, the last subsection reveals the impact of initial moisture uncertainty on pathways to TCG and the timing of TCG.

3.3.1 Impact of Initial Moisture Uncertainty on Intensity Uncertainty

The initial ensemble containing the full EnKF perturbations used in this study came from the 02 UTC 28 August analysis (the ninth DA cycle) of the PSU WRF-EnKF. This analysis was chosen because the ensemble mean of the ensemble forecast initialized from it follows the NHC's HURDAT2 best track data more closely than any other ensemble initialized around 48 hours before the observed TCG time. Note that this study defines the observed TCG time as the

time at which Irma entered the best track database as a tropical depression (i.e., 00 UTC 30 August).

Before exploring the growth of intensity uncertainty in the PRIMER ensembles, it is important to keep in mind the intensity uncertainty that exists in the full EnKF ensemble, which serves as the benchmark for this study. Figure 3.3 shows the temporal evolution of the intensity and track of each member in the full EnKF ensemble, which was initialized 46 hours before the observed TCG time. Throughout this manuscript, the term "storm center" refers to the sweet spot location prior to TCG time and the TC center location after TCG time. The TC center location was determined using the tracking algorithm of HCC23, which is loosely based on the study of Majumdar and Torn (2014) in that the same quantities were used. This algorithm defines the TC center as the centroid of the triangle having vertices at the locations of the maximum 700-850-hPa layer-averaged circulation, maximum 200-850-hPa thickness anomaly, and minimum sea-level pressure (SLP). A quick look at Figure 3.3a reveals the wide range of intensity forecasts in the full EnKF ensemble. By the observed TCG time, the range of minimum SLP values reaches 10-hPa to 20-hPa and grows to ~ 60-hPa by the end of the forecasts. Although the ensemble mean captures the TCG and subsequent intensification (from 0 h to 40 h) of Irma quite well compared to the best track, many members do not – some drastically overestimate the intensity while others fail to develop it at all. Furthermore, there is a general tendency to produce a stronger storm when the initial moisture content within the pouch is higher. This tendency is more noticeable during the pre-TCG period. The full EnKF also exhibits sizeable track uncertainty (Figure 3.3b). This uncertainty is a result of several factors. These factors include uncertainty in the initial sweet spot location, uncertainty in the initial values of all variables, the β effect (i.e., a northwestward drift of the vortex *in the northern hemisphere* due to differential advection of the Earth's vorticity that increases with increasing vortex strength), and nonlinear interactions among variables during integration. In summary, the benchmark ensemble forecasts used in this study, although representative of a state-of-the-art DA system, have considerable room for improvement in both intensity and track.

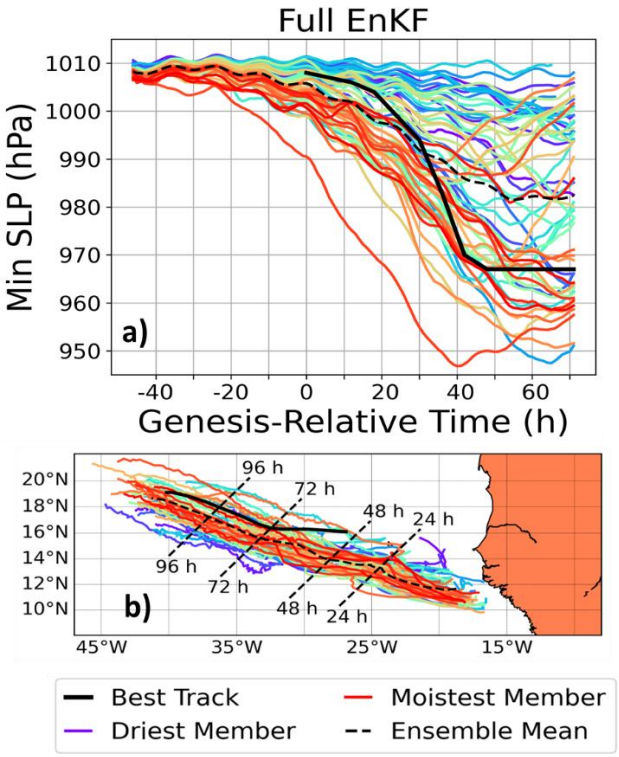

Figure 3.3. Forecasts of the (a) minimum sea-level pressure (hPa) within 300 km of the storm center and (b) track of the disturbance for the ensemble initialized with the full PSU-WRF EnKF perturbations to all variables. Line colors represent the amount of moisture within 300 km of the pouch center at initialization time, with the coolest colors having the lowest and the warmest colors having the highest volume-averaged QVAPOR. The position of the ensemble mean forecasted storm center at select lead times is indicated in (b) by orthogonal black dashed lines.

Now that the full range of intensities in the full EnKF ensemble has been revealed, attention is given to the intensity uncertainty that develops because of the initial moisture uncertainty within the pouch. Figure 3.4 shows the intensity and track forecasts for some of the moisture modification ensembles. In terms of minimum SLP, the Stochastic Q_v' (Figure 3.4a) and PRIMER-0.01 (Figure 3.4b) ensemble forecasts are visually quite similar. Differences that arise between the intensities of these two ensembles, albeit quite small, might be a result of the spatial pattern of initial QVAPOR uncertainty. How the spatial pattern of initial QVAPOR uncertainty impacts the intensity uncertainty is an interesting question but is beyond the scope of this study. As initial QVAPOR uncertainty increases to one-tenth (PRIMER-0.1, Figure 3.4c) of, and eventually all (PRIMER-1.0, Figure 3.4d) of the full EnKF QVAPOR uncertainty, the range

of forecasted intensities increases. Also noticeable is an increase in the range of track forecasts with initial QVAPOR uncertainty (Figures 3.4e, 3.4f). This is most likely tied to the β effect since the stronger members track farther to the north. This can be seen most easily in the PRIMER-1.0 (Figure 3.4f) ensemble. To summarize, since QVAPOR within the pouch was the only variable that differed in the initial conditions of the PRIMER ensembles, uncertainty of initial moisture within the pouch region translates to noticeable uncertainty in the forecasted intensity.

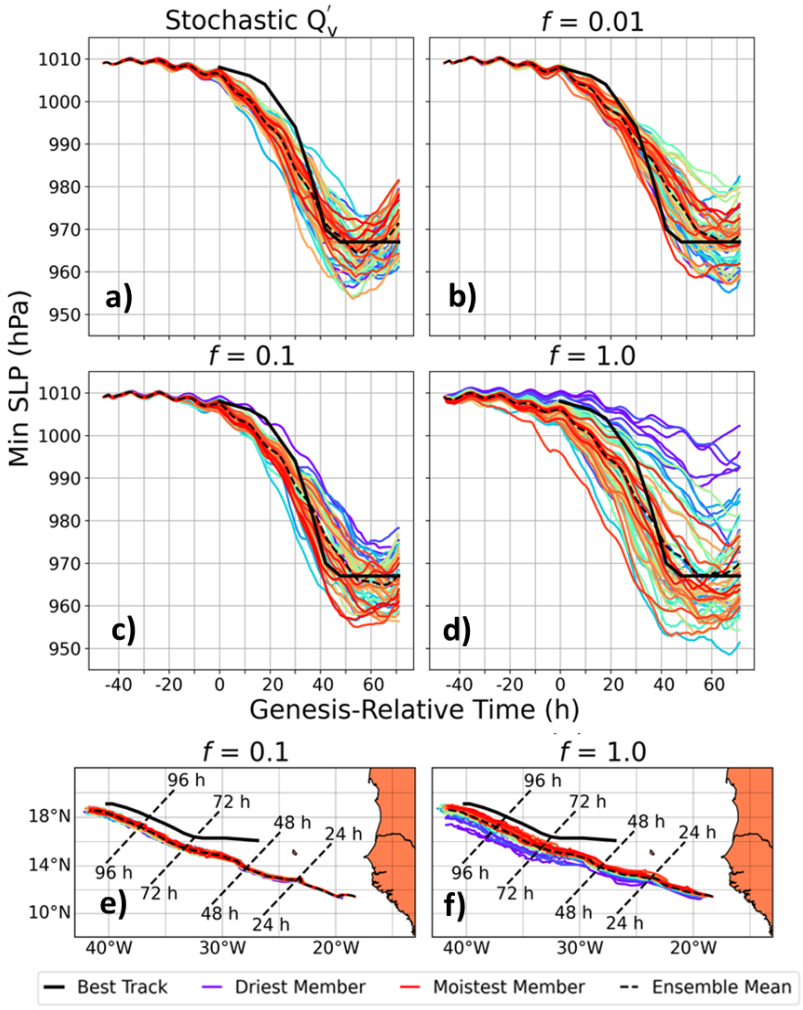

Figure. 3.4. As in Figure 3.3, but for forecasts initialized with (a) stochastic perturbations to the lowest model level QVAPOR, as well as the (b) PRIMER-0.01, (c,e) PRIMER-0.1, and (d,f) PRIMER-1.0 perturbations. Track forecasts for the stochastic and PRIMER-0.01 ensembles exhibit insufficient spread to warrant inclusion.

The increase of intensity uncertainty with initial moisture uncertainty is associated with the propensity for the initially moister members to intensify earlier and reach a greater peak intensity. This is most noticeable for the PRIMER-1.0 (Figure 3.4d) ensemble, where a clear stratification by initial QVAPOR is evident. This is quantified a bit further by showing the Pearson correlation coefficient between the initial QVAPOR and the intensity for each ensemble (Figure 3.5a) forecast. Strong negative correlations exist between initial QVAPOR and minimum SLP in the PRIMER-1.0 ensemble. These correlations are statistically significant at greater than 95% confidence based on the Student's two-tailed t-test (Gosset 1908) for almost all hours of the forecast (Figure 3.5b). This supports the claim that initially moister members intensify earlier and more. As the initial QVAPOR uncertainty decreases, the correlation between initial QVAPOR within the pouch and minimum SLP becomes less negative (Figure 3.5a) and less statistically significant (Figure 3.5b). This trend is likely a result of the decreasing divergence between moist and dry members with decreasing initial moisture uncertainty. The correlation values are most negative in the full EnKF ensemble forecast. This is because the members in the original analysis that have the lowest SLP tend to also have the most moisture in the pouch (not shown) because the PSU WRF-EnKF updates QVAPOR via the ensemble correlations that exist between it and other variables. Ultimately, ensemble members with more moisture within the initial pouch region will intensify earlier and reach a greater peak intensity, thus causing the intensity uncertainty to be greater when the initial moisture uncertainty is greater.

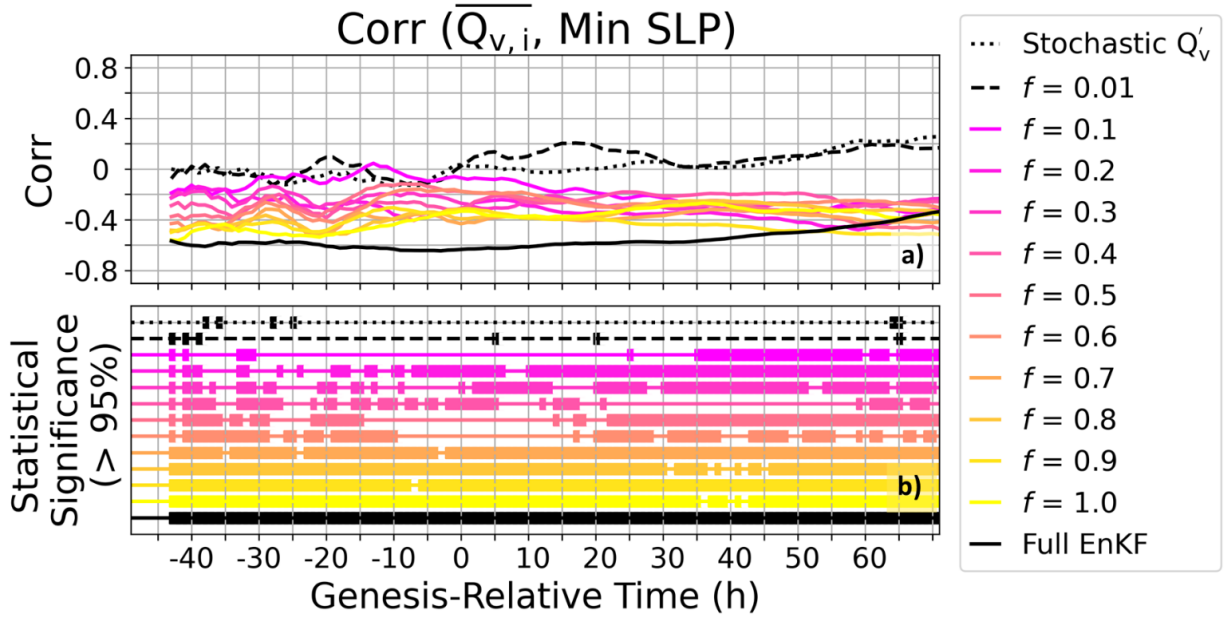

Figure 3.5. (a) Pearson correlation coefficient between the initial-hour volume-averaged QVAPOR within 300 km of the pouch center and the minimum sea-level pressure within 300 km of the storm center for each ensemble forecast. The times for which each correlation value in (a) is statistically significant at greater than 95% confidence based on the Student's two-tailed t-test (Gosset 1908) are indicated in (b).

This subsection is concluded by showing the growth of intensity uncertainty (Figure 3.6) in terms of ensemble spread of minimum SLP. The ensemble spread of minimum SLP grows for all moisture modification ensembles (Figure 3.6a) up to about the point when intensification paused in the best track data (~ 40 hours after the observed TCG time). After that point, the ensemble spread decreased, indicating the members generally agreed intensification would pause. Also evident in Figure 3.6a is the trend towards greater intensity uncertainty as the initial QVAPOR uncertainty within the pouch increased, consistent with Figure 3.4. Note the spread of minimum SLP for the full EnKF ensemble begins at a nonzero value, maintains an almost constant vertical separation with the PRIMER-1.0 ensemble until about 40 hours after the observed TCG time, and then continues to increase almost until the end of the forecast (Figure 3.6a). This trend implies that initial uncertainty in the non-QVAPOR values of the full EnKF ensemble might have played only a minor role in the intensity uncertainty until well after the observed TCG time. By comparing the PRIMER-1.0 ensemble spread of minimum SLP to that of the full EnKF ensemble in Figure 3.6a, it can be concluded that initial moisture uncertainty

within the incipient disturbance plays a crucial role in determining the intensity uncertainty during the hours leading up to the observed TCG time.

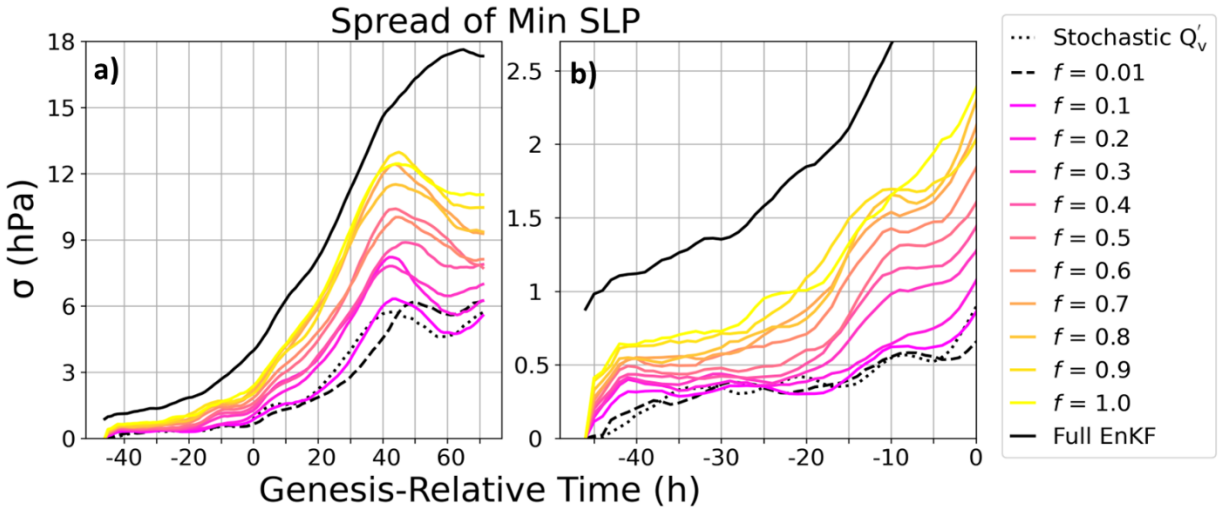

Figure 3.6. Ensemble spread of the minimum sea-level pressure (hPa) within 300 km of the storm center for each ensemble forecast. (b) shows the first 46 hours of (a). Note the y-axis is different in each subplot.

Intensity uncertainty evolution before the observed TCG time is shown more closely in Figure 3.6b. This figure reveals three phases in the evolution of intensity uncertainty during the hours leading up to the observed TCG time. The first phase sees a rapid growth of uncertainty during the first six hours. After the period of rapid uncertainty growth, a roughly twelve-hour period of quasi-steady values followed. Beginning at about 30 hours before the observed TCG time, the ensemble spread increases once again and continues through TCG time. At the start of the last phase, the ensembles with greater initial QVAPOR uncertainty already had larger intensity uncertainty, enabling them to achieve even larger uncertainties by the observed TCG time. This three-phase pattern will be discussed in the next two subsections.

3.3.2 Impact of Initial Moisture Uncertainty on Growth of Convective Differences

This subsection investigates more closely the divergence of forecasts within each ensemble prior to TCG. To focus on the meso-β-scale, the volume-averaged difference kinetic energy (DKE) was calculated within a 2° x 2° box centered on the storm center. DKE between any two ensemble members is given by,

$$\boldsymbol{DKE_{i,j,k}} = \frac{\mathbf{1}}{\mathbf{2}}\boldsymbol{u'^{2}_{i,j,k}} + \frac{\mathbf{1}}{\mathbf{2}}\boldsymbol{v'^{2}_{i,j,k}}, \quad (1)$$

where $\boldsymbol{u'_{i,j,k}}$ and $\boldsymbol{v'_{i,j,k}}$ are the differences between the *u* and *v* wind components at each location in storm-relative coordinates. The DKE at each location was then averaged over the 1,770 combinations $\binom{\mathbf{60}}{\mathbf{2}}$ of ensemble member pairs before taking a volume average. Figure 3.7 shows the trend of DKE during the hours leading up to the observed TCG time. It resembles the ensemble spread in minimum SLP (Figure 3.6b); however, it is smoother and increases monotonically with initial moisture uncertainty. The rapid divergence of the ensemble forecasts during the first few hours appears quite prominent in the DKE plots. Close inspection reveals a local maximum of DKE occurs between eight and ten hours after initialization (38 to 36 hours before the observed TCG), which is about four to six hours after the minimum SLP spread flattens out (see Figure 3.6b). This subtle discrepancy might be a consequence of changes in wind speed lagging that of changes in minimum SLP. Another interesting trend in Figure 3.7 is the decrease in DKE from about 38 to almost 30 hours before the observed TCG time, which are times when the spread of minimum SLP remained quasi-steady. The dip in DKE during these times might reflect changes in the structure of the vortex as well as the potential impact of a diurnal cycle (discussed later). Since DKE (a bulk quantity) and ensemble spread of minimum SLP (a point metric) are two very different ways of quantifying the divergence of the intensity forecasts, it should not be surprising that they exhibit some differences. In summary, multiple metrics reveal a rapid divergence of the intensity forecasts during the first six hours, followed by a roughly twelve-hour pause in divergence, before rapidly diverging through the observed TCG time.

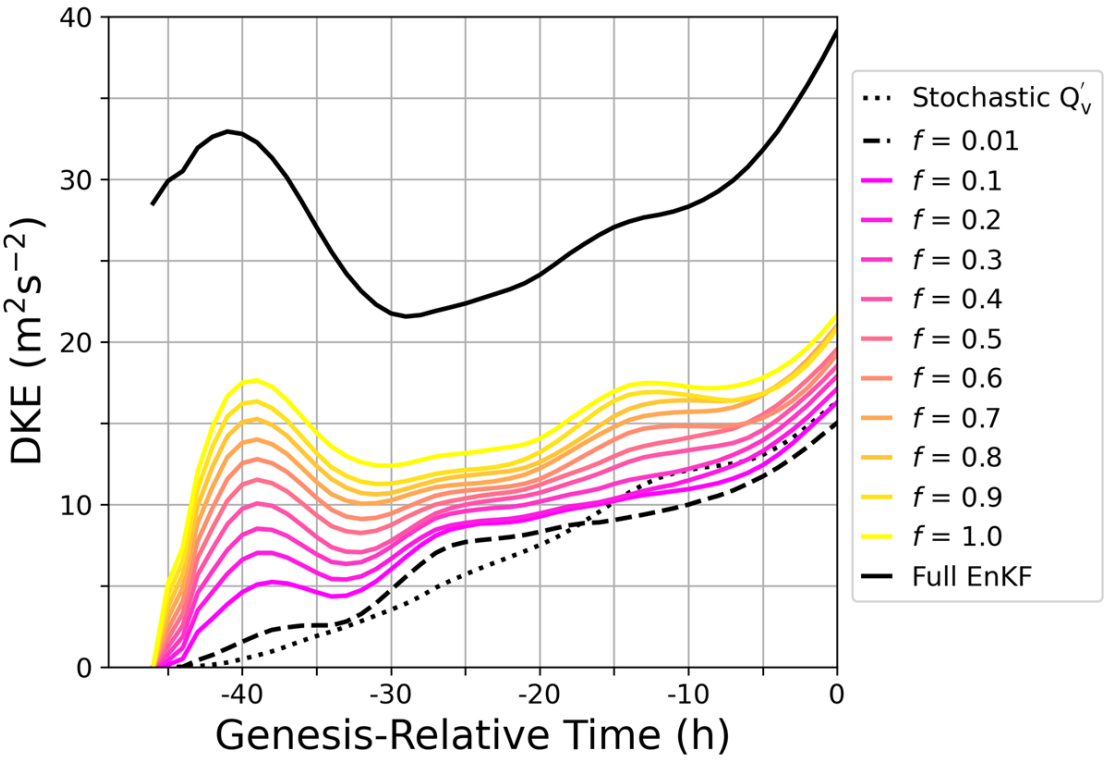

Figure 3.7. Volume-averaged difference kinetic energy (m^2 s^{-2}) computed within a 2° x 2° box centered on the storm center for each ensemble forecast.

Upscale growth of errors to the pouch-scale can be seen in convective differences. Figure 3.8 shows spaghetti plots of the 210 K simulated *Meteosat-10* channel 6 BT contour in the region where initial QVAPOR perturbations were modified. Channel 6, with a central wavelength of 7.3μm (Schmid 2000), is sensitive to lower-tropospheric water vapor. Note that this channel was not assimilated in this study. The 210 K contour represents cold cloud tops, indicative of deep convection. After one hour of integration, all 60 members in both PRIMER-0.01 (Figure 3.8a_1) and PRIMER-0.1 (Figure 3.8b_1) ensembles agree on the positioning of this contour (i.e., deep convection). At this time, a large MCS can be seen in the western half of the pouch region. When initial QVAPOR uncertainty is increased to half of the full EnKF, slight discrepancies in the positioning of this contour become noticeable within one hour (Figure 3.8c_1). These discrepancies, which show the small coverage differences of that MCS among members, are due to small differences in its intensity across members. These intensity differences become more

noticeable when the initial QVAPOR uncertainty is increased to the full EnKF's (Figure 3.8d_1). Some members in PRIMER-1.0 develop new convection in the southern and eastern parts of the pouch region after one hour. As it is integrated further, these members develop the new convection while others subsequently develop their own new convection in other positions (Figure 3.8d_2). By hours three (Figure 3.8d_3) and four (Figure 3.8d_4), through a combination of MCS dislocation and intensity errors, convective differences in the PRIMER-1.0 ensemble have spread throughout the entire region of the initial pouch. This process ensues for all ensemble forecasts; however, its onset appears later as initial QVAPOR uncertainty decreases. For example, the PRIMER-0.5 ensemble shows signs of dislocation errors cropping up after two hours of integration (Figure 3.8c_2), PRIMER-0.1 after three to four hours (Figures 3.8b_3 – 3.8b_4), and PRIMER-0.01 after about six hours (not shown). There appears to be no visible relationship between the initial QVAPOR of a particular member and either where new convection develops or how large the MCSs are. This shows how truly nonlinear and stochastic the system is. The take-home message of Figure 3.8 is that greater initial moisture uncertainty within the pouch region leads to earlier development of dislocation errors in future MCSs, and these dislocation errors rapidly grow to overwhelm the area of the pouch.

Before discussing the impacts of initial moisture uncertainty on pathways to TCG and its timing, the key finding of this subsection is summarized: increasing the uncertainty in the initial moisture content within 300 km of the pouch center leads to larger uncertainty in the intensity forecast during the first six to twelve hours due to an earlier development and faster growth of MCS dislocation and intensity differences.

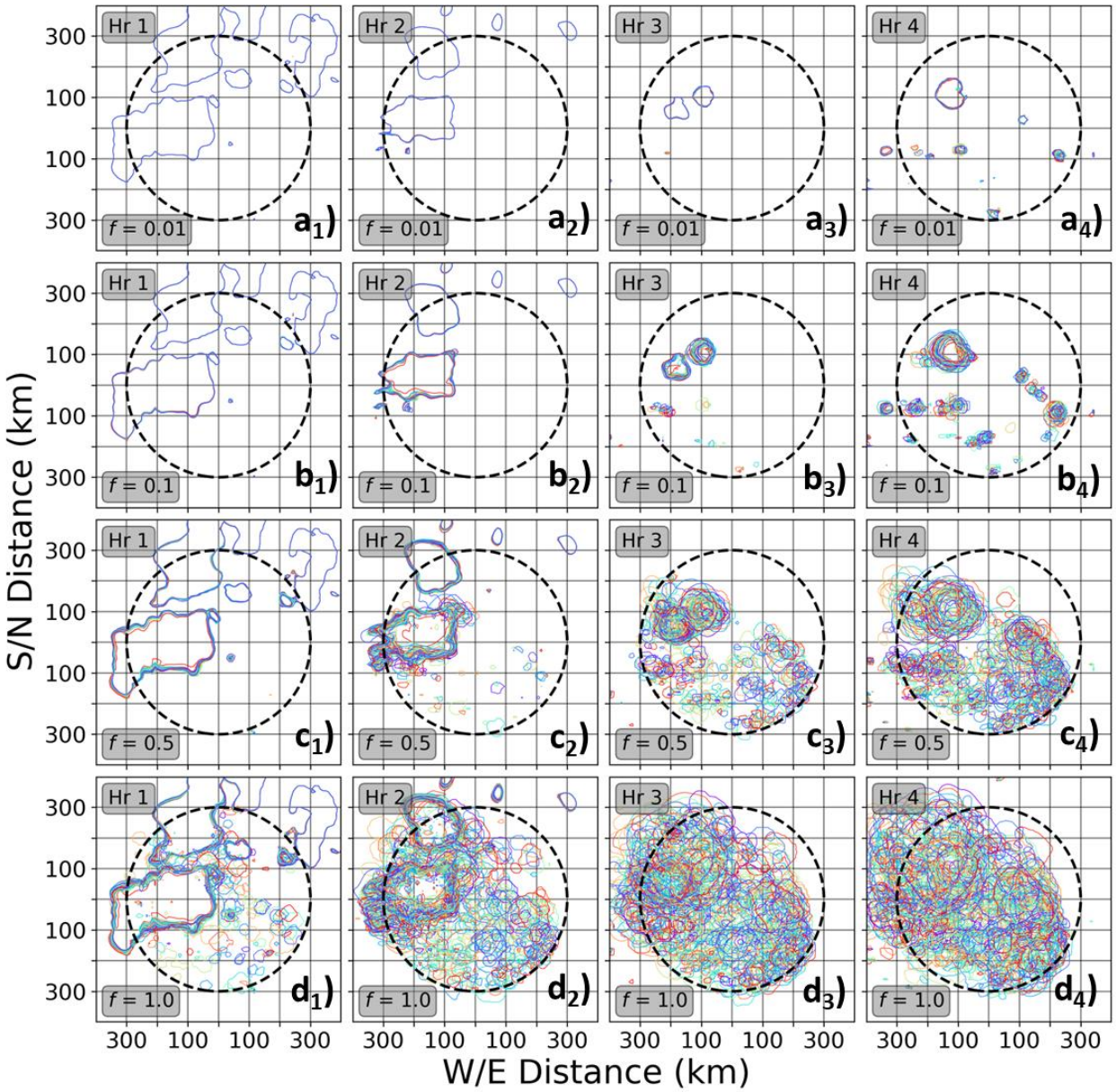

Figure 3.8. Spaghetti plots of the 210 K *Meteosat-10* simulated channel 6 BT contour for the ensemble initialized with (a_1-a_4) PRIMER-0.01, (b_1–b_4) PRIMER-0.1, (c_1-c_4) PRIMER-0.5, and (d_1–d_4) PRIMER-1.0 moisture perturbations at lead times of (column 1) 1 hour, (column 2) 2 hours, (column 3) 3 hours, and (column 4) 4 hours. In each subplot, the origin is the initial sweet spot location, the black dashed circle demarcates the area in which the initial moisture perturbations were modified, and the color of each contour represents the initial moisture content of each member as in Figure 3.3.

3.3.3 Impact of Initial Moisture Uncertainty on Pathways to Genesis and Genesis Timing

The previous subsection showed that the rapid growth of convective differences to the scale of the pouch occurs due to initial moisture uncertainty within it. This subsection reveals the impacts of those errors on pathways to TCG and TCG timing.

Rapid development of pouch-scale convective differences associated with the initial QVAPOR uncertainty within it can be inferred from meso-β-scale latent heating rates (Figure 3.9). In an ensemble mean sense (Figures 3.9a_1 – 3.9a_4), latent heating rates in each PRIMER forecast follow the same general evolution; however, uncertainty in their magnitude, as shown by the ensemble spread of meso-β-scale latent heating rates (Figures 3.9b_1 – 3.9b_4), increases with initial QVAPOR uncertainty. Although all PRIMER ensembles exhibit peaks in the spread of latent heating rates coincident with the timing of convective bursts shown in the ensemble mean, the PRIMER-1.0 ensemble has noticeably larger uncertainty in the strength of those bursts (Figure 3.9b_4).

The timing of the convective bursts in the ensemble mean latent heating rates reveal a diurnal cycle, especially during the first day of integration. A prominent convective burst occurs during the first six hours of all ensembles, peaking just before sunrise. After sunrise, convection in all ensembles is suppressed until about 30 hours before observed TCG time - the approximate time of sunset. Recall the ensemble spread of intensity remained quasi-steady (Figure 3.6b) and DKE dropped (Figure 3.7) during the daylight hours between 42 and 30 hours before the observed TCG time. During this period, the ensemble spread of meso-β-scale latent heating rates also remains quasi-steady or decreases slightly. At around 30 hours before the observed TCG time, the sun begins to set, and another round of convective intensification starts. This new round of convection leads to an increase once again in the mean and spread of latent heating rates. Thus, the diurnal cycle of convection may have played a major role in the further growth of convective differences among members. The impact of the diurnal cycle on deep convection, as well as TCG and intensification, has been illustrated by numerous other studies (e.g., Hobgood

1986; Craig 1996; Ge et al. 2014; Melhauser and Zhang 2014; Tang and Zhang 2016; Bell and Montgomery 2019; Dunion et al. 2019; Ruppert et al. 2020; Wing 2022; Chen et al. 2023).

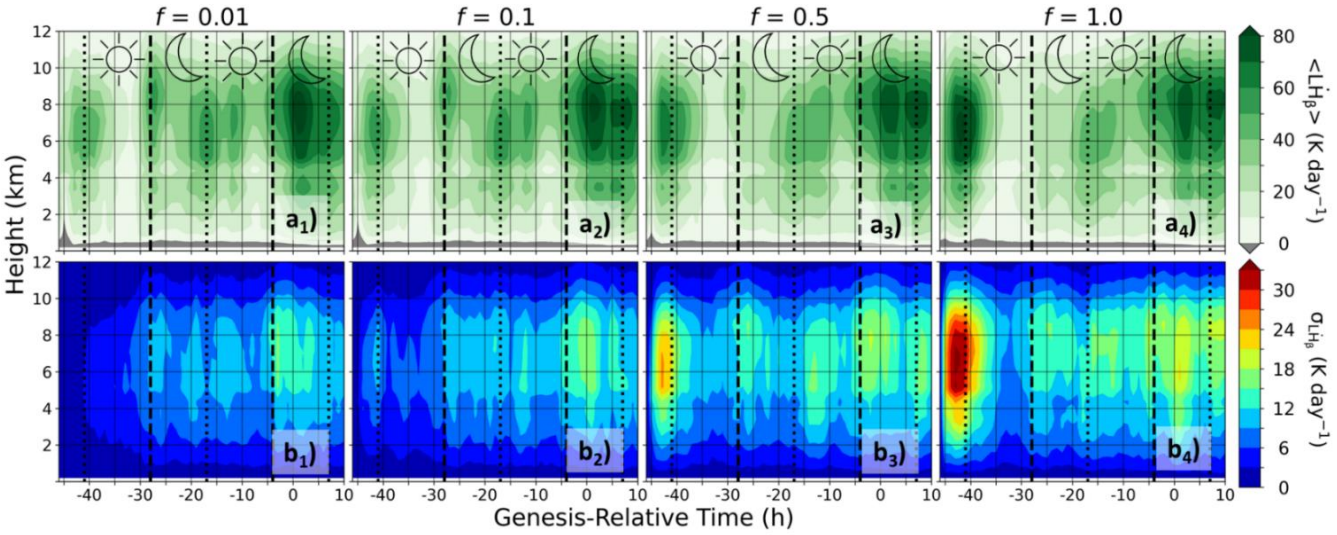

Figure 3.9. Temporal evolution of the (a_1-a_4) ensemble mean and (b_1-b_4) ensemble spread of the meso-β-scale latent heating rates (K day^{-1}) for the ensemble initialized with (a_1,b_1) PRIMER-0.01, (a_2,b_2) PRIMER-0.1, (a_3,b_3) PRIMER-0.5, and (a_4,b_4) PRIMER-1.0 moisture perturbations. The meso-β-scale latent heating rate at each time was found by averaging the latent heating rates within a 2° x 2° box centered on the storm center. In each subplot, dotted vertical lines indicate sunrise and dashed vertical lines represent sunset.

Another intriguing feature in the ensemble mean plots of meso-β-scale latent heating rates is the convective burst during the first six hours of the forecast period, which increases in intensity with increasing initial QVAPOR uncertainty (Figures 3.9a_1 – 3.9a_4). This is a result of the model adjustment process in the first six hours of integration. Since the PSU WRF-EnKF system provides a statistically-based update to the state, some degree of deviation from physical reality is to be expected in the analysis. More specifically, the PSU WRF-EnKF may try to build clouds in columns where the moisture or vertical motion is insufficient. Upon initialization, some of the convection in those columns will dissipate as the model is integrated. This dissipation process affects the initially moister ensemble members less than the drier ones. Since the ensembles that have the greatest initial QVAPOR uncertainty have more extremely moist members, the dissipation process will affect them less. This explains why the PRIMER-1.0 ensemble has the strongest convective burst during the first six hours of the forecast. The

physical disconnect described here, as well as other forms of disconnect such as physical imbalance (e.g., deviations from geostrophy), are a common feature of DA systems (Houtekamer and Mitchell 2005; Poterjoy and Zhang 2014b) that cannot be avoided when starting from an analysis. How much of the rapid intensity spread growth during the first six hours of integration (Figure 3.6b) results from the unsupported convection present at initialization is unclear; however, it suffices to say that operational models will experience this effect as well.

The bursts of deep convection shown in Figure 3.9 are associated with periods of enhanced low-level convergence through a deep layer while times of suppressed convection experience weaker and shallower low-level convergence (Figures 3.10a_1 – 3.10a_4). Consistent with Figures 3.9a_1 – 3.9a_4, the low-level convergence during the first six hours is progressively deeper and stronger with increasing initial QVAPOR uncertainty. During the daylight hours between 42 and 30 hours before the observed TCG time, the lull in deep convection is accompanied by shallower, weaker low-level convergence. When the sun begins to set around 30 hours before the observed TCG time, the low-level convergence once again grows deeper and stronger with the new round of convection. As with the latent heating rates, all PRIMER ensembles agree on the general trend of the meso-β-scale divergence in an ensemble mean sense (Figures 3.10a_1 – 3.10a_4), but they disagree on the uncertainty of its strength. Based on the ensemble spread of meso-β-scale divergence (Figures 3.10b_1 – 3.10b_4), uncertainty in the strength of low-level convergence associated with convective bursts increases as initial QVAPOR uncertainty increases.

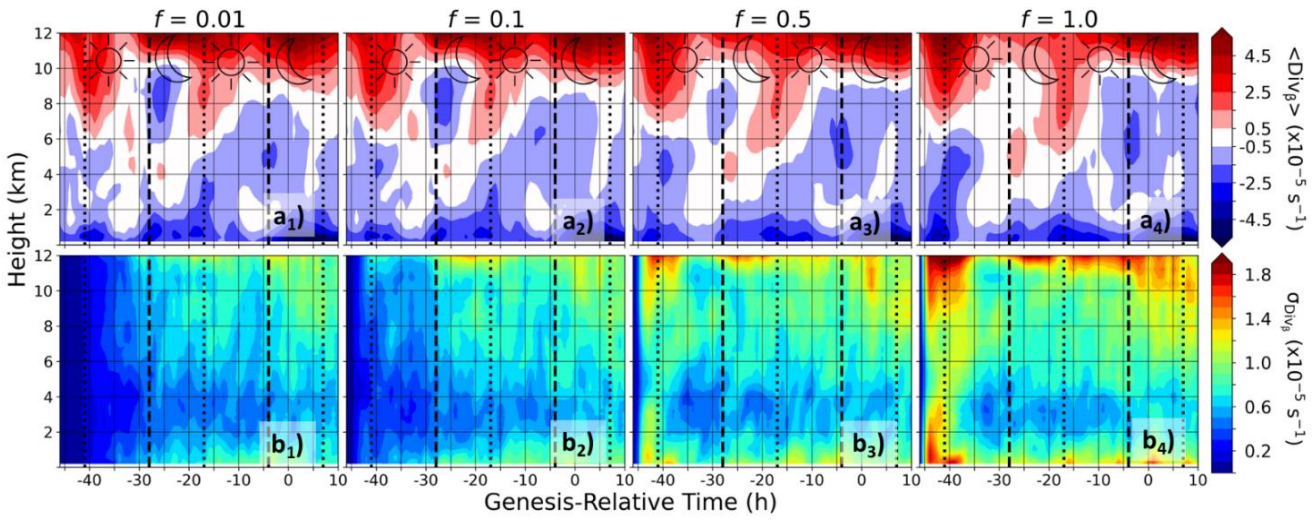

Figure 3.10. As in Figure 3.9, but for the meso-β-scale divergence (x 10^{-5} s^{-1}).

Convective bursts and their associated low-level convergence play a role in the spin-up of the low-level meso-β-scale vortex (Figure 3.11). As with low-level convergence and latent heating rates, all PRIMER ensembles agree on the general trend of the relative vorticity in an ensemble mean sense (Figures 3.11a_1 – 3.11a_4). More specifically, the low-level vortex begins to intensify and extend upwards during the early and late morning hours of the first day (i.e., 42 to 35 hours before the observed TCG time). Around the middle of that day, the vortex at all levels begins to spin-down, with the pattern clearest at low-levels. Shortly after sunset on the first day, the low-level vortex once again begins to spin-up. This time, however, vorticity continues to increase with height and time through the daylight hours of the second day to eventually become a TC. By comparing Figures 3.10a_1 – 3.10a_4 to Figures 3.11a_1 – 3.11a_4, one can see those changes in the low-level vorticity lag changes in the low-level convergence. Consistent with Wang et al. (2010) and Bell and Montgomery (2019), this shows the role of the low-level meso-β-scale convergence associated with convective bursts in helping to spin-up the vortex. An interesting pattern seen in Figures 3.11a_1 – 3.11a_4 is the temporary spin-down of the low-level vortex during the afternoon and evening hours of the first day. This delayed TCG is influenced by the intense convective burst that occurred during the first six hours combined with the subsequent lack of new convection during the daytime hours. Once that convection reaches maturity, evaporatively cooled downdrafts (not shown) reduce the meso-β-scale low-level

convergence, thereby temporarily preventing further spin-up of the low-level vortex. To summarize, convective bursts and their associated low-level convergence contribute to a spin-up of the low-level vortex in an ensemble mean sense, regardless of the initial moisture uncertainty within the pouch.

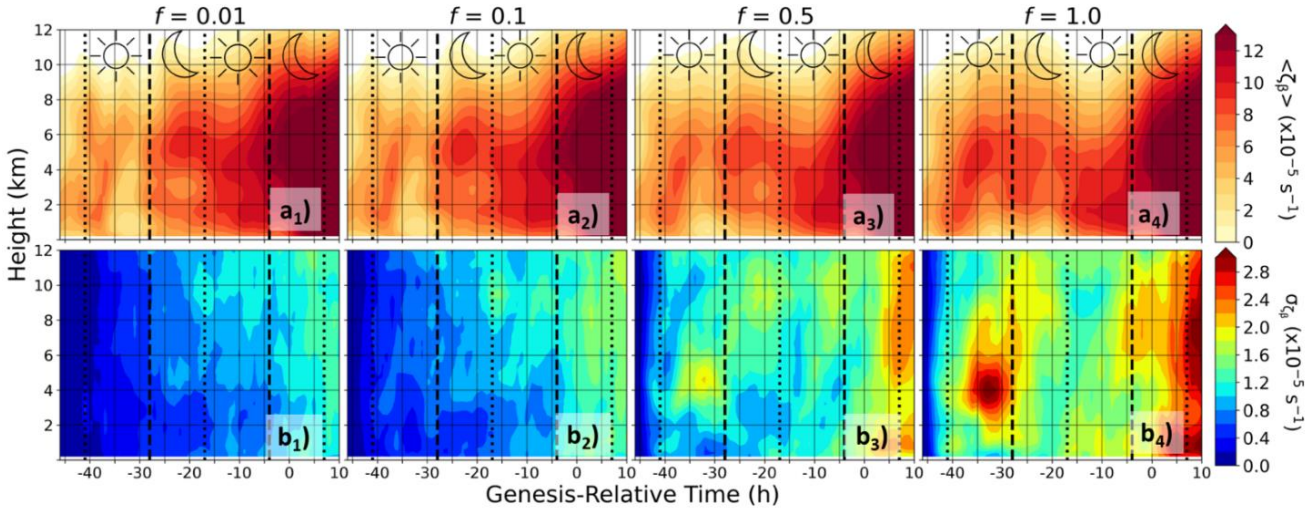

Figure 3.11. As in Figure 3.9, but for the meso-β-scale relative vorticity (x 10^{-5} s^{-1}).

Increasing uncertainty in the initial QVAPOR within the pouch leads to greater uncertainty in the strength of the meso-β-scale vortex at all levels (Figures 3.11b_1 – 3.11b_4). This uncertainty in the strength of the vortex grows rapidly during the early hours, especially for PRIMER-1.0 (Figure 3.11b_4). For PRIMER-1.0, and to a lesser extent PRIMER-0.5 (Figure 3.11b_3), large uncertainty in the strength of the mid-level vortex can be seen in the afternoon hours between 35 and 30 hours before the observed TCG time. This lags the maximum in the ensemble mean mid-level vortex (Figures 3.11a_3, 3.11a_4) by a few hours, indicating uncertainty in the timing of mid-level vortex spin-down when initial QVAPOR uncertainty is greater. Conversely, both PRIMER-0.5 and PRIMER-1.0 display lower uncertainty in the spin-down of the low-level vortex during those afternoon and evening hours. This is likely a result of the lack of new convection during these times. Once the sun sets around 30 hours before the observed TCG time, new convection develops and the low-level vortex eventually spins-up. The ensemble spread of the meso-β-scale relative vorticity subsequently increases in time from the surface

upwards (Figures 3.11b$_1$ – 3.11b$_4$). Ultimately, the timing of the spin-up of the low-level vortex becomes more uncertain as the initial QVAPOR uncertainty within the pouch increases.

The differences in the timing of the spin-up of the low-level vortex shown previously translate to differences in the timing of TCG among members. To corroborate that statement, it is necessary to define the timing of TCG in the simulations. In this study, simulated TCG time refers to the precise hour at which the 700-850 hPa layer-averaged meso-β-scale circulation exceeds a value of 8×10^{-5} s^{-1} and remains above that threshold for the remainder of the forecast period. This threshold value is chosen to be consistent with the study of Majumdar and Torn (2014). Based on the meso-β-scale circulation values plotted in Figure 3.12, uncertainty in the simulated TCG time for this case study increases as the initial moisture uncertainty within the pouch region increases. More specifically, the ensemble spread of the simulated TCG time increases to over six hours as the initial moisture uncertainty reaches that of the full EnKF analysis. The spread of simulated TCG time increases with increasing initial moisture uncertainty because the initially moistest members tend to undergo TCG earlier, as indicated by the correlation between initial moisture content and TCG time. Note that, consistent with Figure 3.5, these correlations become increasingly negative and statistically significant as initial moisture uncertainty within the pouch increases. Ultimately, uncertainty in the simulated TCG times of this case study increases with initial moisture content within the pouch because ensemble members that are initially moister tend to undergo TCG earlier.

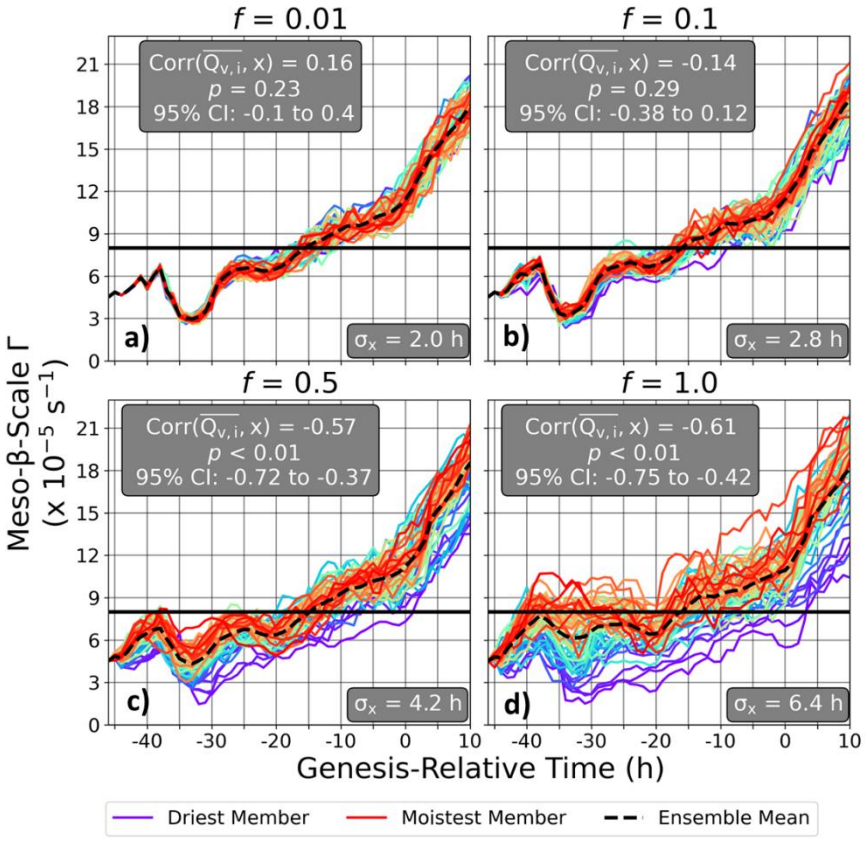

Figure 3.12. Temporal evolution of the meso-β-scale circulation (x 10^{-5} s^{-1}) averaged within the 700-850 hPa layer for the ensemble initialized with (a) PRIMER-0.01, (b) PRIMER-0.1, (c) PRIMER-0.5, and (d) PRIMER-1.0 moisture perturbations. The meso-β-scale circulation at each time was found by averaging the relative vorticity within a 2° x 2° box centered on the storm center. Line colors represent the initial moisture content of each member as in Figure 3.3. The circulation threshold of 8 x 10^{-5} s^{-1} used to identify TCG time in the simulations is demarcated by the solid horizontal black line. Listed in the lower right corner of each subplot is the ensemble spread of simulated TCG time (h). Finally, the upper left corner of each subplot lists the Pearson correlation coefficient (with corresponding p-value and 95% confidence interval) between the volume-averaged QVAPOR within 300 km of the initial sweet spot location and simulated TCG time.

Uncertainty in the simulated timing of TCG due to initial QVAPOR uncertainty within the pouch is a result of uncertainty in the strength and coverage of convective activity on the meso-β-scale. This can be inferred from Figure 3.13, which shows the statistically significant correlations between initial QVAPOR within the pouch and the meso-β-scale averages of latent heating, divergence, and relative vorticity. Based on Figure 3.13, initially moister members tend to produce greater rates of latent heat release (Figure 3.13a), a stronger and deeper layer of low-

level convergence (Figure 3.13b), and a stronger low-level vortex (Figure 3.13c) during the early hours of the forecast. After sunrise on the first day (~ 40 to 35 hours before the observed TCG time), moister members tend to produce evaporative cooling below 4 km as the intense convection they produced has matured by this point. This evaporative cooling coincides with low-level divergence at that time for the initially moist members. Also at that time, the moister members tend to have stronger convergence near 4 km, which is consistent with the top-heavy latent heating profile (Figures $3.9a_1$ – $3.9a_4$) and is related to the prevalence of stratiform precipitation. Shortly thereafter (35 to 30 hours before the observed TCG time), the moister members tend to have a stronger mid-level vortex near 4 km and a greater spin-down (although not statistically significant) of the low-level vortex. As the sun sets that day, the moister members once again begin to release more latent heat at all levels, coincident with a new period of low-level convergence. By the end of the first full night (~ 20 hours before the observed TCG time), the moister members have begun to spin-up the low-level vortex after a prolonged period (~ 10 hours) of enhanced low-level convergence. Ultimately, members that are initially moister tend to form a TC earlier because the intense convection they produce leads to the earlier spin-up of a low-level vortex.

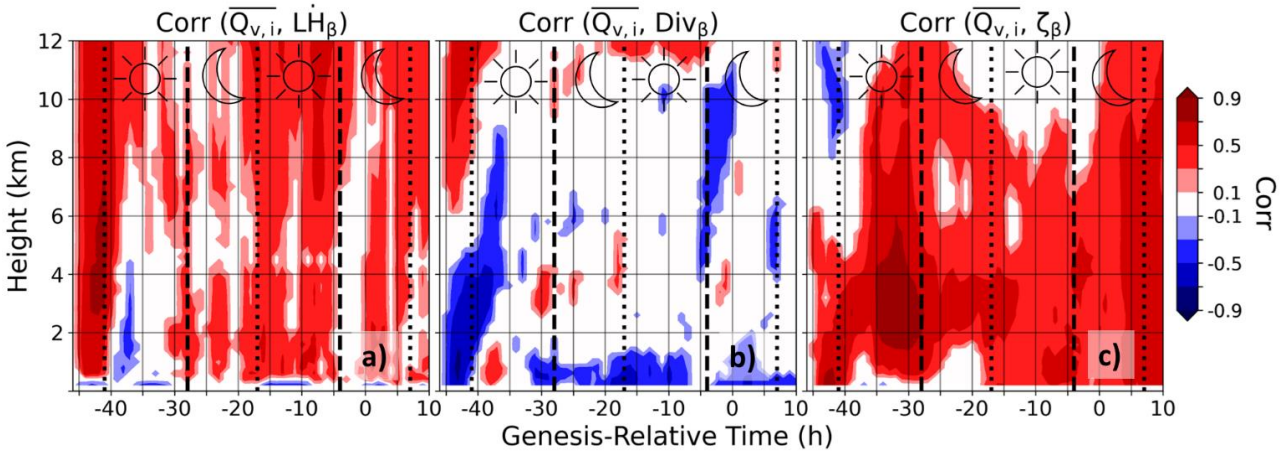

Figure 3.13. Temporal evolution of the Pearson correlation coefficient between the initial-hour volume-averaged QVAPOR within 300 km of the pouch center and the meso-β-scale (a) latent heating rates, (b) divergence, and (c) relative vorticity for the ensemble initialized with PRIMER-1.0 moisture perturbations. Only correlations that are statistically significant at greater than 95% based on the Student's t-test (Gosset 1908) are plotted. The meso-β-scale averages at each time were found by averaging within a 2° x 2° box centered on the storm center. In each subplot, dotted vertical lines indicate sunrise and dashed vertical lines represent sunset.

In this subsection it was shown that, in the context of Hurricane Irma (2017), increasing the uncertainty in the initial moisture content within 300 km of the pouch center does not alter the pathway to TCG; however, it increases the uncertainty in TCG timing since ensemble members with more moisture exhibit an earlier spin-up of the low-level vortex.

3.4 Discussion and Conclusions

This study investigated the impacts of local initial moisture uncertainty within the incipient disturbance that would become Hurricane Irma (2017) on the practical predictability of its formation and subsequent intensification. By comparing an ensemble forecast with only QVAPOR perturbations within the pouch region to one that retained perturbations of all variables domain-wide, it was revealed that initial moisture uncertainty within the incipient disturbance plays a crucial role in determining the predictability of TCG. Upon integration, initial moisture uncertainty causes the rapid growth of MCS intensity and dislocation errors that overwhelm the pouch region within a couple hours. Eventually, pouch-scale differences in convection lead to a variety of TCG timings, with initially moister members spinning-up a low-level vortex earlier. As initial moisture uncertainty is reduced by shrinking perturbations to QVAPOR, pouch-scale convective differences are slower to grow, and TCG timing is constrained.

This study suggests the practical predictability of TCG may be improved by reducing initial moisture uncertainty within the incipient disturbance of potential TCs. Consequently, it provides motivation to target this small, but critical region, for high resolution observations that modern DA systems can use to constrain the initial moisture within it. All-sky IR and MW observations, such as in this study, are one type of observation that can reduce moisture uncertainty. Beyond that, high resolution in-situ moisture observations at all levels within the disturbance will likely be needed (e.g., from a dense dropsonde network). Before such an investment, future studies should confirm the robustness of these results with other storms, given the strong case-to-case variability in TCG predictability associated with various flow regimes (Sippel et al. 2011; Melhauser and Zhang 2012; Torn and Cook 2013; Komaromi and Majumdar 2015). Future studies should also confirm the robustness of these results with higher resolution

models that better resolve convective scale motions - both Zhang et al. (2003) and Zhang et al. (2007) revealed that initial growth of errors becomes faster as resolution is increased. Another limitation of this study is that it neglects the potential impacts of initial moisture uncertainty within the environment. Finally, the spin-down of the model during the first six hours of integration, as well as using a single forecast model and DA system, are just some of the other limitations. Nevertheless, this study reveals a glimmer of hope. Not only does it show the improvement that can be brought to TCG forecasts by constraining moisture within a small region, but it also suggests TCG might be more predictable than it seems. The latter point can be realized by noting perturbations to initial moisture well below the amplitude of any observation system at one model level in a small region leads to forecast uncertainty well below that of forecasts initialized from typical analysis uncertainty in all variables domain-wide (Figure 3.6a).

These results lead to some very interesting questions that are worth pursuing in the future. For example, how does the impact of initial moisture uncertainty within the pouch region compare to that of initial moisture uncertainty within the environment? Also, does constraining the initial moisture at certain vertical levels within the pouch impact the predictability of TCG more than others? Another factor worth considering is the influence of the diurnal cycle of convection on the predictability of TCG. This study revealed the delayed TCG that occurred in the daylight hours on the first day. How might the results differ if the forecasts were initialized during different parts of the diurnal cycle? These are some of the questions that should be pursued in the future.

Data Availability Statement

Initial conditions for all ensemble forecasts presented in this study can be freely downloaded from the Penn State Data Commons (https://doi.org/10.26208/15Q9-MM49). All assimilated GTS observations were obtained from datasets 351.0 and 461.0 of the NCAR Research Data Archive (https://rda.ucar.edu). All assimilated Meteosat-10 SEVIRI Channel 5 BTs were ordered from the EUMETSAT Data Centre (https://www.eumetsat.int/eumetsat-data-centre). All assimilated MW BTs were downloaded from NASA GPMs Precipitation Processing System (https://storm.pps.eosdis.nasa.gov/storm/).

Chapter 4

Improving the Analysis and Forecast of Hurricane Dorian (2019) with Simultaneous Assimilation of GOES-16 All-Sky Infrared Brightness Temperatures and Tail Doppler Radar Radial Velocities

ABSTRACT

Recent studies have shown that assimilation of all-sky IR observations can be beneficial for TC analyses and predictions. The assimilation of TDR radial velocity observations has also been shown to improve TC analyses and predictions; however, there is a paucity of literature on the impacts of simultaneously assimilating them with all-sky IR BTs. This study examines the impacts of assimilating combinations of GOES-16 all-sky IR BTs, NOAA P-3 TDR radial velocities, and conventional observations from the GTS network on the analyses and forecasts of Hurricane Dorian (2019). It is shown that including IR and/or TDR observations on top of conventional GTS observations significantly reduces both track and intensity forecast errors. Track errors are reduced the most (25% at lead times greater than 48 h) when TDR and GTS observations are assimilated. In terms of intensity, errors are always lower at lead times greater than 48 h when all-sky IR BTs are assimilated. Simultaneously assimilating TDR and IR observations has the potential to further improve the intensity forecast by as much as 37% at a lead time of 48 h to 72 h. The improved intensity forecasts produced by the experiments assimilating all three observation sources are shown to be a result of the competing effects of IR assimilation producing an overly broad area of strong cyclonic circulation and TDR assimilation constraining that circulation to a more realistic size and intensity.

4.1 Chapter Introduction

TCs are among the deadliest and costliest natural disasters. Of the billion-dollar weather and climate disasters that have afflicted the United States since 1980, TCs rank first in terms of both fatalities and cost to the economy (Smith 2020). Improving upon track and intensity forecasts is thus of great societal value.

Over the last couple decades, average track errors of the NHC 72-h hurricane forecasts have more than halved, whereas the 72-h forecasts of maximum surface wind speed have seen less improvement over the same time period (Cangialosi 2020). The relatively slow improvement in TC intensity forecasting has been attributed to a number of difficulties. These difficulties include the challenges associated with accurately simulating and predicting small-scale nonlinear features such as moist convection over the hurricane inner core region (e.g., Hendricks et al. 2004; Krishnamurti et al. 2005; Montgomery et al. 2006; Rotunno et al. 2009; Zhang and Weng 2015; Christophersen et al. 2017), model physics deficiencies regarding TC inner core dynamics (e.g., Bao 2016; F. Zhang et al. 2017; Zhang 2018; Rajeswari et al. 2020), the lack of sufficient TC inner core observations (e.g., Pu et al. 2016), and our incomplete understanding of air-sea interactions at high wind speeds (e.g., Green and Zhang 2014; Andreas et al. 2015; Chen and Zhang 2019; Nystrom et al. 2020; Chen et al. 2021b). TC intensity forecast errors are also greatly influenced by initial intensity and structure errors within the TC inner core vortex, which makes prediction of RI especially challenging (Emanuel and Zhang 2016). In addition to minimizing initial intensity and structure errors, it is also important to properly initialize inner core moisture (Emanuel and Zhang 2017), something which is not easily observed.

In order to minimize initialization errors in the TC inner core vortex, a number of studies have used DA systems to assimilate either ground-based (e.g., Osuri et al. 2015; Zhu et al. 2015; Shen et al. 2016, 2020) or airborne (e.g., Aberson et al. 2015; Zhang and Weng 2015; Tong et al. 2018; Nystrom and Zhang 2019) Doppler radar observations. Collectively, these studies show that assimilating Doppler radar radial velocities reduces both track and intensity errors relative to assimilating only conventional GTS observations. These improvements are due to better representation of TC initial position and inner core dynamic structures.

Despite the improvements brought to TC forecasts from assimilating Doppler radar radial velocities, there are some challenges associated with their assimilation. For example, because the radar observations come in high quantities and a resolution significantly higher than the model grid used, substantial data thinning and quality control must be implemented (Zhang et al. 2009). Moreover, Doppler radar observations over the ocean lack continuous spatial and temporal coverage.

In contrast, observations from the new generation geostationary satellites (e.g., GOES-16 and Himawari-8) have continuous coverage. The benefits of assimilating satellite all-sky IR observations on convection-permitting analysis and prediction of TCs were first explored in the pilot work of Zhang et al. (2016). Motivated by the strong ensemble correlations between simulated water vapor channel BTs and model state variables (e.g., moisture and winds), Zhang et al. (2016) assimilated BTs into an ensemble of convection-permitting simulations of Hurricane Karl using an EnKF. They found that assimilating all-sky IR BTs improved both the analyzed thermodynamic fields and the intensity forecast of Hurricane Karl. Subsequent studies (e.g., Honda et al. 2018; Minamide and Zhang 2018; F. Zhang et al. 2019) have further highlighted the benefits of assimilating all-sky IR BTs. These more recent studies have shown that TC structure (both inner core and outer rain bands) is better captured when all-sky IR BTs are assimilated. These improved cloud and moisture structures, combined with a more resilient TC vortex, resulted in better intensity forecasts.

Despite the benefits of assimilating all-sky IR BTs, at the time of writing, all-sky IR BTs have yet to be assimilated operationally (Geer et al. 2019) due to inherent difficulties. One problem with satellite observations is that they tend to be biased relative to their model equivalents and removing these biases is not straightforward (Eyre 2016; Otkin et al. 2018). Additionally, models have trouble predicting the exact location and intensity of clouds, which leads to highly non-Gaussian errors that are introduced into DA systems that assume Gaussian error distributions (Geer and Bauer 2011; Chan et al. 2020a). These mismatches between observed and simulated cloud scenes also lead to large representativeness errors that must be accounted for (Minamide and Zhang 2017). Finally, the relationship between cloudy-sky BTs

and atmospheric states is highly nonlinear (Bauer et al. 2011; Geer and Bauer 2011), which makes construction of an accurate forward model challenging.

Given the inherent strengths and weaknesses of assimilating either Doppler radar radial velocities or all-sky IR BTs, it is surprising that no studies to date have assimilated both. In this study, the potential improvements brought to TC analyses and forecasts by leveraging the benefits of assimilating GOES-16 all-sky IR BTs as well as NOAA P-3 TDR radial velocities are explored. The case of Hurricane Dorian (2019), a powerful storm whose RI was poorly modeled by most operational centers (Avila et al. 2020), is used as a testbed for this study. This storm was also selected for the study due to the abundance of TDR observations available both before and during its RI.

4.2 Data and Methodology

In this section a brief summary of the life of Hurricane Dorian is provided. The DA system and forecast model utilized for this study is then introduced. After describing the observations used, the section is concluded with an illustration of the experimental design.

4.2.1 Description of Hurricane Dorian

Dorian formed from a tropical wave originating off the west coast of Africa and became a named storm on 25 August 2019 as it drifted westward toward the Lesser Antilles. Over the next few days Dorian remained a tropical storm as it traversed the islands of the Lesser Antilles. The system thereafter curved to the north, putting it in a more favorable environment for development. Hurricane Dorian then began to rapidly intensify north of the Virgin Islands on 30 August. Hurricane Dorian eventually made landfall on 1 September, ravaging the Bahamas with 1-min sustained winds of 185 mph (Avila 2019) and making it one of the strongest Atlantic hurricanes at time of landfall.

4.2.2 The DA and Forecast System

This study used the PSU-EnKF system, which is based on the ensemble square-root filter (EnSRF) proposed by Whitaker and Hamill (2002). The PSU-EnKF system was first used in an observing system experiment (OSE) framework by Meng and Zhang (2008). In its current form, the PSU-EnKF system performs the DA in joint state-observation space, which is described by Eqs.(1) and (2) of Chan et al. (2020a). To assimilate BTs in this study, the CRTM (Han et al. 2006, 2007; Weng 2007) release 2.1.3 was used to convert from model state space to observation space. An ensemble of 60 members was used and 75% relaxation to prior perturbations (Zhang et al. 2004) was applied in order to prevent filter divergence.

The WRF model for the cycling EnKF system was configured similar to the real-time PSU-EnKF TC analysis and prediction system (Zhang and Weng, 2015), with three two-way nested domains having horizontal grid spacings of 27 km, 9 km, and 3 km. The nested domain with 9-km grid spacing was 2700 km x 2700 km, whereas the nested domain with 3-km grid spacing was 900 km x 900 km. Domain configuration and parameterization schemes were nearly identical to F. Zhang et al. (2019). All three domains had 43 vertical levels with model top at 10 hPa. The Tiedtke (1989) cumulus parameterization scheme was only applied to the coarsest (27-km) domain whereas all three domains made use of the WRF single-moment 6-class mixed-phase microphysics scheme (WSM6; Hong and Lim 2006), the Yonsei University planetary boundary layer scheme (Hong et al. 2006), and the RRTM longwave and shortwave radiation schemes (Iacono et al. 2008). Surface fluxes of sensible and latent heat, as well as momentum, were parameterized via Eqs. (11) – (13) of Green and Zhang (2013).

4.2.3 The Observations

Observations assimilated in this study fell into three categories: conventional observations from the GTS, TDR radial velocities collected by the NOAA P-3 aircraft, and IR BTs from Channel 8 of the GOES-16 ABI instrument. Conventional GTS observations were assimilated in all three domains whereas TDR and IR observations were assimilated in the 3-km domain (D3) only.

The conventional GTS observations assimilated in this study include hurricane position and intensity (HPI) from the "TC Vitals" database, as well as radiosondes, dropsondes, and METAR data. In order to eliminate the effects of spurious long-distance correlations, the Gaspari and Cohn (1999) fifth-order piecewise polynomial was applied to localize ensemble covariance. The localization ROI in the vertical was 43 vertical levels for all observations. Consistent with F. Zhang et al. (2019), the horizontal ROI was 300 km for HPI and METAR and 90 km for radiosondes and dropsondes. During assimilation, observation errors for these observables were those specified by version 3.6.1 of the WRFDA package. For quality control purposes, METAR and sounding observations were discarded if the absolute value of the observation increment (also known as the "innovation") was greater than five times the observation error.

The TDR observations assimilated in this study were obtained from the NOAA Hurricane Research Division (HRD). These observations were first preprocessed by HRD using the super-observation procedure outlined in Weng and Zhang (2012, 2016). These super-observation radar data have a spacing of 5 km in the radial direction and 5° in the azimuthal direction. Further thinning to every 10^{th} super-observation resulted in an average distance between TDR super-observations of approximately 23 km. When assimilating TDR super-observations, Gaspari and Cohn (1999) covariance localization was employed together with the Successive Covariance Localization (SCL) procedure described in Zhang et al. (2009). As per SCL, large-scale features were first corrected by randomly selecting a ninth of the thinned TDR super-observations and assimilating them with an ROI of 405 km. Smaller-scale features were then corrected by randomly assimilating two ninths of the thinned super-observations with an ROI of 135 km and the remaining super-observations with an ROI of 45 km. The vertical ROI for all super-observations was 43 vertical levels. Consistent with Zhang et al. (2009), the observation error for all TDR super-observations was assumed to be 3 m s^{-1}. As with the conventional GTS observations, a TDR super-observation was discarded if the absolute value of the observation increment was more than five times the observation error.

The GOES-16 ABI all-sky IR BTs assimilated in this study came from Channel 8 (6.2-μm wavelength), which is sensitive to upper-tropospheric water vapor (Schmit et al. 2005). The raw BT data has a horizontal resolution of approximately 2 km. As in F. Zhang et al. (2019), a

form of SCL was performed on the IR BTs such that BT observations thinned every 12 km had a 30-km horizontal ROI and observations thinned every 18 km had a 200- km horizontal ROI. No vertical localization was applied when assimilating BT observations. As mentioned in the chapter introduction, assimilating all-sky IR BTs can sometimes lead to large representativeness errors. To deal with this problem, AOEI was employed. AOEI is a method that was introduced by Minamide and Zhang (2017) to adaptively adjust observation errors to limit erroneous analysis increments associated with representativeness errors. Note that this study did not reject any IR observations because the observation error is adaptively adjusted by using AOEI. In addition, ABEI (Minamide and Zhang 2019) was applied to deal with situations in which the model erroneously predicted clear skies despite cloudy observations. This method uses an empirically-derived spatially-varying multiplicative inflation factor that inflates the state vector components associated with erroneously predicted clear sky regions within each member of the prior ensemble. However, it does not create cloud particles at the analysis step. Instead, it increases the likelihood of developing clouds by increasing the ensemble spread. Following F. Zhang et al. (2019), bias correction was not performed on the GOES-16 IR BTs used in this study. Previous studies (e.g., Zhang et al. 2018, F. Zhang et al. 2019) have shown that, based on the statistics of innovations throughout EnKF cycling, there is no significant bias in the system. This was confirmed for the current study as well (figure not shown).

The setup of the experiments in this study were based on the setup of the PSU-EnKF real-time TC forecast system described in Zhang and Weng (2015) and F. Zhang et al. (2019). Data thinning and localization of IR BTs and TDR observations in the PSU system have been extensively tuned over several years in order to achieve a statistically improved TC intensity forecast result in the real-time system (e.g., Zhang et al. 2011; Weng and Zhang 2012; Zhang and Weng 2015; Zhang et al. 2016; Minamide and Zhang 2017, 2018; F. Zhang et al. 2019). Hence, the same setup for the experiments in this study was used. Although it is possible that the experimental results in this study may be further improved by fine-tuning of data thinning and localization, doing so is beyond the scope of this study.

4.2.4 The Experimental Design

A schematic of the experimental design of this study is provided in Figure 4.1. The design of these experiments was to mimic near-operational cycling DA systems (similar to the configuration of the real-time PSU-EnKF TC analysis and prediction system) that assimilate different observation types. The initial and boundary conditions for this study came from the NCEP GFS analysis at 00 UTC 27 August. A 60-member ensemble was initiated at this time by adding perturbations to the GFS analysis using WRFDA's CV3 background error covariance (Barker et al. 2004). At that time, Dorian was still a weak tropical storm with a maximum sustained wind speed of 45 kt and a minimum central pressure of 1005 mb. The ensemble was then integrated with WRF for 12 h to develop flow-dependent ensemble statistics before assimilating the first observations at 12 UTC 27 August. Because no TDR observations were available at that time, the ensemble became the background for the GTS Only and GTS+IR experiments. The GTS Only experiment assimilated only the conventional observations whereas the GTS+IR experiment assimilated the IR BTs after the conventional observations. These two cycling experiments continued assimilating observations every hour up to and including 00 UTC 29 August. There was a total of 4,455 conventional GTS observations available within domain 3 of the GTS Only experiment over the course of the 37 cycles. This translates to an average of approximately 120 observations per cycle. The number of conventional GTS observations available in any particular cycle varied widely, with the number being as high as 456 at the 23 UTC 28 August cycle and as low as 1 (the HPI observation) at the 09 UTC 28 August cycle. The number of IR BTs assimilated in each cycle was approximately 8,000.

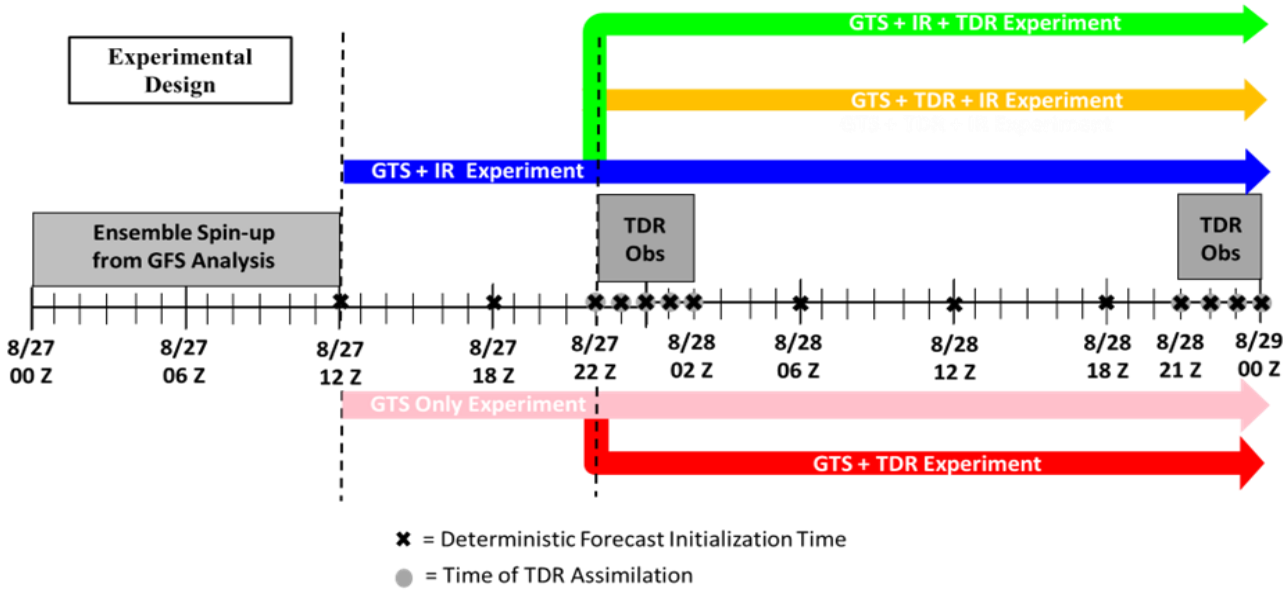

Figure 4.1. Overview of the experimental design. The names of the hourly cycling experiments indicate the order in which each observation type was assimilated. Black 'x's indicate the times at which deterministic forecasts were initialized from the analysis means of the experiments and gray circles indicate hours that TDR observations were assimilated. Note that the GTS+TDR experiment was initialized from the background of the GTS Only experiment at 22 UTC 27 August whereas the experiments that assimilated all observation types were initialized from the background of the GTS+IR experiment at 22 UTC 27 August.

TDR observations were available starting 22 UTC 27 August. At that time, the GTS+TDR experiment was initialized from the background of the GTS Only experiment. This experiment assimilated TDR observations after conventional GTS observations and was cycled forward to 00 UTC 29 August. Note that, from 03 UTC 28 August through 20 UTC 28 August, TDR observations were not available. During that time, only conventional GTS observations were assimilated each hour in the GTS+TDR experiment. In addition to the GTS+TDR experiment, two more experiments were conducted that assimilated all three types of observations: GTS+TDR+IR and GTS+IR+TDR. The only difference between these last two experiments is the order in which observations were assimilated. Both experiments were initialized at 22 UTC 27 August from the background of the GTS+IR experiment and cycled forward to 00 UTC 29 August. During the window when TDR observations were not available, both experiments assimilated conventional GTS followed by IR BT observations each hour. An

average of 2,381 TDR observations were assimilated per cycle during the nine cycles when TDR observations were available and an average of 1 TDR observation per cycle was rejected. These values did not vary across experiments.

As a metric of assessing the value of assimilating these observations, 5-day (120-h) convection-allowing deterministic forecasts were initialized from the analysis mean of each experiment at the times indicated by the black 'x's in Figure 4.1. These deterministic forecasts utilized the same WRF physics options described earlier in this section.

4.3 Results

This section is divided into two parts. The first part shows the impacts of assimilating all-sky IR BTs on the analyses and forecasts of Hurricane Dorian prior to the first TDR cycle, whereas the second part shows the impacts of simultaneously assimilating TDR and IR observations.

4.3.1 Impacts of IR BT Assimilation

Before looking at the impacts of simultaneous assimilation of TDR radial velocity and IR BT observations, the impacts of assimilating all-sky IR BTs on the analyses and forecasts of Hurricane Dorian prior to the first TDR cycle are discussed. This discussion begins with deterministic forecasts of Dorian's track. All deterministic forecasts initialized from the first cycle's analyses show large track errors (Figure 4.2a_1). The first cycle's track forecast in GTS Only is the closest to the best track, followed by that of the GTS+IR. Note that the first cycle's track forecast in the GTS+IR is comparable to that of the Hurricane Weather Research and Forecasting (HWRF) model as well as the official forecast of the NHC (OFCL). By 18 UTC 27 August, continued cycling of DA has reduced track errors of both GTS Only and GTS+IR (Figure 4.2a_2). At this time, the GTS+IR track is comparable to the GTS Only experiment and slightly better than both HWRF and OFCL.

In terms of intensity, the GTS+IR experiment produces higher maximum wind speeds than the GTS Only experiment after only one cycle (Figure 4.2b_1). However, both experiments, as well as HWRF and OFCL, fail to capture the RI of Hurricane Dorian with forecasts starting at

12 UTC 27 August. Continued cycling of observations leads to dramatically improved intensity forecasts starting at 18 UTC 27 August (Figure 4.2b$_2$). Although the GTS+IR intensity forecast initialized at this time does not predict the category 5 status Dorian would become, this forecast closely mirrors the RI from 18 UTC 27 August to 18 UTC 30 August seen in the best track values. In contrast, the GTS Only experiment, as well as HWRF, exhibit a delayed intensification relative to the GTS+IR experiment, while OFCL misses the intensification altogether.

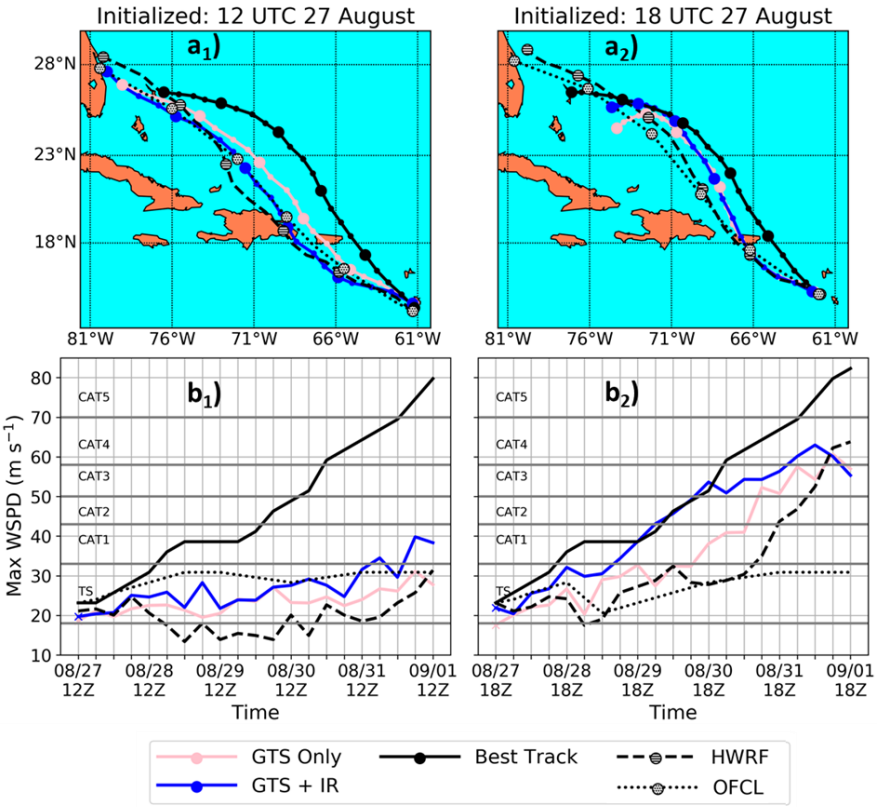

Figure 4.2. Deterministic forecasts of (a) track and (b) intensity initialized from the EnKF analysis means of the (1) first (12 UTC 27 August) and (2) seventh (18 UTC 27 August) cycles of the experiments that did not assimilate TDR. Large circles on track plots denote the first hour of each day. For comparison, best track values from the NHC HURDAT2 database, as well as the operational HWRF and NHC official forecasts, are shown.

To understand why the GTS+IR experiment produced an improved intensity forecast starting at 18 UTC 27 August, attention can be turned to the analyzed and forecasted wind fields and cloud structures. Figure 4.3 illustrates that the initial primary circulation of the GTS+IR experiment (Figure 4.3b$_1$) is stronger, broader, and deeper than the GTS Only experiment (Figure

4.3a_1). As this stronger circulation is integrated in time, it intensifies faster than the GTS Only circulation (Figures 4.3a_2, 4.3a_3 compared to Figures 4.3b_2, 4.3b_3). Additionally, the radius of maximum wind (RMW) of the GTS+IR experiment shows a faster contraction, especially below 4 km, during the first 48 hours of the forecast. This contraction is noticeable in the GTS Only experiment but is less pronounced.

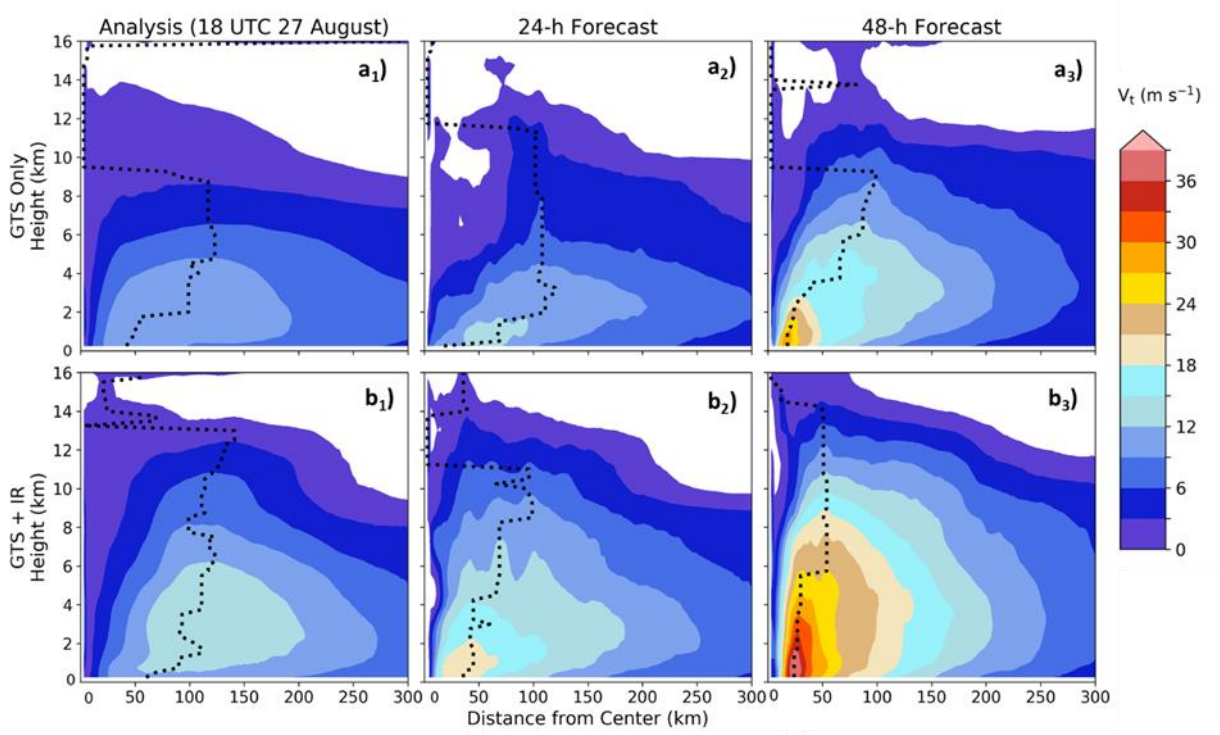

Figure 4.3. Azimuthally averaged tangential velocities of the EnKF analysis mean at the time of the seventh cycle (18 UTC August 27) for the (a_1) GTS Only and (b_1) GTS+IR experiments, as well as the (a_2,b_2) 24-h and (a_3,b_3) 48-h deterministic forecasts initialized from those analyses. The RMW is denoted by the black dotted line.

The GTS+IR experiment not only produces a stronger primary circulation, but also a stronger secondary circulation. This can be seen in Figure 4.4. At analysis time, the GTS+IR experiment displays a much stronger outflow at upper levels. Low-level inflow in the GTS+IR analysis is also slightly stronger than the GTS Only analysis in the region centered around 50 km from the TC center. When forecasts are initialized from these analyses, the GTS+IR forecast of

low-level inflow grows relative to the GTS Only forecast. This low-level inflow advects angular momentum from the outer regions to the TC inner core region, which helps to spin up the vortex. Consequently, the GTS+IR experiment better captures the RI of the storm than the GTS Only experiment.

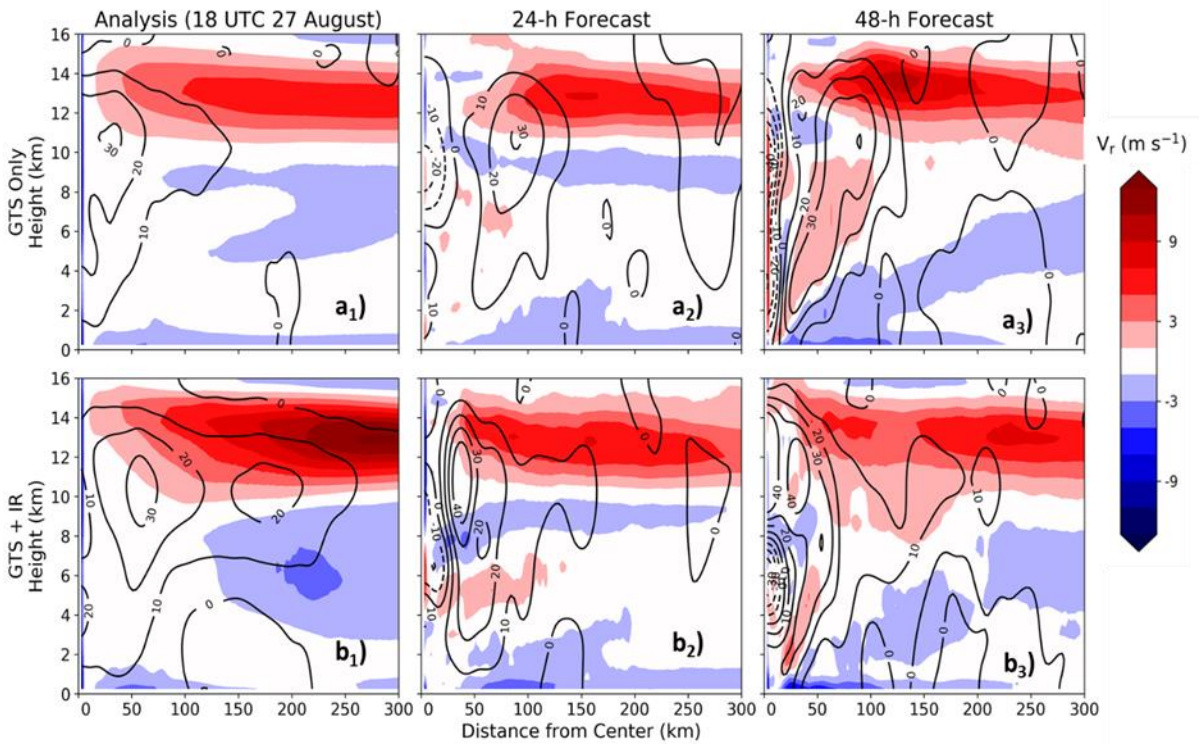

Figure 4.4. As in Figure 4.3, but for azimuthally averaged radial velocities. Black contours show azimuthally averaged vertical velocities in cm s^{-1}, with negative values dashed. Note that a Gaussian smoother was applied to the analysis vertical velocities with a smoothing length scale of 6 km in the horizontal and 0.5 km in the vertical. The Gaussian smoothing length scale for forecasted vertical velocities was 9 km in the horizontal and 0.75 km in the vertical.

In addition to stronger primary and secondary circulations, the GTS+IR experiment develops more convective activity than the GTS Only experiment (Figure 4.5). At analysis time, the azimuthally-averaged reflectivities of each experiment are fairly similar; however, the GTS+IR analysis has a rainband that extends from 125 to 200 km from the TC center. From the analysis to the 24-h forecast, there are large drop-offs in reflectivity in both experiments, which will be explained shortly. The key feature of Figure 4.5 is the difference between experiments

from the 24-h to 48-h forecasts. As the analyses are integrated forward in the forecasts, the GTS+IR forecast develops areas of higher reflectivity that expand outward and deepen. The enhanced convection in the GTS+IR forecast, compared to the GTS Only forecast, is consistent with the stronger vertical motions illustrated in Figure 4.4.

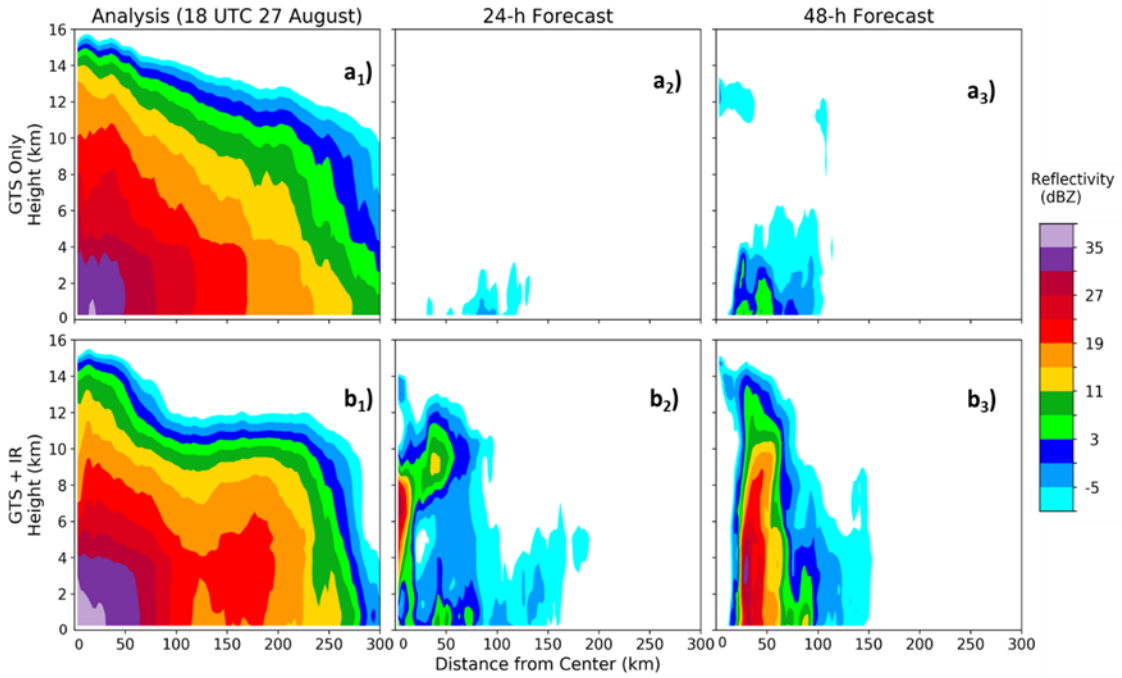

Figure 4.5. As in Figure 4.3, but for azimuthally averaged reflectivity.

The large drops in reflectivity from the analysis to the 24-h forecasts in both experiments is a result of integrating the ensemble mean to make the forecast. Because clouds and precipitation are tied to the vertical velocity field, and thus near-surface convergence, one would expect the evolution of reflectivity to mirror that of the near-surface convergence field. As it turns out, the near-surface convergence fields of the analyses (not shown) are quite weak with very isolated small-scale maxima and minima, the result of averaging dislocated near-surface convergence fields from ensemble member to ensemble member. Consequently, when the

ensemble means are integrated forward to make forecasts, the clouds that exist in the analyses quickly die off. The forecasts then gradually develop clouds and precipitation over time as they reconstruct the small-scale convergence patterns. Notice that the forecast reconstructs the convection sooner in the GTS+IR experiment than in the GTS Only experiment. This is because the small-scale features of the convergence fields in the individual GTS+IR ensemble members are stronger and less dislocated than in the GTS Only experiment, by virtue of the assimilation of all-sky IR BTs.

To see the impact of assimilating IR BTs on the simulated cloud structures, the simulated Channel-10 BTs are compared to those that were observed. GOES-16 ABI Channel 10 (7.3-μm wavelength), which is sensitive to lower-tropospheric water vapor (Schmit et al. 2005), is treated as an independent observation for verification in Figure 4.6. At analysis time, the GTS Only experiment (Figure 4.6a_1) fails to capture the structure of the clouds. The GTS+IR experiment (Figure 4.6b_1) does display many of the small-scale convective features seen in the observations (Figure 4.6c_1). Integrating these analyses forward in time, the GTS+IR cloud structures evolve more similarly to the observations than those of the GTS Only experiment. After 54 h of integration, the GTS+IR forecast better captures the large area of deep inner core convection, as well as the primary spiral rainband, than the GTS Only forecast (Figures 4.6a_4,4.b_4,4.6c_4). The trouble the GTS Only experiment has in producing and sustaining clouds is quantified by its inner core warm bias (Figures 4.6a_2 – 4.6a_4). This is not as problematic in the GTS+IR experiment, which has an inner core bias that is cold to slightly warm (Figures 4.6b_2 – 4.6b_4). Ultimately, the GTS+IR experiment better captures the cloud structures than the GTS Only experiment.

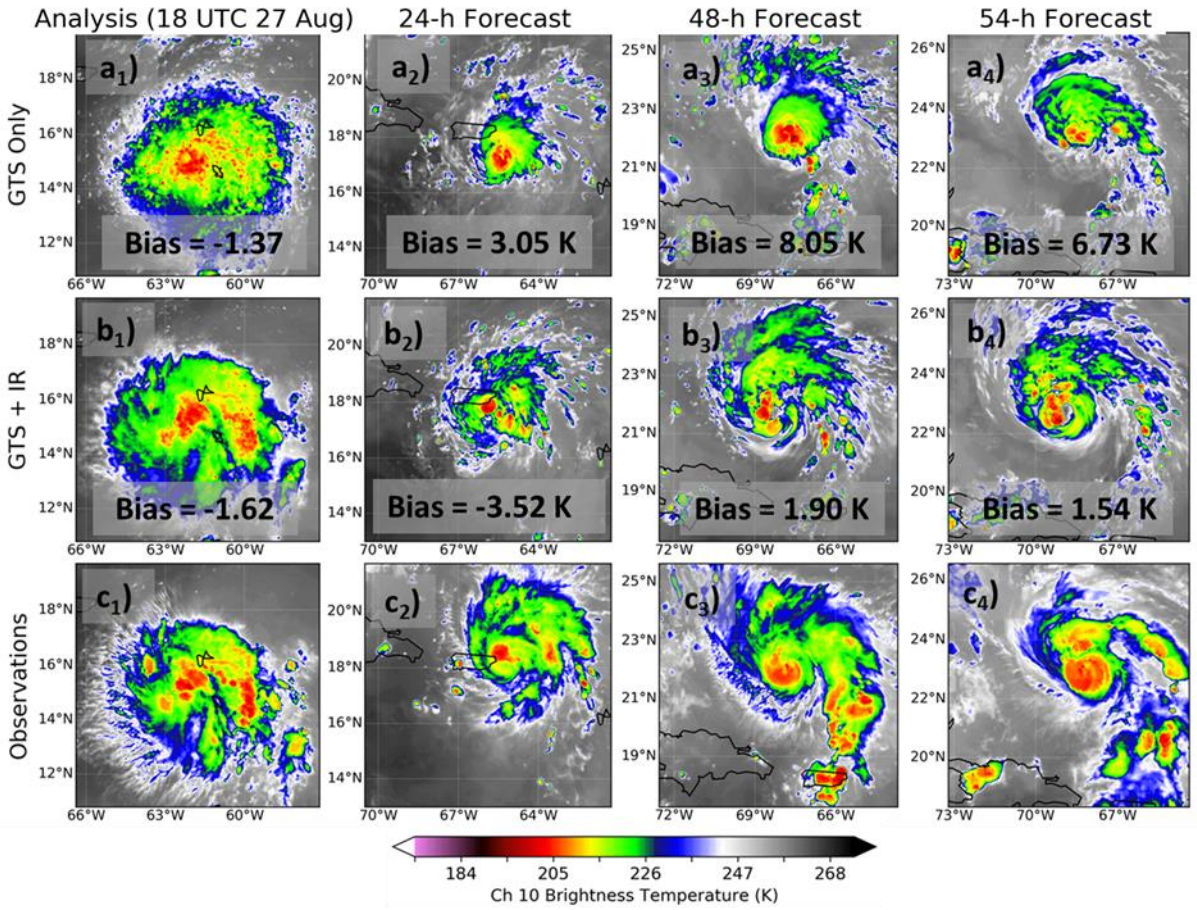

Figure 4.6. Comparison of the simulated Channel-10 BTs of the EnKF analysis mean at the time of the seventh cycle (18 UTC 27 August) for the (a_1) GTS Only and (b_1) GTS+IR experiments to (c_1) observations. Comparisons of the (a_2,b_2) 24-h, (a_3,b_3) 48-h, and (a_4,b_4) 54-h deterministic forecasts initialized from those analyses are also made to (c_2-c_4) observations. Bias values reported in rows (a) and (b) were calculated for the simulated BTs within 300 km of the TC center, with negative values indicating simulated BTs that are lower than observed.

To further assess the intensity and structure of simulated surface wind fields, the simulated surface winds are compared to those retrieved by NOAA/HRD's Stepped Frequency Microwave Radiometer (SFMR). This instrument, which is flown aboard the P-3 aircraft, has a downward-pointing antenna that passively measures MW radiation emitted from the ocean surface. Together with retrievals of sea surface temperature, its measurements support retrieval of surface wind speeds accurate to within 1 m s^{-1} at speeds above 15 m s^{-1} (Uhlhorn and Black 2003). A comparison of these retrieved surface winds to the surface winds of the deterministic forecasts initialized at 18 UTC 27 August is shown in Figure 4.7a for various lead times. These

rather unconventional times were chosen because they correspond to times when the observations within the inner core were available. Additionally, the analysis from which these forecasts were initialized is not shown since SFMR retrievals at that time are only available on the outer fringes of the storm. Figure 4.7a shows that the GTS+IR forecast better captures the intensification of Dorian than the GTS Only experiment. As the GTS+IR forecast is integrated, it develops a classic Rankine vortex-like structure of a developed TC, with the eye wall maxima more closely matching the intensity of the observations than the GTS Only forecast. Although the positions of the eye wall maxima and minimum deviated a bit from those of the observations, the inner core wind structure of the GTS+IR forecast is noticeably more accurate than that of the GTS Only forecast.

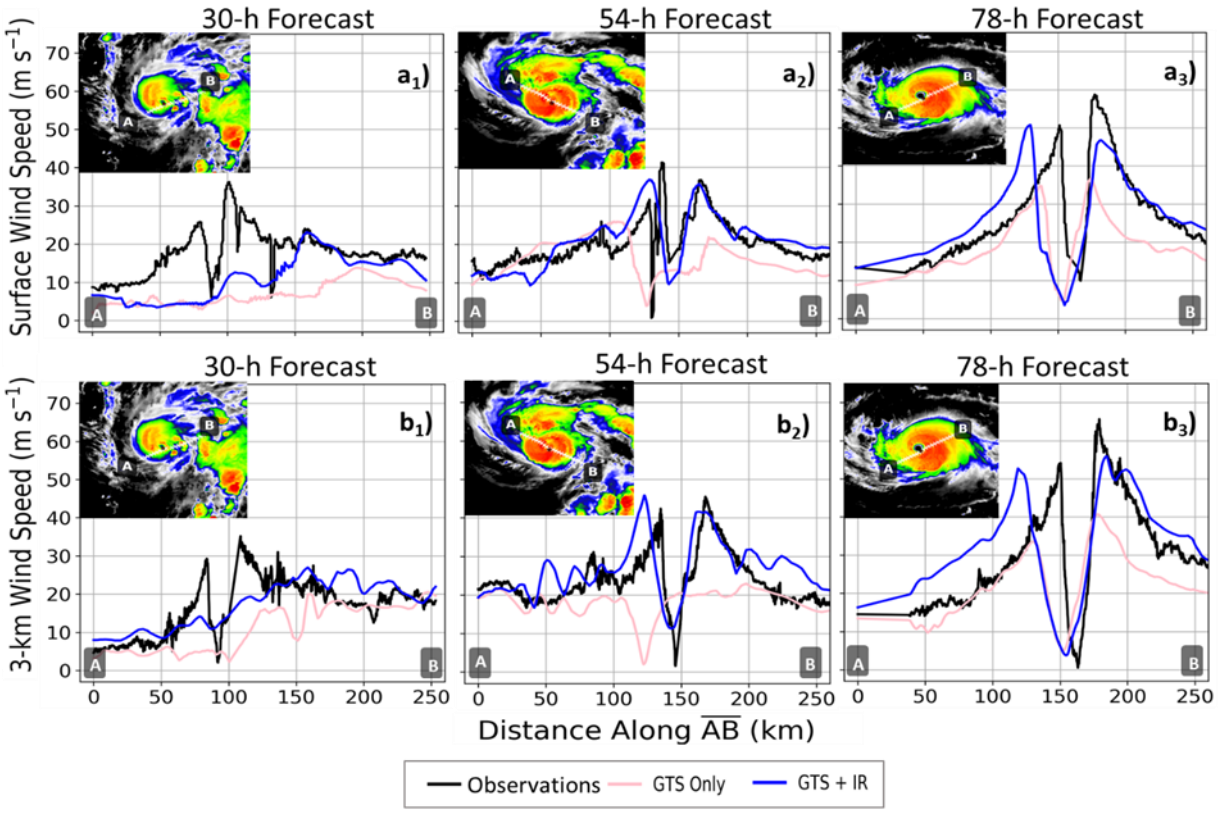

Figure 4.7. Observed and simulated (a_1-a_3) surface and (b_1-b_3) 3-km wind speeds along the line segments within each inset. The (a_1,b_1) 30-h, (a_2,b_2) 54-h, and (a_3,b_3) 78-h deterministic forecasts were initialized from the 18 UTC 27 August EnKF analysis mean of the GTS Only and GTS+IR experiments. Observed surface winds were retrieved by the SFMR instrument aboard NOAA aircraft. Observed 3-km wind speeds were measured by flight-level probes aboard NOAA aircraft.

Not only does the GTS+IR forecast produce a more accurate inner core surface wind structure, but it also better captures the inner core wind structure in the lower troposphere. This can be seen in Figure 4.7b, which compares the simulated 3-km inner core wind speeds to those observed by probes aboard NOAA P-3 aircraft. It is important to stress that neither these observations, nor the SFMR-retrieved observations, were assimilated in any experiment. Although the eye wall maxima of the GTS+IR forecast are often too far apart relative to the observations, it is apparent that the GTS+IR forecast better captures the intensity of the eye wall maxima than the GTS Only forecast.

In summary, relative to an experiment that does not assimilate all-sky IR BTs, hourly assimilation of all-sky IR BTs for 6 hours results in an analysis that has stronger primary and secondary circulations, enhanced convection, and better-defined cloud structures. This translates to a deterministic forecast that better captures the RI and inner core winds of Hurricane Dorian. These results are consistent with the recent literature on other TCs (Zhang et al. 2016; Honda et al. 2018; Minamide and Zhang 2018; F. Zhang et al. 2019).

4.3.2 Combined Impacts of TDR radial velocity and IR BT Assimilation

Now the impacts of simultaneously assimilating TDR radial velocities and all-sky IR BTs are presented. As in the previous subsection, the results of deterministic forecasts are presented and then the physical reasons for differences among them are elaborated on.

Figure 4.8 shows four of the twelve deterministic forecast sets that were initialized during or after the first TDR cycle (22 UTC 27 August). Inspecting the track forecasts (Figures 4.8a$_2$,4.8a$_3$), it is clear that track errors of the operational HWRF and NHC OFCL forecasts, as well as all experiments, diverge from the best track values in the last two days of the five-day forecasts. Aside from that, both the HWRF and OFCL forecasts initialized at 00 UTC and 12 UTC 28 August overestimate the forward translational speed of Dorian, resulting in an erroneously forecasted Florida landfall (Figures 4.8a$_2$,4.8a$_3$). In contrast, forecasts initialized at 00 UTC 28 August from this study's experiments better capture the forward translational speed (Figure 4.8a$_2$), with hints of the northward curve beginning to appear at the end of forecast day five. All in all, both the 00 UTC and 12 UTC 28 August track forecasts initialized from these

experiments better match the best track over the first three days of the forecasts than the operational guidance.

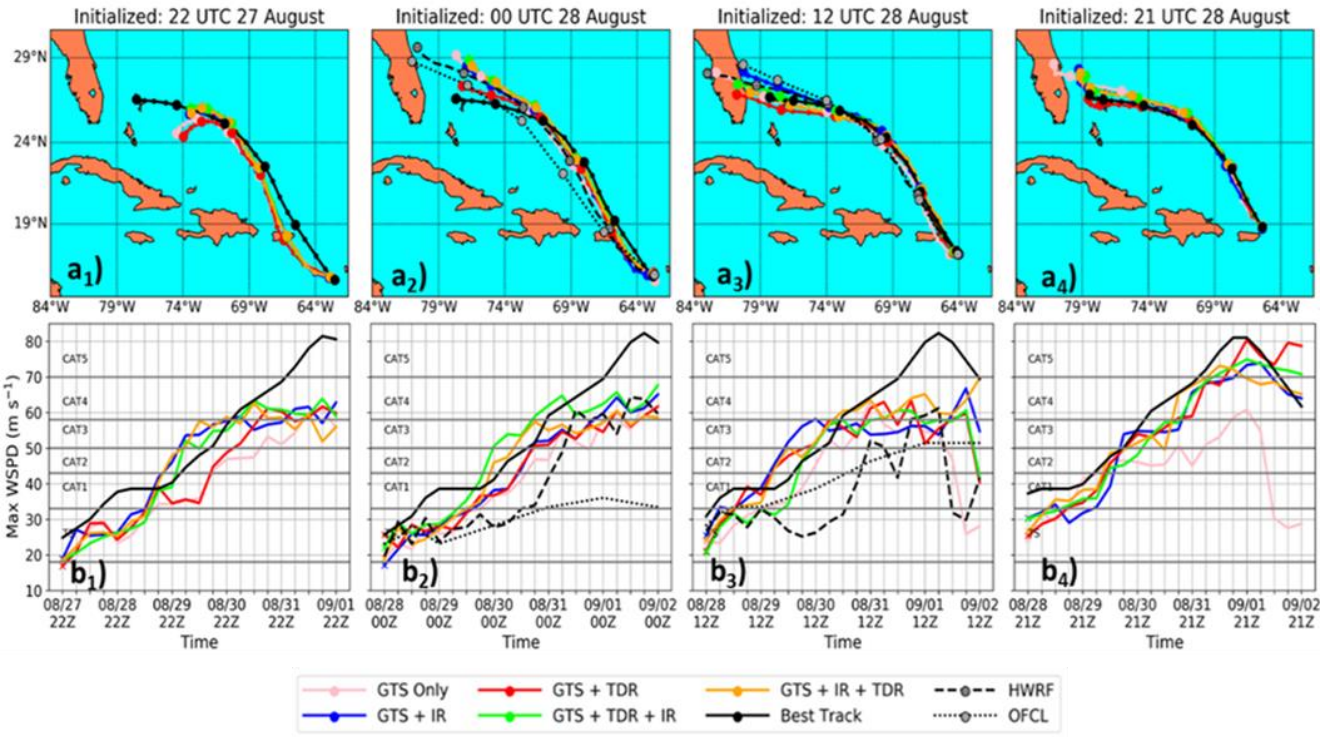

Figure 4.8. As in Figure 4.2, but for deterministic forecasts initialized during and after the first phase of TDR cycling.

When forecasts of the maximum surface wind speed are compared to operational guidance, it can be seen that at 00 UTC (Figure 4.8b$_2$) and 12 UTC (Figure 4.8b$_3$) 28 August OFCL fails to predict the RI of Dorian, whereas HWRF at those times predicts a delayed RI. At these forecast times the experiments in this study better capture the RI of Dorian than operational guidance. Consequently, they are able to predict peak intensities that are closer to the best track values (Figures 4.8b$_2$,4.8b$_3$). As a side note, the forecasts initialized at 21 UTC 28 August (Figure 4.8b$_4$) best captures the best track peak intensity. At this time, all experiments except the GTS Only predict Dorian to reach category 5 intensity.

At this point, attention is turned to the average track and intensity errors of the deterministic forecasts. The forecasts initialized at 12 UTC and 18 UTC 27 August (Figure 4.2) are excluded from this analysis because only two (GTS Only and GTS+IR) of the five

experiments produced forecasts at those times due to TDR observations not yet being available. For the remaining 5-day deterministic forecasts, the mean absolute errors (MAEs) of track and maximum surface wind speed relative to the HURDAT2 best track values were calculated as a function of lead time (Figure 4.9). From a lead time of 24 h and greater, average track errors of HWRF are always higher than the five experiments in this study, whereas average track errors of OFCL are comparable to the GTS Only experiment (Figure 4.9a_2). In terms of intensity, HWRF average errors are comparable to or higher than the GTS Only experiment whereas OFCL has a higher average intensity error than all experiments in this study for lead times over 40 h (Figure 4.9b_2). These results show that the forecasts of track and intensity in this study outperform the operational HWRF and OFCL forecasts at lead times of 2 days or more.

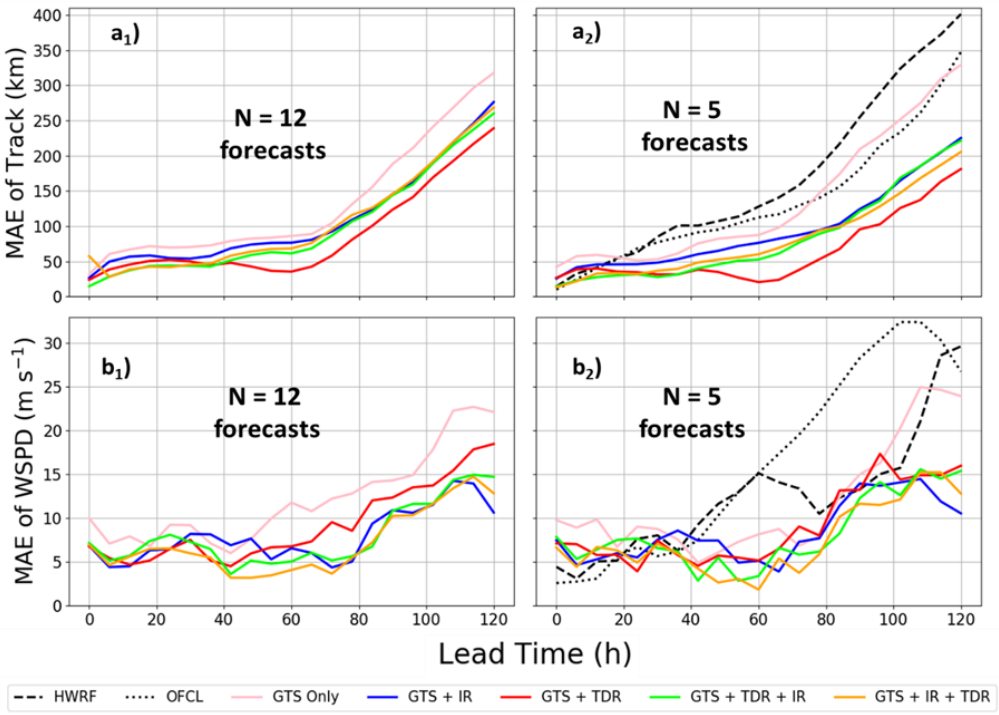

Figure 4.9. MAEs relative to the HURDAT2 best track values of (a_1,a_2) track and (b_1,b_2) maximum surface wind speed from deterministic forecasts as a function of lead time. Forecasts initialized prior to 22 UTC August 27 were excluded from the calculations in order to make a fair comparison among experiments. For column 1 the averages were taken over all twelve forecasts denoted by a black 'x' in Figure 4.1 that were initialized at 22 UTC 27 August or later. For column 2 the averages were taken over the five forecasts denoted by a black 'x' in Figure 4.1 that were initialized when HWRF and OFCL produced forecasts.

When the average track errors of the experiments in this study are compared to one another (Figure 4.9a_1), it is seen that the GTS+TDR experiment outperforms all other experiments from a lead time of 40 h and longer. More specifically, the average MAE of track for the GTS+TDR experiment for lead times greater than 48 h is 25% lower than that of the GTS+IR+TDR experiment. Furthermore, the Student's t-test (Gosset 1908) indicates at greater than 95% confidence that the GTS+TDR experiment produces a lower average track error than any other forecast at lead times of 48 h to 72 h.

Despite the improved track forecasts, the GTS+TDR experiment did not have the lowest average intensity errors at any lead time (Figure 4.9b_1). Average intensity errors for 48 h and longer lead times were consistently lower for experiments that assimilated IR observations than for experiments that did not. At lead times of 48 h to 72 h, the GTS+IR+TDR experiment had the lowest average intensity errors. The improvement of this experiment at those times over the GTS Only and GTS+TDR experiments is statistically significant with confidence values always greater than 92%. When comparing the GTS+IR+TDR experiment to the other experiments that assimilated IR observations, it was found that the average intensity errors at lead times of 48 h to 72 h are 37% lower than the GTS+IR and 27% lower than the GTS+TDR+IR experiment. These improvements in the intensity forecast at 48 h to 72 h lead times are statistically significant at confidence values greater than 90% for many of those hours. In summary, average intensity errors of deterministic forecasts initialized from experiments that assimilated IR observations were lowest for all lead times of 48 h and longer, with the greatest improvements coming from the GTS+IR+TDR experiment for lead times from 48 h to 72 h. These results demonstrate that assimilating TDR observations along with IR observations does not degrade the intensity forecasts but rather has the potential to improve them. The order in which observations are assimilated within a cycle has an impact on the forecast. In this study, both the average track and intensity errors are sensitive to that order.

The impacts of simultaneously assimilating TDR and IR observations on the structure of the analyzed and forecasted wind fields are discussed next. This discussion commences with cross sections of the azimuthally averaged tangential (Figure 4.10) and radial (Figure 4.11) winds for all five experiments at the time of the first TDR cycle. Note that the GTS+TDR

experiment was initialized from the background of the GTS Only experiment whereas the GTS+TDR+IR and GTS+IR+TDR experiments were initialized from the background of the GTS+IR experiment. Additionally, there was a total of 247 conventional GTS observations assimilated within domain three during this cycle - one HPI, six METAR (T, U, V at two locations), and 240 soundings (T, U, V, Q at ten levels at six locations). Comparing Figures 4.10a_1 and 4.10b_1 reveals that the primary circulation in the background of the GTS+IR experiment is substantially stronger than that of the GTS Only experiment. Furthermore, the RMW is smaller in the GTS+IR experiment. These primary circulation and RMW differences are consistent with what was shown for the 18 UTC 27 August cycle (Figure 4.3).

Inspecting the primary and secondary circulations of the GTS+IR experiment at this cycle reveals that the assimilation of conventional GTS and IR observations results in little to no adjustment of the primary circulation (Figure 4.10b_3); however, the secondary circulation is impacted (Figure 4.11b_3). The low-level inflow is increased and the upper-level outflow is decreased within the inner core (Figure 4.11b_3). These substantial adjustments to the secondary circulation are likely because cloud patterns are dynamically correlated with patterns of convergence and divergence.

When both conventional GTS and TDR observations are assimilated at the first TDR cycle, the increments (Figure 4.10c_3) show a strengthening of the primary circulation like that of the GTS Only experiment but this time extending to the mid and upper levels of the storm. This is not surprising, considering that the TDR observations within the inner core of the storm extended to altitudes as high as 10 km. Assimilation of conventional GTS and TDR observations also strengthens the secondary circulation (Figure 4.11c_3). This strengthening of the secondary circulation likely helps to spin up the vortex in the GTS+TDR experiment. These results show that assimilation of TDR radial velocities adjusts both the primary and secondary circulations of the TC.

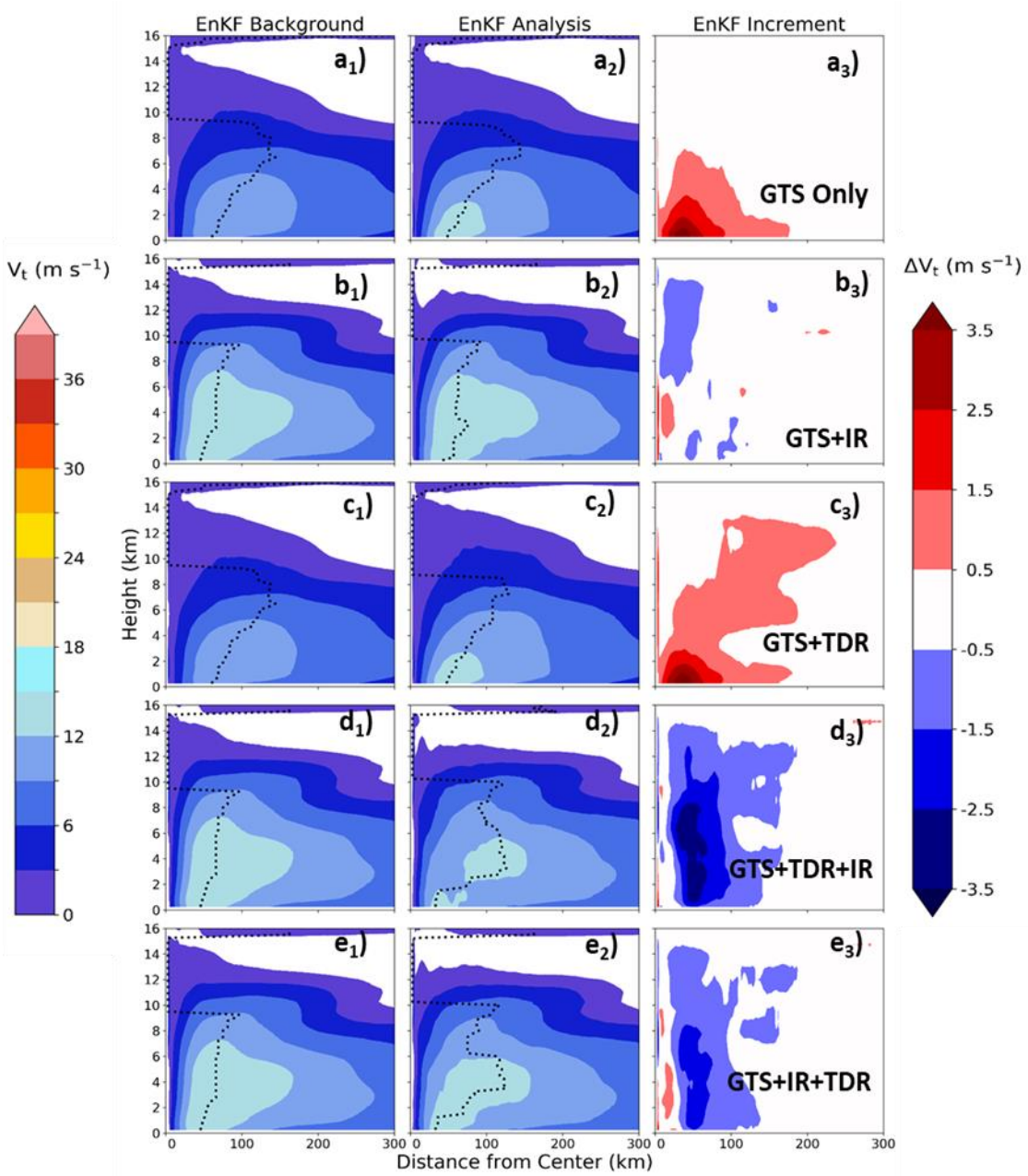

Figure 4.10. Azimuthally averaged tangential velocities for the first TDR cycle (22 UTC 27 August) of the EnKF (a_1-e_1) background mean, (a_2-e_2) analysis mean, and (a_3-e_3) increment of the (a) GTS Only, (b) GTS+IR, (c) GTS+TDR, (d) GTS+TDR+IR, and (e) GTS+IR+TDR experiments. The RMW is denoted by the black dotted line.

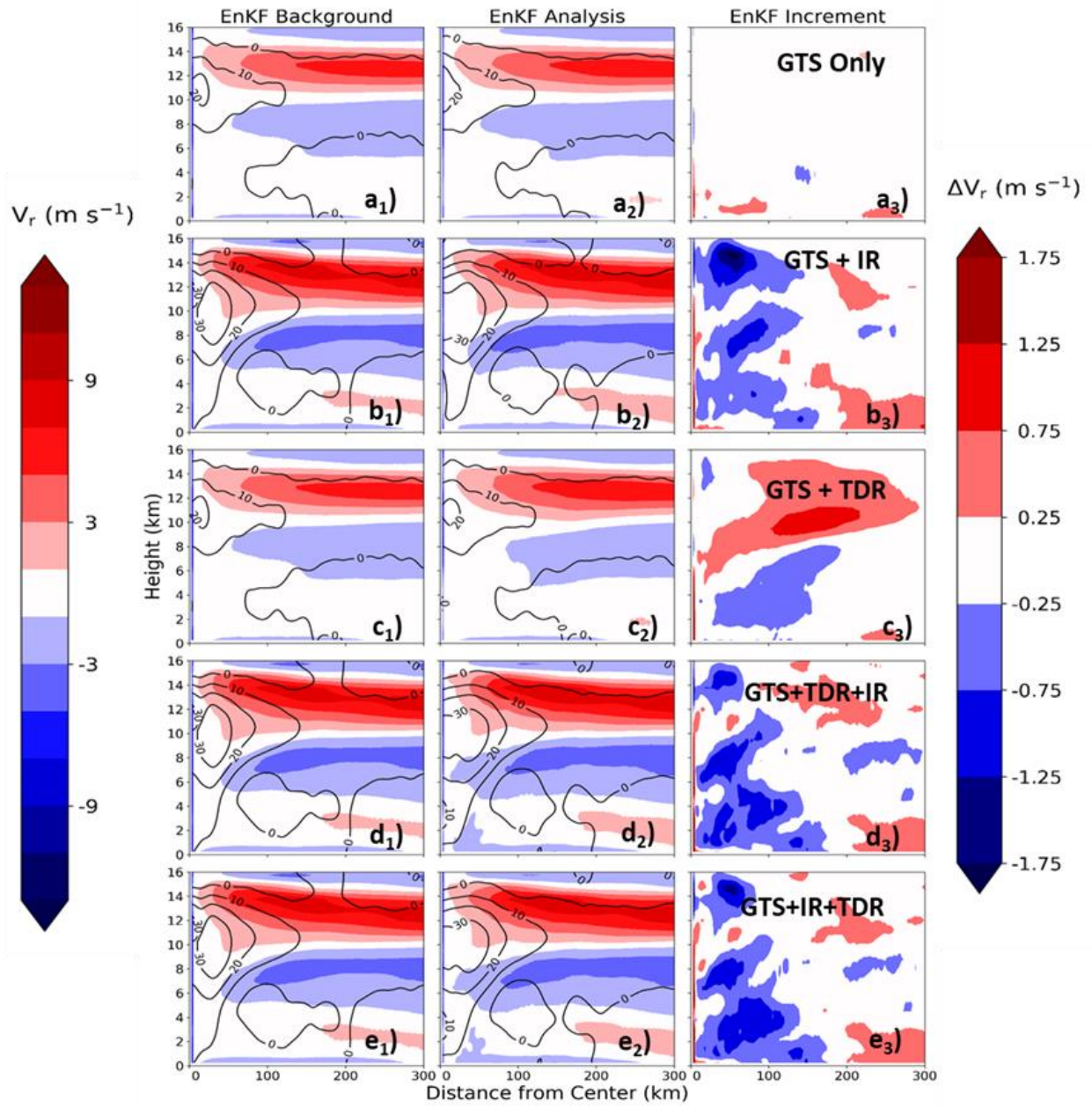

Figure 4.11. As in Figure 4.10, but for azimuthally averaged radial velocities. Black contours show azimuthally averaged vertical velocities in cm s^{-1}. Note that a Gaussian smoother was applied to the vertical velocity with a smoothing length scale of 6 km in the horizontal and 0.5 km in the vertical.

Figures 4.10d_3 and 4.10e_3 show that both the GTS+TDR+IR and GTS+IR+TDR experiments have strong negative increments in the tangential velocity centered around 50-km radius. In the region within 25-km radius, the increments are small or slightly positive in the lower troposphere (Figures 4.10d_3,4.10e_3). This pattern indicates that the addition of TDR observations to the already strong GTS+IR background weakens the vortex in the middle and upper troposphere around 50-km radius. At the same time, TDR observations also tighten the vortex in the lower troposphere, which can be seen in the RMW migrating to approximately 25 km in the lowest 2 km (Figures 4.10d_2,4.10e_2). Note that the increments in the GTS+TDR+IR experiment are not exactly the same as for the GTS+IR+TDR experiment. This shows that the order of assimilation with a serial EnKF makes a difference in the primary circulation. While both experiments act to tighten the lower TC vortex, they do so in different ways. For instance, the GTS+TDR+IR experiment produces much stronger negative increments centered on 50-km radius and small positive increments within 25-km radius, whereas the GTS+IR+TDR produces weaker negative increments centered on 50-km radius but produces slightly stronger positive increments within 25-km radius. These differences in the increments explain the differences in the analyzed primary circulations of the GTS+TDR+IR and GTS+IR+TDR experiments (Figures 4.10d_2,4.10e_2). In conclusion, simultaneously assimilating TDR and IR observations results in tightening of the primary circulation in the lower troposphere and weakening of the primary circulation in the middle and upper troposphere relative to the GTS+IR experiment.

Next, the impacts of simultaneous assimilation of TDR and IR observations on the secondary circulation of Dorian (Figures 4.11d,4.11e) are investigated. Earlier, it was shown that the assimilation of IR BTs impacts the secondary circulation in the inner core in such a way as to increase low-level inflow and decrease upper-level outflow (Figure 4.11b_3). That pattern is also seen in the GTS+TDR+IR and GTS+IR+TDR experiments; however, the pattern is weakened at upper levels and enhanced at lower levels relative to the GTS+IR experiment. This shows that assimilation of TDR radial velocities simultaneously with IR BTs impacts the secondary circulation and does so in a manner that counteracts the impacts of the IR BTs in the upper troposphere. The impacts of the order of assimilation on the secondary circulation are relatively small compared to the impacts on the primary circulation.

To emphasize the previous points, Figure 4.12 plots the differences between the EnKF analysis means at 22 UTC 27 August of the azimuthally averaged tangential and radial velocities for the experiments that had the same background at the start of the first TDR cycle. Figure $4.12a_1$ shows that the primary circulation of the GTS+TDR analysis is stronger above 4 km and slightly weaker below 4 km than the GTS Only analysis, whereas Figure $4.12a_2$ shows that the secondary circulation of the GTS+TDR analysis is clearly stronger than the GTS Only analysis at all levels.

Comparing the differences among the primary circulations of the experiments that assimilated IR (Figures $4.12b_1$ – $4.12d_1$), it can be found once again that simultaneously assimilating TDR and IR observations reduces the overall intensity of the vortex relative to the GTS+IR analysis at 50-km radius. This effect is more dramatic when TDR is assimilated before IR (compare Figure $4.12c_1$ to Figure $4.12b_1$). The net impact is a primary circulation that is stronger at radii centered around 50 km for the GTS+IR+TDR analysis (Figure $4.12d_1$). When comparing the differences among the secondary circulations of the experiments that assimilated IR (Figures $4.12b_2$ – $4.12d_2$), it is apparent that both the GTS+TDR+IR and GTS+IR+TDR analyses at this time have a stronger secondary circulation than the GTS+IR analysis (Figures $4.12b_2$,$4.12c_2$). As a result of assimilating TDR observations, the upper-level outflow strengthened and lifted vertically relative to the GTS+IR analysis whereas the lower-level inflow strengthened within the inner core. This effect is more pronounced when assimilating TDR before IR (Figure $4.12d_2$). Based on Figure $4.12d_2$, it can be concluded that the GTS+TDR+IR analysis has a stronger upper-level outflow than in the GTS+IR+TDR analysis. Additionally, the low-level inflow within 50-km radius of the TC center is stronger in the GTS+TDR+IR analysis, yet outside of 50-km radius it is stronger in the GTS+IR+TDR analysis. To summarize, simultaneously assimilating TDR and IR observations weakens the TC vortex in the middle-to-upper troposphere, tightens the TC vortex in the lower troposphere, and strengthens the secondary circulation relative to the GTS+IR analysis, with the net impact being more pronounced if TDR is assimilated before IR.

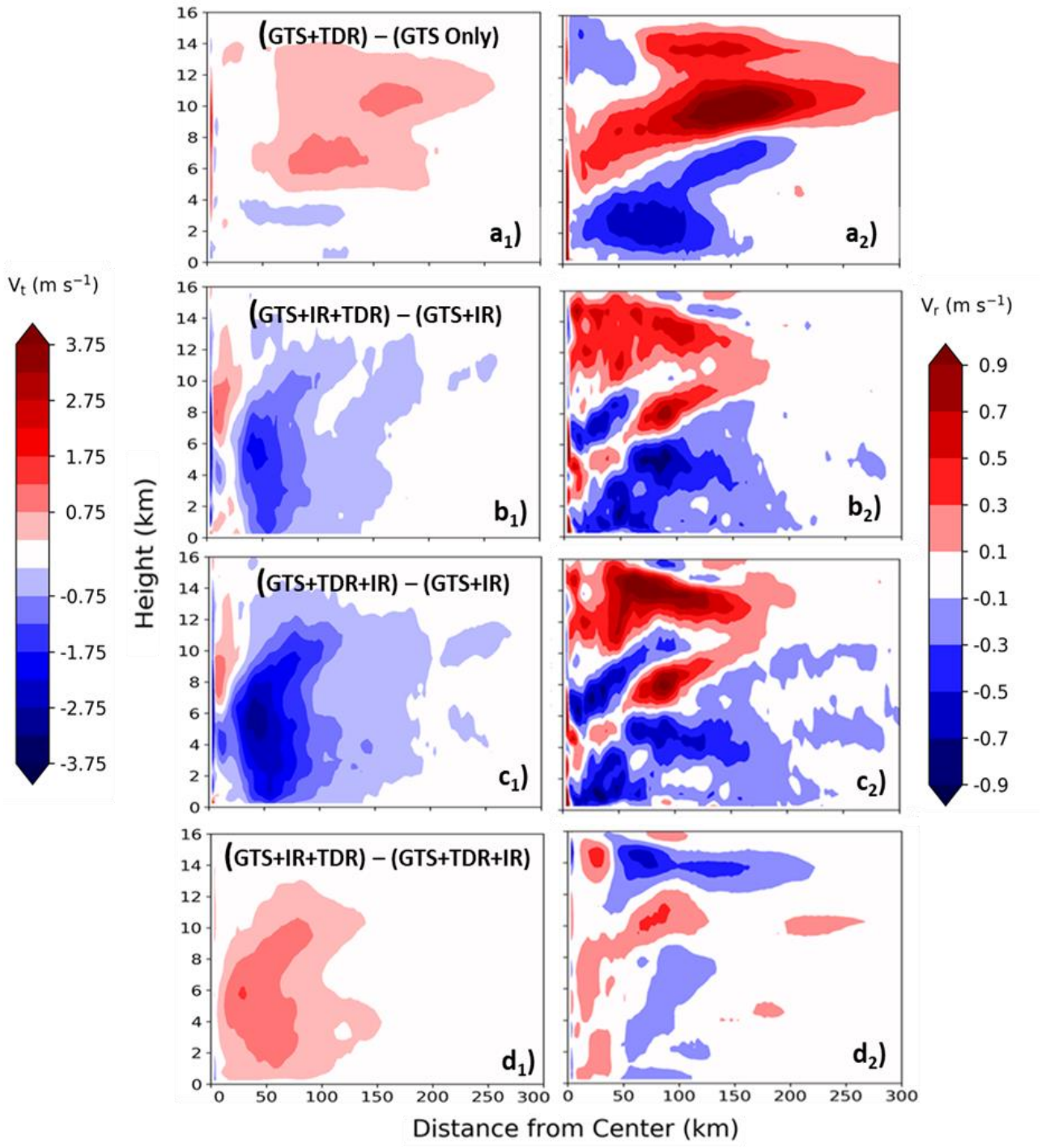

Figure 4.12. Experiment differences at 22 UTC 27 August between the EnKF analysis mean (a_1-d_1) azimuthally averaged tangential velocities and (a_2-d_2) azimuthally averaged radial velocities for those experiments that had the same background mean at the start of the first TDR cycle.

It is important to note that Dorian was still a sheared tropical storm at the time of this first TDR cycle. Consequently, azimuthal averages of the secondary circulation might not tell the full story of the impacts of TDR assimilation when the average is taken over the entire vortex. Therefore, differences in the secondary circulations using azimuthal averages for each shear-relative quadrant (Figure 4.13) were investigated. Inspection of these shear-relative differences (note the color bar is different from Figure 4.12) reveals that the left of shear quadrants contain the dominant contributions to the vortex-wide azimuthal averages in Figure 4.12.

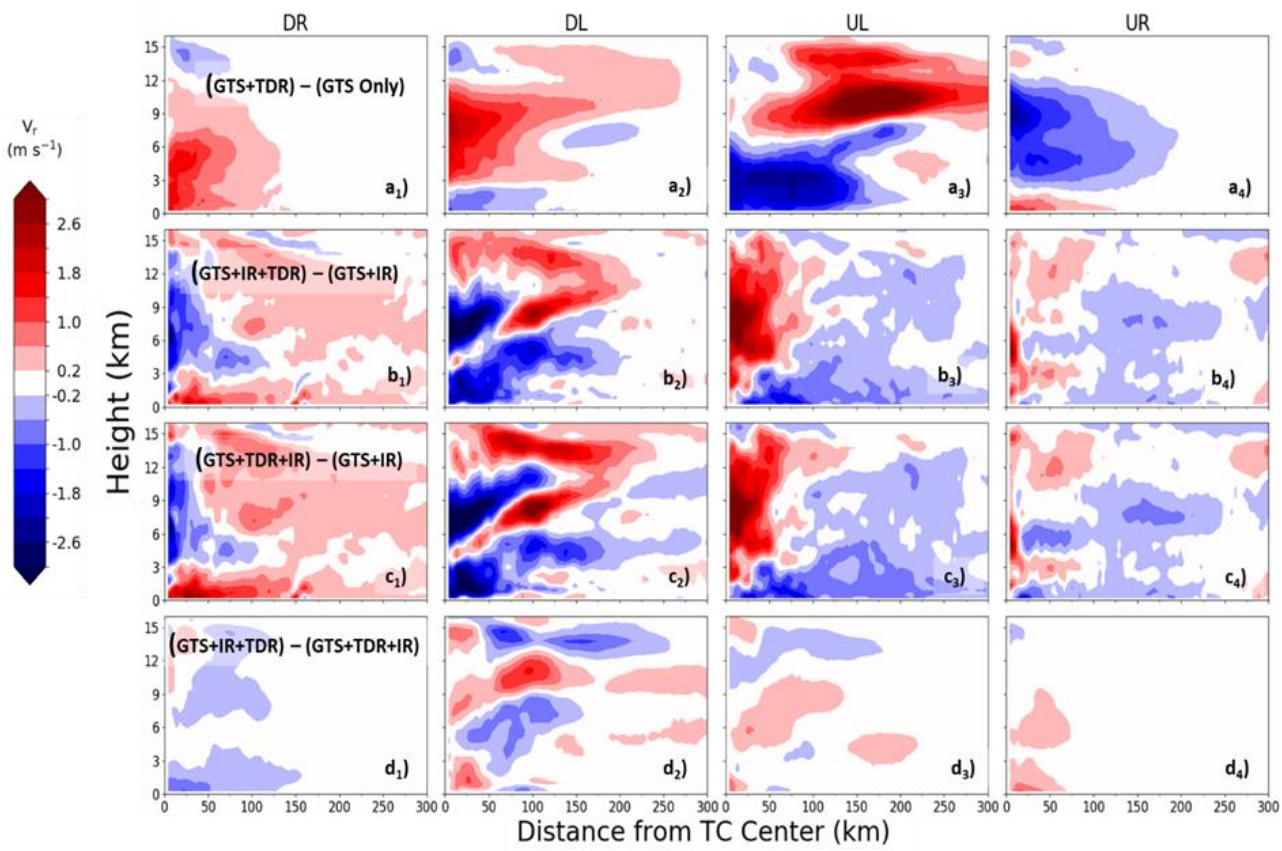

Figure 4.13. Experiment differences at 22 UTC 27 August between the EnKF analysis mean azimuthally averaged radial velocities for those experiments that had the same background mean at the start of the first TDR cycle for the (a_1,b_1,c_1,d_1) downshear right (DR), (a_2,b_2,c_2,d_2) downshear left (DL), (a_3,b_3,c_3,d_3) upshear left (UL), and (a_4,b_4,c_4,d_4) upshear right (UR) quadrants.

The cumulative effects of simultaneously assimilating TDR and IR observations on the low-level vortex are illustrated as Hovmöller diagrams in Figure 4.14. Inspection of this figure reveals that the experiments assimilating IR observations produced high (e.g., 16 m s^{-1}) azimuthally averaged 10-m wind speeds sooner than experiments that did not. Although the TDR experiments were slower to develop high 10-m wind speeds, they ended up producing wind speeds that exceeded the GTS+IR experiment during the second TDR phase of cycling (21 UTC August 28 – 00 UTC August 29). Further inspection of Figure 4.14 reveals that the region of 10-m wind speeds exceeding 16 m s^{-1} extended noticeably farther from the TC center in the GTS+IR experiment than in the experiments that assimilated both IR and TDR observations. Consequently, these Hovmöller diagrams are consistent with the finding that simultaneously assimilating TDR and IR observations tightened the low-level vortex relative to the GTS+IR experiment.

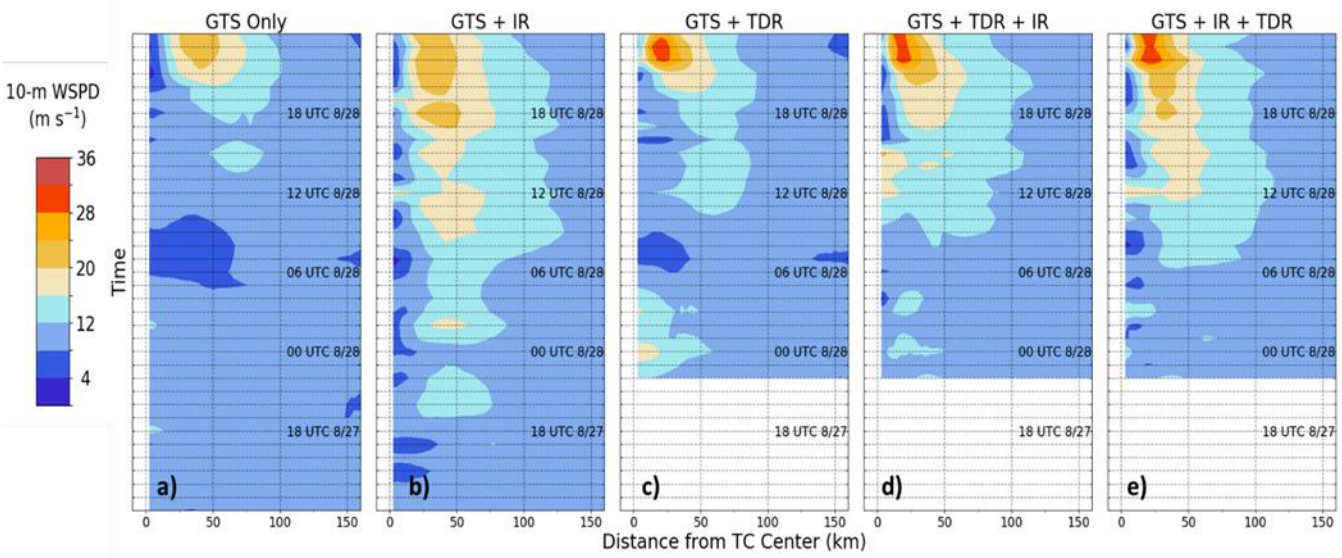

Figure 4.14. Temporal evolution of 10-m wind speeds in the EnKF analysis mean for the (a) GTS Only, (b) GTS+IR, (c) GTS+TDR, (d) GTS+TDR+IR, and (e) GTS+IR+TDR experiments.

As before, the analyzed and forecasted inner core wind speeds are compared to the SFMR-retrieved surface wind speeds (Figure 4.15) and 3-km observed wind speeds (Figure 4.16). Inspection of Figure 4.15 reveals that assimilating TDR radial velocities improves the analyzed and forecasted inner core surface wind structure. At most times, the overly broad vortex of the GTS+IR is narrowed when TDR observations are assimilated. Furthermore, the two experiments that assimilated both IR and TDR observations better capture the intensity and location of the eye wall maxima. These conclusions apply to the 3-km wind speed as well (Figure 4.16). Ultimately, assimilating TDR radial velocities improves the analyzed and forecasted inner core wind speeds, with the greatest benefits coming from experiments that assimilate it simultaneously with IR observations.

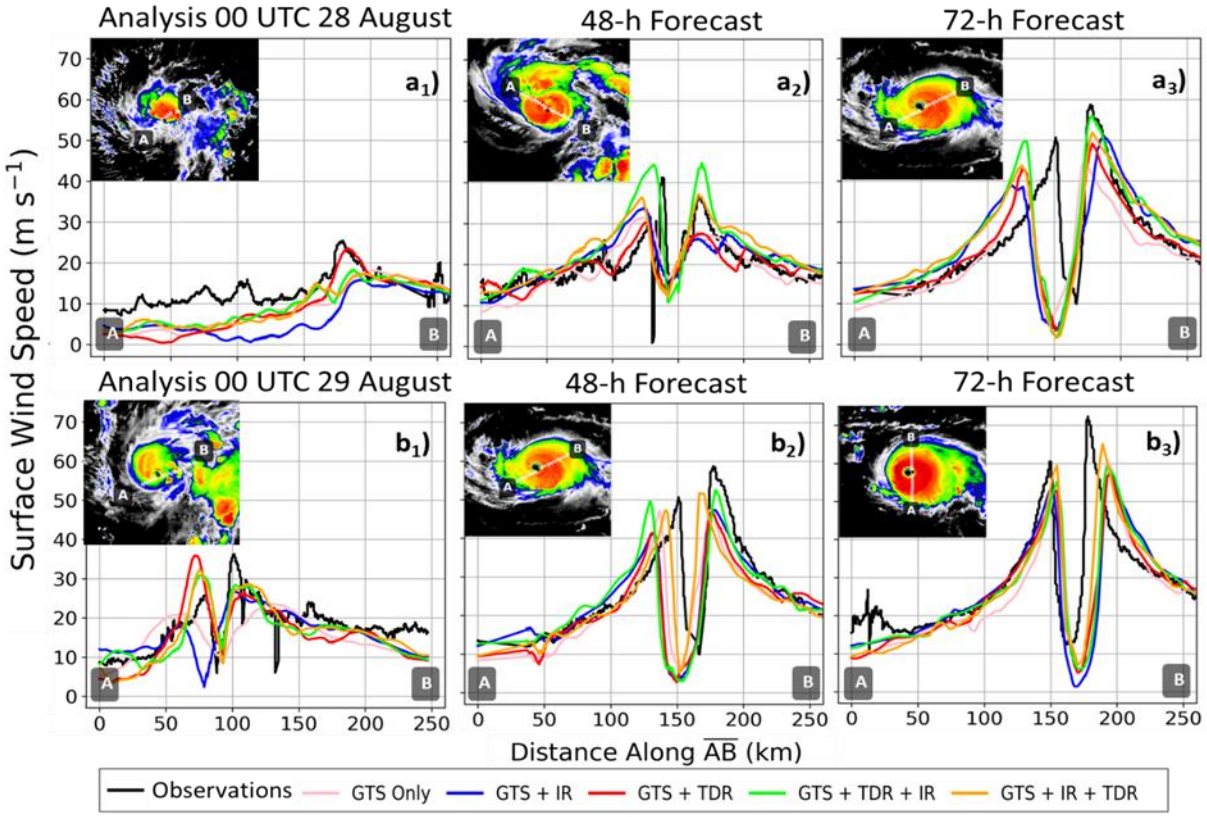

Figure 4.15. Observed surface wind speeds together with simulated surface wind speeds along line segment AB within each inset for the EnKF analysis mean at (a_1) 00 UTC 28 August and (b_1) 00 UTC 29 August, as well as the (a_2, b_2) 48-h and (a_3,b_3) 72-h forecasts initialized from them. Observed surface wind speeds were retrieved from the SFMR instrument aboard NOAA aircraft.

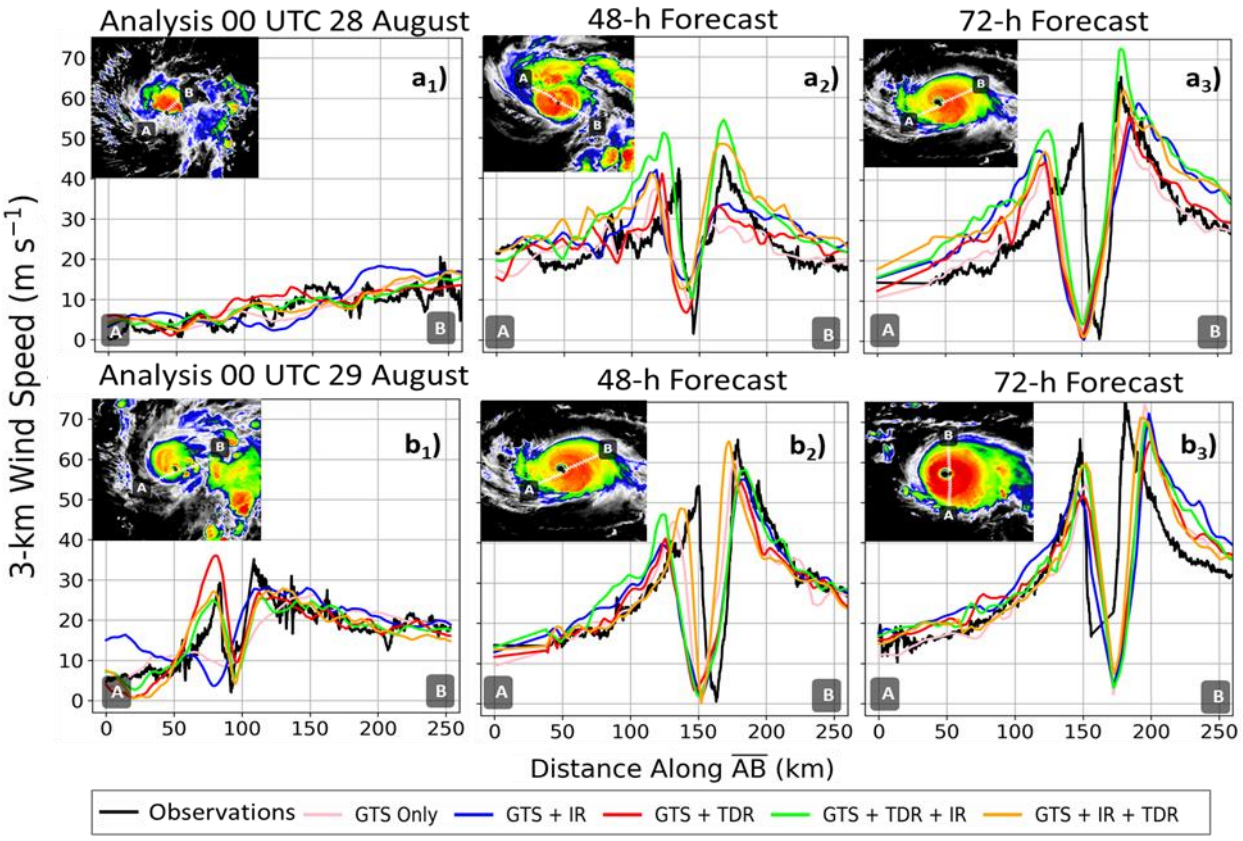

Figure 4.16. As in Figure 4.15, but for 3-km wind speeds. Observed 3-km wind speeds were measured by flight-level probes aboard NOAA aircraft.

4.4 Discussion and Conclusions

In this study, the value of simultaneously assimilating TDR radial velocities and GOES-16 all-sky IR BTs on both the analyses and forecasts of Hurricane Dorian was shown. Results of deterministic forecasts show that forecasts initialized from analyses that assimilated TDR radial velocities after conventional GTS observations had 25% lower average track errors at a lead time of 48 h and greater compared to any other experiment. In terms of intensity, forecasts that assimilated all-sky IR BTs had average intensity errors lower than forecasts that did not assimilate all-sky IR BTs at lead times of 48 h and greater. The improvements brought to forecasts when assimilating IR observations were shown to be a result of better analyzed cloud and moisture fields, as well as more intense initial primary and secondary circulations. Simultaneously assimilating TDR radial velocities and all-sky IR BTs further reduced the average intensity errors relative to the GTS+IR experiment by 37% at lead times of 48 h to 72 h. These improvements were shown to be a result of a more realistic inner core wind structure when TDR and IR observations are assimilated together. Ultimately, simultaneously assimilating TDR radial velocities and all-sky IR BTs has the potential to achieve more accurate track and intensity forecasts than only assimilating all-sky IR BTs.

This study also showed that the order in which these observations are assimilated makes a difference in the results. At lead times of 48 h to 72 h, the intensity errors of forecasts that assimilated all-sky IR BTs before TDR radial velocities are, on average, 27% lower than those of forecasts that assimilated all-sky IR BTs after TDR radial velocities. This dependence of the analysis on the order of assimilation when using a serial filter has been demonstrated in other studies as well (Nerger 2015; Kotsuki et al. 2017). The assimilation order can influence the results of sequential methods like EnSRF as a result of localization of the increments coming from each observation (i.e., Kalman gain localization, or Kloc). Furthermore, Kotsuki et al. (2017) demonstrated that the analysis can be significantly improved in the EnSRF by changing the assimilation order. Determining the optimal order of assimilation when simultaneously assimilating TDR radial velocities and all-sky IR BTs with a serial EnKF is something that deserves more attention in the future, especially considering that serial EnKF methods that employ Kloc are used in operational practice and are common in ensemble DA research. For

instance, Environment Canada has been running a Kloc EnKF system (Houtekamer and Mitchell 2001) globally since 2005 (Houtekamer and Mitchell 2005; Jacques et al. 2017). Also, the NCAR experimental real-time convection-allowing ensemble prediction system (Schwartz et al. 2015) is based on a Kloc EnKF method (Anderson 2001). There is also a plethora of ensemble DA research that employs Kloc EnKF (e.g., Romine et al. 2013; Thompson et al. 2015; Zhang et al. 2018; Y. Zhang et al. 2019). As such, the findings of this study have implications for the ensemble DA community.

The improvements brought to deterministic forecasts by all-sky IR BT assimilation in this study, as well as other studies, is encouraging. Additionally, assimilating TDR observations, even with their limited spatial (~ 1/6 that of the IR observations) and temporal (only 9 out of the 37 cycles when IR was assimilated) coverage, brought added improvements to those obtained from all-sky IR BT assimilation. These results suggest that more frequent TDR flights through burgeoning storms will substantially improve hurricane forecasts, even with the availability of dense and frequent IR observations.

Given the expense of TDR flights, it is necessary to test the setup of this experiment on other storms to confirm that the case of Hurricane Dorian is not a statistical anomaly. As such a test, additional experiments were conducted on Hurricane Laura (2020), the only other storm since GOES-16 became operational that was poorly forecasted and for which there were TDR measurements prior to RI (as of the time of this study). In the Hurricane Laura experiments, the same experimental design was used as for Hurricane Dorian, but without the GTS Only and GTS+TDR experiments. The ensemble was initiated at 18 UTC 22 August and spun-up until 06 UTC 23 August. Then, the ensemble of the GTS+IR experiment was initiated from the ensemble at 06 UTC 23 August and cycled hourly until 14 UTC 23 August. Also, the GTS+IR+TDR and GTS+TDR+IR experiments were initialized from the background of the GTS+IR experiment at 10 UTC 23 August and cycled hourly until 14 UTC 23 August. Finally, three five-day deterministic forecasts were initialized from the EnKF analysis means at 12 UTC, 13 UTC, and 14 UTC 23 August.

Although the track forecasts had substantial errors, the intensity forecasts of the GTS+TDR+IR and GTS+IR+TDR experiments more accurately predicted the RI of Laura than the GTS+IR experiment. Furthermore, the GTS+IR+TDR had an MAE of maximum surface wind speed that was slightly smaller than that of the GTS+TDR+IR experiment. These results are consistent with the results of the Hurricane Dorian experiments and provide support for additional TDR measurement campaigns focused on future storms. Future studies should also investigate more deeply the interplay between the adjustment of the TC vortex by the assimilation of all-sky IR BTs and TDR radial velocities in order to reap the maximum benefits from each.

Data Availability Statement

The EnKF analyses and WRF forecasts presented in this study can be freely downloaded from the Penn State Data Commons (https://doi.org/10.26208/37q8-3r61). All assimilated GTS observations were obtained from datasets 351.0 and 461.0 of the NCAR Research Data Archive (https://rda.ucar.edu). TDR data, as well as SFRM retrievals and 3-km wind speed observations, were obtained from NOAA HRD (www.aoml.noaa.gov/hrd/Storm_pages/dorian2019/). All assimilated GOES-16 ABI Channel 8 BTs were ordered from the NOAA Comprehensive Large Array-Data Stewardship System (https://www.avl.class.noaa.gov/).

Chapter 5

Concluding Remarks

This dissertation demonstrated the improvements that can be brought to forecasts of TCG and TC RI, the two least predictable stages in the lifecycle of a TC, by assimilating all-sky IR BTs from geostationary satellites with an ensemble-based DA system (the PSU-EnKF). The common theme throughout the studies comprising this dissertation is the ability of the all-sky IR BT assimilation to produce a more realistic representation of convection in analyses and the forecasts initialized from them. With a more realistic convective evolution, the forecasts are better able to capture both the formation and intensification of TCs.

In chapter 2, it was shown that the timing of TCG in forecasts of Hurricane Irma (2017) can be improved by assimilating all-sky IR BTs observed by the upper-tropospheric water vapor channel of the SEVIRI instrument onboard the Meteosat-10 satellite. In that study, deterministic forecasts initialized two days before TCG in an experiment that withheld the all-sky IR BTs featured the premature TCG of Irma by up to 24 hours. It was revealed that those forecasts led to premature TCG due to a gross overestimation of the intensity and spatial coverage of deep convection within the region Irma formed from. The excessive deep convection led to the earlier spin-up of the vortex, and hence TCG, due to an enhanced inward advection of relative vorticity and subsequent stretching of that vorticity. Assimilating the all-sky IR BTs led to a drying of both the region Irma formed from and the environment. Consequently, much of the spurious convection was removed in the analyses. Upon integration, the convection followed a much more realistic evolution, which translated to the later, more realistic TCG timing in forecasts.

In chapter 3, it was shown that a substantial portion of the uncertainty in TCG timing can be attributed to uncertainty in the initial moisture content within the region Hurricane Irma (2017) formed from. Motivated by the results of chapter 2, this study presented the results of an ensemble forecast initialized from an analysis, valid two days before Irma formed, in which both all-sky IR and MW BTs had been assimilated. That baseline ensemble featured a wide range of intensity uncertainty, with a range of minimum SLP predictions of 10-hPa to 20-hPa at TCG

time, and up to 60-hPa by the end of the five-day forecast period. By initializing another ensemble forecast that retained only the moisture perturbations of the baseline ensemble within the incipient disturbance, it was shown that at least half of the intensity uncertainty at all times of the forecast can be attributed to the initial moisture uncertainty within the region Irma formed from. Additional sets of ensemble forecasts were initialized that not only retained the initial moisture perturbations within the incipient disturbance, but also shrunk them. These additional forecasts demonstrated that the intensity uncertainty increases monotonically with initial moisture uncertainty due to an earlier development of MCS dislocation errors when the initial moisture uncertainty is higher. These convective differences then grew upscale, projecting onto the vortex much quicker. Consequently, the uncertainty in TCG timing increased as initial moisture uncertainty increased due to uncertainty in the timing of the spin-up of the low-level vortex.

In chapter 4, it was shown that RI forecasts of Hurricane Dorian (2019) can be improved by assimilating the upper-tropospheric water vapor channel BTs observed by the GOES-16 ABI instrument. In that study, forecasts initialized near the onset of RI time had average intensity errors that were lower at lead times of 48 hours and greater when the all-sky IR BTs had been assimilated. These RI forecast improvements were shown to be a result of better analyzed cloud fields, as well as more intense initial primary and secondary circulations. By simultaneously assimilating the all-sky IR BTs with TDR radial velocities observed by the NOAA P-3 aircraft, the average intensity errors at lead times of 48 to 72 hours were further reduced by 37% due to a more realistic inner-core wind structure at initialization time and after integration. By comparing the forecasted wind field to observations that were not assimilated, it was revealed that the assimilation of all-sky IR BTs produced a vortex that was much broader than what was observed. The simultaneous assimilation of TDR radial velocities with the all-sky IR BTs refined the vortex structure such that it was more compact. This translated to improved RI forecasts. Additionally, this study showed that average track errors were 25% lower when assimilating the TDR radial velocities. Ultimately, this study demonstrated the value of simultaneously assimilating all-sky IR BTs and TDR radial velocities on the forecasts of TC track, structure, and RI.

There are several important implications of the results presented within this dissertation. First and foremost, the assimilation of all-sky IR BTs from geostationary satellites is shown to improve TC forecasts from formation through maturity. This dissertation provides further support for the ability of all-sky IR BT assimilation to improve TC RI forecasts and contains a study which is the first of its kind to show the potential improvements it can bring to TCG forecasts. These results should give further motivation for operational centers to upgrade their DA systems to include the capability of all-sky BT assimilation. A second implication of this dissertation is that more flights (either manned or unmanned) into developing TCs should be conducted to collect radial velocity observations. Not only does a study in this dissertation further support the gains that can be brought to RI forecasts by assimilating the radial velocity observations, but it also is the first of its kind to show that TDR radial velocity assimilation can complement all-sky IR BT assimilation. Finally, two of the three studies in this dissertation suggest that TCG forecasts are very sensitive to the initial moisture content within the disturbance the TC forms from. In the absence of in-situ moisture observations over the open ocean, all-sky IR BTs serve as a surrogate, since they can constrain the initial moisture content through the strong ensemble correlations existing between them and the moisture. With the increasing prevalence of unmanned aircraft (e.g., Christophersen et al. 2017; Cione et al. 2020; Aksoy et al. 2022; Zawislak et al. 2022; Sellwood et al. 2023), the targeted collection of moisture observations within the incipient disturbance for the purposes of assimilation into forecasts should be strongly considered if possible. Ultimately, this dissertation provides justification for the collection of more observations of the initial wind and moisture field for the purposes of assimilation alongside all-sky IR BTs to further improve TC RI and TCG forecasts.

The studies comprising this dissertation have a few limitations. Perhaps the most obvious drawback is the reliance on only two case studies. For the TCG studies, attempts were made to simulate a few Atlantic storms that formed from an AEW (i.e., Helene (2018), Isaac (2018), and Lorenzo (2019)); however, all three failed to achieve TCG in the control simulations. Consequently, no conclusions could be drawn from these cases. Additionally, the impact of assimilating all-sky IR BTs on the TCG of Hurricane Florence (2018) was also tested. For Florence, both the control and GTS+IR simulations captured TCG. In this situation, assimilation of the IR BTs appeared, although subtly, to improve TGC timing; however, the slow

intensification that ensued after the observed TCG time made assessing the improvements challenging. For this reason, Florence was abandoned in favor of Irma. These trials show that simulating TCG is challenging indeed. Another limitation of the studies herein is the coarse resolution of the simulations (9 km for the TCG studies and 3 km for the RI study). A more realistic representation of the convective evolution for both studies would be attained by increasing the resolution. At a higher resolution, a more detailed analysis of the fundamental processes of the convection and its interaction with the vortex would be possible. A third limitation of this dissertation is the reliance on a statistically-based update to the initial conditions. For example, the DA system used a form of linear regression. This linear update is not ideal when simulating nonlinear phenomena such as convection. Furthermore, the reliance on a statistically-based update to initial conditions makes the analysis somewhat susceptible to a certain degree of physical imbalance (Houtekamer and Mitchell 2005; Poterjoy and Zhang 2014b). This imbalance can be further degraded by performing localization when assimilating observations (Greybush et al. 2011). Finally, all conclusions within this dissertation were reached using a single forecast and a single DA system. Nevertheless, the studies herein show promise that both TCG and RI forecasts are improvable by assimilating all-sky IR BTs with an ensemble-based DA system.

Given the limitations mentioned, several ideas for future work naturally come to mind. First and foremost, the improvements shown here for the TCG of Irma and the RI of Dorian should be checked for other storms. Since the author was not yet aware of the “marsupial pouch” paradigm during his analysis of the TCG of Hurricane Florence (2018), a pouch-relative framework should be employed to assess the impact of the assimilation of all-sky IR BTs on its TCG. Even though higher resolution simulations would be costly, future studies should make use of higher resolution nested grids that follow the pouch or vortex center. This would allow a closer look at the details of the convection. As noted in chapter 3, there is a diurnal cycle of convection leading up to TCG. A future study should investigate the impact of the diurnal cycle on the predictability of TCG. Also regarding TCG, what is the relative impact of initial condition uncertainty in the wind fields on the predictability of TCG? Finally, future studies should go beyond the assimilation of all-sky BTs in attempting to improve TCG and RI forecasts through the modulation of initial moisture. These observations include, but are not limited to, unmanned

aircraft, both airborne and spaceborne radio occultation, and microwave humidity and temperature sensor observations. Both observation types can obtain detailed thermodynamic profiles. With ever-growing computational power and a growing list of novel observation types, the future of DA and its ability to improve TC forecasting is looking bright!

Bibliography

Aberson, S. D., A. Aksoy, K. J. Sellwood, T. Vukicevic, and X. Zhang, 2015: Assimilation of High-Resolution Tropical Cyclone Observations with an Ensemble Kalman Filter Using HEDAS: Evaluation of 2008–11 HWRF Forecasts. *Mon. Weather Rev.*, **143**, 511–523, https://doi.org/10.1175/MWR-D-14-00138.1.

Aksoy, A., J. J. Cione, B. A. Dahl, and P. D. Reasor, 2022: Tropical Cyclone Data Assimilation with Coyote Uncrewed Aircraft System Observations, Very Frequent Cycling, and a New Online Quality Control Technique. *Mon. Weather Rev.*, **150**, 797–820, https://doi.org/https://doi.org/10.1175/MWR-D-21-0124.1.

Anderson, J. L., 2001: An Ensemble Adjustment Kalman Filter for Data Assimilation. *Mon. Weather Rev.*, **129**, 2884–2903, https://doi.org/10.1175/1520-0493(2001)129<2884:AEAKFF>2.0.CO;2.

——, 2009: Spatially and temporally varying adaptive covariance inflation for ensemble filters. *Tellus A Dyn. Meteorol. Oceanogr.*, **61**, 72–83, https://doi.org/10.1111/j.1600-0870.2007.00361.x.

Anderson, J. L., and N. Collins, 2007: Scalable Implementations of Ensemble Filter Algorithms for Data Assimilation. *J. Atmos. Ocean. Technol.*, **24**, 1452–1463, https://doi.org/10.1175/JTECH2049.1.

Andreas, E. L., L. Mahrt, and D. Vickers, 2015: An Improved Bulk Air–Sea Surface Flux Algorithm, Including Spray-Mediated Transfer. *Q. J. R. Meteorol. Soc.*, **141**, 642–654, https://doi.org/10.1002/qj.2424.

Asaadi, A., G. Brunet, and M. K. Yau, 2016: On the Dynamics of the Formation of the Kelvin Cat's-Eye in Tropical Cyclogenesis. Part II: Numerical Simulation. *J. Atmos. Sci.*, **73**, 2339–2359, https://doi.org/10.1175/JAS-D-15-0237.1.

——, ——, and ——, 2017: The Importance of Critical Layer in Differentiating Developing from Nondeveloping Easterly Waves. *J. Atmos. Sci.*, **74**, 409–417, https://doi.org/10.1175/JAS-D-16-0085.1.

Avila, L. A., 2019: Hurricane Dorian Advisory Number 33. *Natl. Hurric. Cent.*, nhc.noaa.gov.

——, S. R. Stewart, R. Berg, and A. B. Hagen, 2020: *National Hurricane Center Tropical Cyclone Report: Hurricane Dorian (AL052019).* https://www.nhc.noaa.gov/data/tcr/AL052019_Dorian.pdf.

Bao, J.-W., 2016: Physical Processes in Tropical Cyclone Models. *Advanced Numerical*

Modeling and Data Assimilation Techniques for Tropical Cyclone Prediction, U.C. Mohanty and S.G. Gopalakrishnan, Eds., Springer Netherlands, p. 746.

Barker, D. M., W. Huang, Y.-R. Guo, A. J. Bourgeois, and Q. N. Xiao, 2004: A Three-Dimensional Variational Data Assimilation System for MM5: Implementation and Initial Results. *Mon. Weather Rev.*, **132**, 897–914, https://doi.org/10.1175/1520-0493(2004)132<0897:ATVDAS>2.0.CO;2.

Bauer, P., G. Ohring, C. Kummerow, and T. Auligne, 2011: Assimilating Satellite Observations of Clouds and Precipitation into NWP Models. *Bull. Am. Meteorol. Soc.*, **92**, ES25–ES28, https://doi.org/10.1175/2011BAMS3182.1.

Bei, N., and F. Zhang, 2007: Impacts of initial condition errors on mesoscale predictability of heavy precipitation along the Mei-Yu front of China. *Q. J. R. Meteorol. Soc.*, **133**, 83–99, https://doi.org/https://doi.org/10.1002/qj.20.

Bell, M. M., and M. T. Montgomery, 2019: Mesoscale Processes during the Genesis of Hurricane Karl (2010). *J. Atmos. Sci.*, **76**, 2235–2255, https://doi.org/10.1175/JAS-D-18-0161.1.

Berry, G. J., and C. D. Thorncroft, 2012: African Easterly Wave Dynamics in a Mesoscale Numerical Model: The Upscale Role of Convection. *J. Atmos. Sci.*, **69**, 1267–1283, https://doi.org/https://doi.org/10.1175/JAS-D-11-099.1.

Bister, M., and K. A. Emanuel, 1997: The Genesis of Hurricane Guillermo: TEXMEX Analyses and a Modeling Study. *Mon. Weather Rev.*, **125**, 2662–2682, https://doi.org/10.1175/1520-0493(1997)125<2662:TGOHGT>2.0.CO;2.

Brammer, A., and C. D. Thorncroft, 2015: Variability and Evolution of African Easterly Wave Structures and Their Relationship with Tropical Cyclogenesis over the Eastern Atlantic. *Mon. Weather Rev.*, **143**, 4975–4995, https://doi.org/https://doi.org/10.1175/MWR-D-15-0106.1.

——, ——, and J. P. Dunion, 2018: Observations and Predictability of a Nondeveloping Tropical Disturbance over the Eastern Atlantic. *Mon. Weather Rev.*, **146**, 3079–3096, https://doi.org/https://doi.org/10.1175/MWR-D-18-0065.1.

Braun, S. A., M. T. Montgomery, K. J. Mallen, and P. D. Reasor, 2010: Simulation and Interpretation of the Genesis of Tropical Storm Gert (2005) as Part of the NASA Tropical Cloud Systems and Processes Experiment. *J. Atmos. Sci.*, **67**, 999–1025, https://doi.org/10.1175/2009JAS3140.1.

——, and Coauthors, 2013: NASA's Genesis and Rapid Intensification Processes (GRIP) Field Experiment. *Bull. Am. Meteorol. Soc.*, **94**, 345–363, https://doi.org/10.1175/BAMS-D-11-00232.1.

Briegel, L. M., and W. M. Frank, 1997: Large-Scale Influences on Tropical Cyclogenesis in the Western North Pacific. *Mon. Weather Rev.*, **125**, 1397–1413, https://doi.org/10.1175/1520-0493(1997)125<1397:LSIOTC>2.0.CO;2.

Cangialosi, J. P., 2020: *National Hurricane Center Forecast Verification Report: 2019 Hurricane Season*. 75 pp. https://www.nhc.noaa.gov/verification/pdfs/Verification_2019.pdf.

——, A. S. Latto, and R. Berg, 2018: *National Hurricane Center Tropical Cyclone Report: Hurricane Irma (AL112017) 30 August-12 September 2017*. 111 pp. https://www.nhc.noaa.gov/data/tcr/AL112017_Irma.pdf.

Chan, M.-Y., and X. Chen, 2022: Improving the Analyses and Forecasts of a Tropical Squall

Line Using Upper Tropospheric Infrared Satellite Observations. *Adv. Atmos. Sci.*, **39**, 733–746, https://doi.org/10.1007/s00376-021-0449-8.
——, J. L. Anderson, and X. Chen, 2020a: An Efficient Bi-Gaussian Ensemble Kalman Filter for Satellite Infrared Radiance Data Assimilation. *Mon. Weather Rev.*, **148**, 5087–5104, https://doi.org/https://doi.org/10.1175/MWR-D-20-0142.1.
——, F. Zhang, X. Chen, and L. R. Leung, 2020b: Potential Impacts of Assimilating All-Sky Satellite Infrared Radiances on Convection-Permitting Analysis and Prediction of Tropical Convection. *Mon. Weather Rev.*, **148**, 3203–3224, https://doi.org/10.1175/MWR-D-19-0343.1.
Chang, M., C. H. Ho, M. S. Park, J. Kim, and M. H. Ahn, 2017: Multiday evolution of convective bursts during western North Pacific tropical cyclone development and nondevelopment using geostationary satellite measurements. *J. Geophys. Res.*, **122**, 1635–1649, https://doi.org/10.1002/2016JD025535.
Chen, X., and F. Zhang, 2019a: Relative Roles of Preconditioning Moistening and Global Circumnavigating Mode on the MJO Convective Initiation During DYNAMO. *Geophys. Res. Lett.*, **46**, 1079–1087, https://doi.org/10.1029/2018GL080987.
——, and ——, 2019b: Development of a Convection-Permitting Air-Sea-Coupled Ensemble Data Assimilation System for Tropical Cyclone Predictiont. *J. Adv. Model. Earth Syst.*, **11**, 3474– 3496, https://doi.org/10.1029/2019MS001795.
——, O. M. Pauluis, L. R. Leung, and F. Zhang, 2018a: Multiscale Atmospheric Overturning of the Indian Summer Monsoon as Seen through Isentropic Analysis. *J. Atmos. Sci.*, **75**, 3011–3030, https://doi.org/10.1175/JAS-D-18-0068.1.
——, ——, and F. Zhang, 2018b: Atmospheric Overturning across Multiple Scales of an MJO Event during the CINDY/DYNAMO Campaign. *J. Atmos. Sci.*, **75**, 381–399, https://doi.org/10.1175/JAS-D-17-0060.1.
——, L. R. Leung, Z. Feng, F. Song, and Q. Yang, 2021a: Mesoscale Convective Systems Dominate the Energetics of the South Asian Summer Monsoon Onset. *Geophys. Res. Lett.*, **48**, e2021GL094873, https://doi.org/10.1029/2021GL094873.
——, R. G. Nystrom, C. A. Davis, and C. M. Zarzycki, 2021b: Dynamical Structures of Cross-Domain Forecast Error Covariance of a Simulated Tropical Cyclone in a Convection-Permitting Coupled Atmosphere–Ocean Model. *Mon. Weather Rev.*, **149**, 41–63, https://doi.org/10.1175/MWR-D-20-0116.1.
——, L. R. Leung, Z. Feng, and F. Song, 2022a: Crucial Role of Mesoscale Convective Systems in the Vertical Mass, Water, and Energy Transports of the South Asian Summer Monsoon. *J. Clim.*, **35**, 91–108, https://doi.org/10.1175/JCLI-D-21-0124.1.
——, ——, ——, and Q. Yang, 2022b: Precipitation-Moisture Coupling Over Tropical Oceans: Sequential Roles of Shallow, Deep, and Mesoscale Convective Systems. *Geophys. Res. Lett.*, **49**, e2022GL097836, https://doi.org/10.1029/2022GL097836.
——, ——, ——, and ——, 2023: Diurnal MCSs Precede the Genesis of Tropical Cyclone Mora (2017): The Role of Convectively Forced Gravity Waves. *J. Atmos. Sci.*, **80**, 1463–1479, https://doi.org/https://doi.org/10.1175/JAS-D-22-0203.1.
Christophersen, H., A. Aksoy, J. Dunion, and K. Sellwood, 2017: The Impact of NASA Global Hawk Unmanned Aircraft Dropwindsonde Observations on Tropical Cyclone Track, Intensity, and Structure: Case Studies. *Mon. Weather Rev.*, **145**, 1817–1830, https://doi.org/https://doi.org/10.1175/MWR-D-16-0332.1.

Cione, J. J., and Coauthors, 2020: Eye of the Storm: Observing Hurricanes with a Small Unmanned Aircraft System. *Bull. Am. Meteorol. Soc.*, **101**, E186–E205, https://doi.org/https://doi.org/10.1175/BAMS-D-19-0169.1.

Corbosiero, K. L., and J. Molinari, 2002: The Effects of Vertical Wind Shear on the Distribution of Convection in Tropical Cyclones. *Mon. Weather Rev.*, **130**, 2110–2123, https://doi.org/https://doi.org/10.1175/1520-0493(2002)130<2110:TEOVWS>2.0.CO;2.

Craig, G. C., 1996: Numerical experiments on radiation and tropical cyclones. *Q. J. R. Meteorol. Soc.*, **122**, 415–422, https://doi.org/https://doi.org/10.1002/qj.49712253006.

DeHart, J. C., R. A. Houze, and R. F. Rogers, 2014: Quadrant Distribution of Tropical Cyclone Inner-Core Kinematics in Relation to Environmental Shear. *J. Atmos. Sci.*, **71**, 2713–2732, https://doi.org/https://doi.org/10.1175/JAS-D-13-0298.1.

DeMaria, M., J. A. Knaff, and B. H. Connell, 2001: A Tropical Cyclone Genesis Parameter for the Tropical Atlantic. *Weather Forecast.*, **16**, 219–233, https://doi.org/10.1175/1520-0434(2001)016<0219:ATCGPF>2.0.CO;2.

Desroziers, G., L. Berre, B. Chapnik, and P. Poli, 2005: Diagnosis of observation, background and analysis-error statistics in observation space. *Q. J. R. Meteorol. Soc.*, **131**, 3385–3396, https://doi.org/https://doi.org/10.1256/qj.05.108.

Doyle, J. D., C. A. Reynolds, C. Amerault, and J. Moskaitis, 2012: Adjoint Sensitivity and Predictability of Tropical Cyclogenesis. *J. Atmos. Sci.*, **69**, 3535–3557, https://doi.org/https://doi.org/10.1175/JAS-D-12-0110.1.

Dunion, J. P., C. D. Thorncroft, and D. S. Nolan, 2019: Tropical Cyclone Diurnal Cycle Signals in a Hurricane Nature Run. *Mon. Weather Rev.*, **147**, 363–388, https://doi.org/https://doi.org/10.1175/MWR-D-18-0130.1.

Dunkerton, T. J., M. T. Montgomery, and Z. Wang, 2009: Tropical cyclogenesis in a tropical wave critical layer: easterly waves. *Atmos. Chem. Phys.*, **9**, 5587–5646, https://doi.org/10.5194/acp-9-5587-2009.

Durran, D. R., and M. Gingrich, 2014: Atmospheric Predictability: Why Butterflies Are Not of Practical Importance. *J. Atmos. Sci.*, **71**, 2476–2488, https://doi.org/https://doi.org/10.1175/JAS-D-14-0007.1.

——, and J. A. Weyn, 2016: Thunderstorms Do Not Get Butterflies. *Bull. Am. Meteorol. Soc.*, **97**, 237–243, https://doi.org/https://doi.org/10.1175/BAMS-D-15-00070.1.

——, P. A. Reinecke, and J. D. Doyle, 2013: Large-Scale Errors and Mesoscale Predictability in Pacific Northwest Snowstorms. *J. Atmos. Sci.*, **70**, 1470–1487, https://doi.org/https://doi.org/10.1175/JAS-D-12-0202.1.

ECMWF, 2021: IFS Documentation CY47R3 - Part I: Observations. *IFS Documentation CY47R3*, *IFS Documentation*, ECMWF.

Emanuel, K., 2018: 100 Years of Progress in Tropical Cyclone Research. *Meteorol. Monogr.*, **59**, 15.1-15.68, https://doi.org/10.1175/AMSMONOGRAPHS-D-18-0016.1.

——, and F. Zhang, 2016: On the Predictability and Error Sources of Tropical Cyclone Intensity Forecasts. *J. Atmos. Sci.*, **73**, 3739–3747, https://doi.org/10.1175/JAS-D-16-0100.1.

——, and ——, 2017: The Role of Inner-Core Moisture in Tropical Cyclone Predictability and Practical Forecast Skill. *J. Atmos. Sci.*, **74**, 2315–2324, https://doi.org/10.1175/JAS-D-17-0008.1.

Evensen, G., 1994: Sequential data assimilation with a nonlinear quasi-geostrophic model using Monte Carlo methods to forecast error statistics. *J. Geophys. Res. Ocean.*, **99**, 10143–

10162, https://doi.org/https://doi.org/10.1029/94JC00572.
Eyre, J. R., 2016: Observation Bias Correction Schemes in Data Assimilation Systems: a Theoretical Study of Some of their Properties. *Q. J. R. Meteorol. Soc.*, **142**, 2284–2291, https://doi.org/https://doi.org/10.1002/qj.2819.
Fischer, M. S., P. D. Reasor, B. H. Tang, K. L. Corbosiero, R. D. Torn, and X. Chen, 2023: A Tale of Two Vortex Evolutions: Using a High-Resolution Ensemble to Assess the Impacts of Ventilation on a Tropical Cyclone Rapid Intensification Event. *Mon. Weather Rev.*, **151**, 297–320, https://doi.org/https://doi.org/10.1175/MWR-D-22-0037.1.
Gaspari, G., and S. E. Cohn, 1999: Construction of Correlation Functions in Two and Three Dimensions. *Q. J. R. Meteorol. Soc.*, **125**, 723–757, https://doi.org/10.1002/qj.49712555417.
Ge, X., Y. Ma, S. Zhou, and T. Li, 2014: Impacts of the diurnal cycle of radiation on tropical cyclone intensification and structure. *Adv. Atmos. Sci.*, **31**, 1377–1385, https://doi.org/10.1007/s00376-014-4060-0.
Geer, A. J., and P. Bauer, 2011: Observation Errors in All-Sky Data Assimilation. *Q. J. R. Meteorol. Soc.*, https://doi.org/10.1002/qj.830.
Geer, A. J., S. Migliorini, and M. Matricardi, 2019: All-Sky Assimilation of Infrared Radiances Sensitive to Mid- and Upper-Tropospheric Moisture and Cloud. *Atmos. Meas. Tech.*, **12**, 4903–4929, https://doi.org/http://dx.doi.org/10.5194/amt-12-4903-2019.
Gjorgjievska, S., and D. J. Raymond, 2014: Interaction between dynamics and thermodynamics during tropical cyclogenesis. *Atmos. Chem. Phys.*, **14**, 3065–3082, https://doi.org/10.5194/acp-14-3065-2014.
Gosset, W. S., 1908: The Probable Error of a Mean. *Biometrika*, **6 (1)**, 1–25, https://doi.org/10.1093/biomet/6.1.1.
Gray, W. M., 1968: Global View of the Origin of Tropical Disturbances and Storms. *Mon. Weather Rev.*, **96**, 669–700, https://doi.org/10.1175/1520-0493(1968)096<0669:gvotoo>2.0.co;2.
Green, B. W., and F. Zhang, 2013: Impacts of Air–Sea Flux Parameterizations on the Intensity and Structure of Tropical Cyclones. *Mon. Weather Rev.*, **141**, 2308–2324, https://doi.org/10.1175/MWR-D-12-00274.1.
——, and ——, 2014: Sensitivity of Tropical Cyclone Simulations to Parametric Uncertainties in Air–Sea Fluxes and Implications for Parameter Estimation. *Mon. Weather Rev.*, **142**, 2290–2308, https://doi.org/10.1175/MWR-D-13-00208.1.
Greybush, S. J., E. Kalnay, T. Miyoshi, K. Ide, and B. R. Hunt, 2011: Balance and Ensemble Kalman Filter Localization Techniques. *Mon. Weather Rev.*, **139**, 511–522, https://doi.org/10.1175/2010MWR3328.1.
Hall, N. M. J., G. N. Kiladis, and C. D. Thorncroft, 2006: Three-Dimensional Structure and Dynamics of African Easterly Waves. Part II: Dynamical Modes. *J. Atmos. Sci.*, **63**, 2231–2245, https://doi.org/https://doi.org/10.1175/JAS3742.1.
Halperin, D. J., H. E. Fuelberg, R. E. Hart, J. H. Cossuth, P. Sura, and R. J. Pasch, 2013: An Evaluation of Tropical Cyclone Genesis Forecasts from Global Numerical Models. *Weather Forecast.*, **28**, 1423–1445, https://doi.org/https://doi.org/10.1175/WAF-D-13-00008.1.
Han, Y., P. van Delst, Q. Liu, F. Weng, B. Yan, R. Treadon, and J. Derber, 2006: *JCSDA Community Radiative Transfer Model (CRTM) - Version 1. NOAA Tech. Rep. NESDIS 122*. 33 pp. https://repository.library.noaa.gov/view/noaa/1157.

——, F. Weng, Q. Liu, and P. van Delst, 2007: A Fast Radiative Transfer Model for SSMIS Upper Atmosphere Sounding Channels. *J. Geophys. Res.*, **112**, D11121, https://doi.org/10.1029/2006JD008208.

Hartman, C. M., X. Chen, E. E. Clothiaux, and M.-Y. Chan, 2021: Improving the Analysis and Forecast of Hurricane Dorian (2019) with Simultaneous Assimilation of GOES-16 All-Sky Infrared Brightness Temperatures and Tail Doppler Radar Radial Velocities. *Mon. Weather Rev.*, **149**, 2193–2212, https://doi.org/10.1175/MWR-D-20-0338.1.

——, ——, and M.-Y. Chan, 2023: Improving Tropical Cyclogenesis Forecasts of Hurricane Irma (2017) through the Assimilation of All-Sky Infrared Brightness Temperatures. *Mon. Weather Rev.*, **151**, 837–853, https://doi.org/https://doi.org/10.1175/MWR-D-22-0196.1.

He, J., and Coauthors, 2019: Development and Evaluation of an Ensemble-Based Data Assimilation System for Regional Reanalysis Over the Tibetan Plateau and Surrounding Regions. *J. Adv. Model. Earth Syst.*, **11**, 2503–2522, https://doi.org/10.1029/2019MS001665.

Hence, D. A., and R. A. Houze, 2011: Vertical Structure of Hurricane Eyewalls as Seen by the TRMM Precipitation Radar. *J. Atmos. Sci.*, **68**, 1637–1652, https://doi.org/https://doi.org/10.1175/2011JAS3578.1.

Hendricks, E. A., M. T. Montgomery, and C. A. Davis, 2004: The Role of "Vortical" Hot Towers in the Formation of Tropical Cyclone Diana (1984). *J. Atmos. Sci.*, **61**, 1209–1232, https://doi.org/10.1175/1520-0469(2004)061<1209:TROVHT>2.0.CO;2.

Hobgood, J. S., 1986: A Possible Mechanism for the Diurnal Oscillations of Tropical Cyclones. *J. Atmos. Sci.*, **43**, 2901–2922, https://doi.org/https://doi.org/10.1175/1520-0469(1986)043<2901:APMFTD>2.0.CO;2.

Honda, T., and Coauthors, 2018: Assimilating All-Sky Himawari-8 Satellite Infrared Radiances: A Case of Typhoon Soudelor (2015). *Mon. Weather Rev.*, **146**, 213–229, https://doi.org/10.1175/MWR-D-16-0357.1.

Hong, S.-Y., and J.-O. J. Lim, 2006: The WRF Single-Moment 6-Class Microphysics Scheme (WSM6). *J. Korean Meteorol. Soc.*, **42**, 129–151.

——, Y. Noh, and J. Dudhia, 2006: A New Vertical Diffusion Package with an Explicit Treatment of Entrainment Processes. *Mon. Weather Rev.*, **134**, 2318–2341, https://doi.org/10.1175/MWR3199.1.

Hopsch, S. B., C. D. Thorncroft, and K. R. Tyle, 2010: Analysis of African Easterly Wave Structures and Their Role in Influencing Tropical Cyclogenesis. *Mon. Weather Rev.*, **138**, 1399–1419, https://doi.org/https://doi.org/10.1175/2009MWR2760.1.

Hou, A. Y., and Coauthors, 2014: The Global Precipitation Measurement Mission. *Bull. Am. Meteorol. Soc.*, **95**, 701–722, https://doi.org/https://doi.org/10.1175/BAMS-D-13-00164.1.

Houtekamer, P. L., and H. L. Mitchell, 2001: A Sequential Ensemble Kalman Filter for Atmospheric Data Assimilation. *Mon. Weather Rev.*, **129**, 123–137, https://doi.org/https://doi.org/10.1175/1520-0493(2001)129<0123:ASEKFF>2.0.CO;2.

——, and ——, 2005: Ensemble Kalman Filtering. *Q. J. R. Meteorol. Soc.*, **131**, 3269–3289, https://doi.org/https://doi.org/10.1256/qj.05.135.

Houze, R. A., W.-C. Lee, and M. M. Bell, 2009: Convective Contribution to the Genesis of Hurricane Ophelia (2005). *Mon. Weather Rev.*, **137**, 2778–2800, https://doi.org/10.1175/2009MWR2727.1.

Iacono, M. J., J. S. Delamere, E. J. Mlawer, M. W. Shephard, S. A. Clough, and W. D. Collins,

2008: Radiative Forcing by Long-Lived Greenhouse Gases: Calculations with the AER Radiative Transfer Models. *J. Geophys. Res.*, **113**, D13103, https://doi.org/10.1029/2008JD009944.

Jacques, D., W. Chang, S.-J. Baek, T. Milewski, L. Fillion, K.-S. Chung, and H. Ritchie, 2017: Developing a Convective-Scale EnKF Data Assimilation System for the Canadian MEOPAR Project. *Mon. Weather Rev.*, **145**, 1473–1494, https://doi.org/https://doi.org/10.1175/MWR-D-16-0135.1.

Jones, S. C., 1995: The evolution of vortices in vertical shear. I: Initially barotropic vortices. *Q. J. R. Meteorol. Soc.*, **121**, 821–851, https://doi.org/https://doi.org/10.1002/qj.49712152406.

Jones, T. A., and Coauthors, 2020: Assimilation of GOES-16 Radiances and Retrievals into the Warn-on-Forecast System. *Mon. Weather Rev.*, **148**, 1829–1859, https://doi.org/10.1175/MWR-D-19-0379.1.

Judt, F., and S. S. Chen, 2016: Predictability and Dynamics of Tropical Cyclone Rapid Intensification Deduced from High-Resolution Stochastic Ensembles. *Mon. Weather Rev.*, **144**, 4395–4420, https://doi.org/https://doi.org/10.1175/MWR-D-15-0413.1.

Kaplan, J., and M. DeMaria, 2003: Large-Scale Characteristics of Rapidly Intensifying Tropical Cyclones in the North Atlantic Basin. *Weather Forecast.*, **18**, 1093–1108, https://doi.org/10.1175/1520-0434(2003)018<1093:LCORIT>2.0.CO;2.

Kerns, B. W., and S. S. Chen, 2013: Cloud Clusters and Tropical Cyclogenesis: Developing and Nondeveloping Systems and Their Large-Scale Environment. *Mon. Weather Rev.*, **141**, 192–210, https://doi.org/10.1175/MWR-D-11-00239.1.

Komaromi, W. A., 2013: An Investigation of Composite Dropsonde Profiles for Developing and Nondeveloping Tropical Waves during the 2010 PREDICT Field Campaign. *J. Atmos. Sci.*, **70**, 542–558, https://doi.org/https://doi.org/10.1175/JAS-D-12-052.1.

——, and S. J. Majumdar, 2015: Ensemble-Based Error and Predictability Metrics Associated with Tropical Cyclogenesis. Part II: Wave-Relative Framework. *Mon. Weather Rev.*, **143**, 1665–1686, https://doi.org/https://doi.org/10.1175/MWR-D-14-00286.1.

Kotsuki, S., S. J. Greybush, and T. Miyoshi, 2017: Can We Optimize the Assimilation Order in the Serial Ensemble Kalman Filter? A Study with the Lorenz-96 Model. *Mon. Weather Rev.*, **145**, 4977–4995, https://doi.org/https://doi.org/10.1175/MWR-D-17-0094.1.

Krishnamurti, T. N., S. Pattnaik, L. Stefanova, T. S. V. V. Kumar, B. P. Mackey, A. J. O'Shay, and R. J. Pasch, 2005: The Hurricane Intensity Issue. *Mon. Weather Rev.*, **133**, 1886–1912, https://doi.org/10.1175/MWR2954.1.

Lawton, Q. A., and S. J. Majumdar, 2023: Convectively Coupled Kelvin Waves and Tropical Cyclogenesis: Connections through Convection and Moisture. *Mon. Weather Rev.*, **151**, 1647–1666, https://doi.org/https://doi.org/10.1175/MWR-D-23-0005.1.

——, ——, K. Dotterer, C. Thorncroft, and C. J. Schreck, 2022: The Influence of Convectively Coupled Kelvin Waves on African Easterly Waves in a Wave-Following Framework. *Mon. Weather Rev.*, **150**, 2055–2072, https://doi.org/https://doi.org/10.1175/MWR-D-21-0321.1.

Lei, L., J. S. Whitaker, J. L. Anderson, and Z. Tan, 2020: Adaptive Localization for Satellite Radiance Observations in an Ensemble Kalman Filter. *J. Adv. Model. Earth Syst.*, **12**, e2019MS001693, https://doi.org/https://doi.org/10.1029/2019MS001693.

Leppert, K. D., D. J. Cecil, and W. A. Petersen, 2013a: Relation between Tropical Easterly Waves, Convection, and Tropical Cyclogenesis: A Lagrangian Perspective. *Mon. Weather Rev.*, **141**, 2649–2668, https://doi.org/10.1175/MWR-D-12-00217.1.

——, W. A. Petersen, and D. J. Cecil, 2013b: Electrically Active Convection in Tropical Easterly Waves and Implications for Tropical Cyclogenesis in the Atlantic and East Pacific. *Mon. Weather Rev.*, **141**, 542–556, https://doi.org/10.1175/MWR-D-12-00174.1.

Li, Z., and Z. Pu, 2014: Numerical Simulations of the Genesis of Typhoon Nuri (2008): Sensitivity to Initial Conditions and Implications for the Roles of Intense Convection and Moisture Conditions. *Weather Forecast.*, **29**, 1402–1424, https://doi.org/10.1175/WAF-D-14-00003.1.

Lloveras, D. J., D. R. Durran, and J. D. Doyle, 2023: The Two- to Four-Day Predictability of Midlatitude Cyclones: Don't Sweat the Small Stuff. *J. Atmos. Sci.*, **80**, 2613–2633, https://doi.org/https://doi.org/10.1175/JAS-D-22-0232.1.

Lorenz, E. N., 1969: The predictability of a flow which possesses many scales of motion. *Tellus*, **21**, 289–307, https://doi.org/10.3402/tellusa.v21i3.10086.

Majumdar, S. J., and R. D. Torn, 2014: Probabilistic Verification of Global and Mesoscale Ensemble Forecasts of Tropical Cyclogenesis. *Weather Forecast.*, **29**, 1181–1198, https://doi.org/10.1175/WAF-D-14-00028.1.

Melhauser, C., and F. Zhang, 2012: Practical and Intrinsic Predictability of Severe and Convective Weather at the Mesoscales. *J. Atmos. Sci.*, **69**, 3350–3371, https://doi.org/https://doi.org/10.1175/JAS-D-11-0315.1.

——, and ——, 2014: Diurnal Radiation Cycle Impact on the Pregenesis Environment of Hurricane Karl (2010). *J. Atmos. Sci.*, **71**, 1241–1259, https://doi.org/https://doi.org/10.1175/JAS-D-13-0116.1.

Meng, Z., and F. Zhang, 2008: Tests of an Ensemble Kalman Filter for Mesoscale and Regional-Scale Data Assimilation. Part III: Comparison with 3DVAR in a Real-Data Case Study. *Mon. Weather Rev.*, **136**, 522–540, https://doi.org/10.1175/2007MWR2106.1.

Minamide, M., and F. Zhang, 2017: Adaptive Observation Error Inflation for Assimilating All-Sky Satellite Radiance. *Mon. Weather Rev.*, https://doi.org/10.1175/MWR-D-16-0257.1.

——, and ——, 2018: Assimilation of All-Sky Infrared Radiances from Himawari-8 and Impacts of Moisture and Hydrometer Initialization on Convection-Permitting Tropical Cyclone Prediction. *Mon. Weather Rev.*, **146**, 3241–3258, https://doi.org/10.1175/MWR-D-17-0367.1.

——, and ——, 2019: An Adaptive Background Error Inflation Method for Assimilating All-Sky Radiances. *Q. J. R. Meteorol. Soc.*, https://doi.org/10.1002/qj.3466.

——, ——, and E. E. Clothiaux, 2020: Nonlinear Forecast Error Growth of Rapidly Intensifying Hurricane Harvey (2017) Examined through Convection-Permitting Ensemble Assimilation of GOES-16 All-Sky Radiances. *J. Atmos. Sci.*, **77**, 4277–4296, https://doi.org/10.1175/JAS-D-19-0279.1.

Montgomery, M. T., and J. Enagonio, 1998: Tropical Cyclogenesis via Convectively Forced Vortex Rossby Waves in a Three-Dimensional Quasigeostrophic Model. *J. Atmos. Sci.*, **55**, 3176–3207, https://doi.org/10.1175/1520-0469(1998)055<3176:TCVCFV>2.0.CO;2.

Montgomery, M. T., M. E. Nicholls, T. A. Cram, and A. B. Saunders, 2006: A Vortical Hot Tower Route to Tropical Cyclogenesis. *J. Atmos. Sci.*, **63**, 355–386, https://doi.org/10.1175/JAS3604.1.

——, L. L. Lussier III, R. W. Moore, and Z. Wang, 2010a: The genesis of Typhoon Nuri as observed during the Tropical Cyclone Structure 2008 (TCS-08) field experiment – Part 1: The role of the easterly wave critical layer. *Atmos. Chem. Phys.*, **10**, 9879–9900,

https://doi.org/10.5194/acp-10-9879-2010.
——, Z. Wang, and T. J. Dunkerton, 2010b: Coarse, intermediate and high resolution numerical simulations of the transition of a tropical wave critical layer to a tropical storm. *Atmos. Chem. Phys.*, **10**, 10803–10827, https://doi.org/10.5194/acp-10-10803-2010.
Montgomery, M. T., and Coauthors, 2012: The Pre-Depression Investigation of Cloud-Systems in the Tropics (PREDICT) Experiment: Scientific Basis, New Analysis Tools, and Some First Results. *Bull. Am. Meteorol. Soc.*, **93**, 153–172, https://doi.org/10.1175/BAMS-D-11-00046.1.
Neelin, J. D., O. Peters, and K. Hales, 2009: The Transition to Strong Convection. *J. Atmos. Sci.*, **66**, 2367–2384, https://doi.org/10.1175/2009JAS2962.1.
Nerger, L., 2015: On Serial Observation Processing in Localized Ensemble Kalman Filters. *Mon. Weather Rev.*, **143**, 1554–1567, https://doi.org/https://doi.org/10.1175/MWR-D-14-00182.1.
Nolan, D. S., 2007: What is the trigger for tropical cyclogenesis? *Aust. Meteor. Mag.*, **56**, 241–266.
Núñez Ocasio, K. M., 2021: Tropical Cyclogenesis and Its Relation to Interactions Between African Easterly Waves and Mesoscale Convective Systems. The Pennsylvania State University, 123 pp. https://ezaccess.libraries.psu.edu/login?qurl=https%3A%2F%2Fwww.proquest.com%2Fdissertations-theses%2Ftropical-cyclogenesis-relation-interactions%2Fdocview%2F2577531063%2Fse-2%3Faccountid%3D13158.
——, J. L. Evans, and G. S. Young, 2020: A Wave-Relative Framework Analysis of AEW–MCS Interactions Leading to Tropical Cyclogenesis. *Mon. Weather Rev.*, **148**, 4657–4671, https://doi.org/https://doi.org/10.1175/MWR-D-20-0152.1.
——, A. Brammer, J. L. Evans, G. S. Young, and Z. L. Moon, 2021: Favorable Monsoon Environment over Eastern Africa for Subsequent Tropical Cyclogenesis of African Easterly Waves. *J. Atmos. Sci.*, **78**, 2911–2925, https://doi.org/https://doi.org/10.1175/JAS-D-20-0339.1.
Nuss, W. A., and D. K. Miller, 2001: Mesoscale predictability under various synoptic regimes. *Nonlinear Process. Geophys.*, **8**, 429–438, https://doi.org/10.5194/npg-8-429-2001.
Nystrom, R. G., and F. Zhang, 2019: Practical Uncertainties in the Limited Predictability of the Record-Breaking Intensification of Hurricane Patricia (2015). *Mon. Weather Rev.*, **147**, 3535–3556, https://doi.org/10.1175/MWR-D-18-0450.1.
——, R. Rotunno, C. A. Davis, and F. Zhang, 2020: Consistent Impacts of Surface Enthalpy and Drag Coefficient Uncertainty between an Analytical Model and Simulated Tropical Cyclone Maximum Intensity and Storm Structure. *J. Atmos. Sci.*, **77**, 3059–3080, https://doi.org/10.1175/JAS-D-19-0357.1.
Osuri, K. K., U. C. Mohanty, A. Routray, and D. Niyogi, 2015: Improved Prediction of Bay of Bengal Tropical Cyclones through Assimilation of Doppler Weather Radar Observations. *Mon. Weather Rev.*, https://doi.org/10.1175/MWR-D-13-00381.1.
Otkin, J. A., and R. Potthast, 2019: Assimilation of All-Sky SEVIRI Infrared Brightness Temperatures in a Regional-Scale Ensemble Data Assimilation System. *Mon. Weather Rev.*, **147**, 4481–4509, https://doi.org/10.1175/MWR-D-19-0133.1.
Otkin, J. A., R. Potthast, and A. S. Lawless, 2018: Nonlinear Bias Correction for Satellite Data Assimilation Using Taylor Series Polynomials. *Mon. Weather Rev.*, **146**, 263–285, https://doi.org/https://doi.org/10.1175/MWR-D-17-0171.1.

Ou, T., D. Chen, X. Chen, C. Lin, K. Yang, H.-W. Lai, and F. Zhang, 2020: Simulation of summer precipitation diurnal cycles over the Tibetan Plateau at the gray-zone grid spacing for cumulus parameterization. *Clim. Dyn.*, **54**, 3525–3539, https://doi.org/10.1007/s00382-020-05181-x.

Pan, S., J. Gao, D. J. Stensrud, X. Wang, and T. A. Jones, 2018: Assimilation of Radar Radial Velocity and Reflectivity, Satellite Cloud Water Path, and Total Precipitable Water for Convective-Scale NWP in OSSEs. *J. Atmos. Ocean. Technol.*, **35**, 67–89, https://doi.org/https://doi.org/10.1175/JTECH-D-17-0081.1.

Peng, M. S., B. Fu, T. Li, and D. E. Stevens, 2012: Developing versus Nondeveloping Disturbances for Tropical Cyclone Formation. Part I: North Atlantic. *Mon. Weather Rev.*, **140**, 1047–1066, https://doi.org/https://doi.org/10.1175/2011MWR3617.1.

Poterjoy, J., and F. Zhang, 2014a: Predictability and Genesis of Hurricane Karl (2010) Examined through the EnKF Assimilation of Field Observations Collected during PREDICT. *J. Atmos. Sci.*, **71**, 1260–1275, https://doi.org/https://doi.org/10.1175/JAS-D-13-0291.1.

——, and ——, 2014b: Intercomparison and Coupling of Ensemble and Four-Dimensional Variational Data Assimilation Methods for the Analysis and Forecasting of Hurricane Karl (2010). *Mon. Weather Rev.*, **142**, 3347–3364, https://doi.org/https://doi.org/10.1175/MWR-D-13-00394.1.

Pu, Z., S. Zhang, M. Tong, and V. Tallapragada, 2016: Influence of the Self-Consistent Regional Ensemble Background Error Covariance on Hurricane Inner-Core Data Assimilation with the GSI-Based Hybrid System for HWRF. *J. Atmos. Sci.*, **73**, 4911–4925, https://doi.org/10.1175/JAS-D-16-0017.1.

Rajasree, V. P. M., A. P. Kesarkar, J. N. Bhate, V. Singh, U. Umakanth, and T. H. Varma, 2016a: A comparative study on the genesis of North Indian Ocean tropical cyclone Madi (2013) and Atlantic Ocean tropical cyclone Florence (2006). *J. Geophys. Res. Atmos.*, **121**, 13,813-826,858, https://doi.org/10.1002/2016JD025412.

——, ——, ——, U. Umakanth, V. Singh, and T. Harish Varma, 2016b: Appraisal of recent theories to understand cyclogenesis pathways of tropical cyclone Madi (2013). *J. Geophys. Res. Atmos.*, **121**, 8949–8982, https://doi.org/10.1002/2016JD025188.

Rajeswari, J. R., C. V Srinivas, P. R. Mohan, and B. Venkatraman, 2020: Impact of Boundary Layer Physics on Tropical Cyclone Simulations in the Bay of Bengal Using the WRF Model. *Pure Appl. Geophys.*, https://doi.org/10.1007/s00024-020-02572-3.

Raymond, D. J., S. L. Sessions, and C. López Carrillo, 2011: Thermodynamics of tropical cyclogenesis in the northwest Pacific. *J. Geophys. Res. Atmos.*, **116**, https://doi.org/https://doi.org/10.1029/2011JD015624.

Reasor, P. D., M. T. Montgomery, and L. F. Bosart, 2005: Mesoscale Observations of the Genesis of Hurricane Dolly (1996). *J. Atmos. Sci.*, **62**, 3151–3171, https://doi.org/10.1175/JAS3540.1.

——, R. Rogers, and S. Lorsolo, 2013: Environmental Flow Impacts on Tropical Cyclone Structure Diagnosed from Airborne Doppler Radar Composites. *Mon. Weather Rev.*, **141**, 2949–2969, https://doi.org/https://doi.org/10.1175/MWR-D-12-00334.1.

Reed, R. J., D. C. Norquist, and E. E. Recker, 1977: The Structure and Properties of African Wave Disturbances as Observed During Phase III of GATE. *Mon. Weather Rev.*, **105**, 317–333, https://doi.org/10.1175/1520-0493(1977)105<0317:TSAPOA>2.0.CO;2.

Ritchie, E. A., and G. J. Holland, 1997: Scale Interactions during the Formation of Typhoon

Irving. *Mon. Weather Rev.*, **125**, 1377–1396, https://doi.org/10.1175/1520-0493(1997)125<1377:SIDTFO>2.0.CO;2.
Romine, G. S., C. S. Schwartz, C. Snyder, J. L. Anderson, and M. L. Weisman, 2013: Model Bias in a Continuously Cycled Assimilation System and Its Influence on Convection-Permitting Forecasts. *Mon. Weather Rev.*, **141**, 1263–1284, https://doi.org/https://doi.org/10.1175/MWR-D-12-00112.1.
Rotunno, R., Y. Chen, W. Wang, C. Davis, J. Dudhia, and G. J. Holland, 2009: Large-Eddy Simulation of an Idealized Tropical Cyclone. *Bull. Am. Meteorol. Soc.*, **90**, 1783–1788, https://doi.org/10.1175/2009BAMS2884.1.
Ruppert, J. H., A. A. Wing, X. Tang, and E. L. Duran, 2020: The critical role of cloud–infrared radiation feedback in tropical cyclone development. *Proc. Natl. Acad. Sci.*, **117**, 27884–27892, https://doi.org/10.1073/pnas.2013584117.
Russell, J. O., A. Aiyyer, J. D. White, and W. Hannah, 2017: Revisiting the connection between African Easterly Waves and Atlantic tropical cyclogenesis. *Geophys. Res. Lett.*, **44**, 587–595, https://doi.org/10.1002/2016GL071236.
Russell, J. O. H., and A. Aiyyer, 2020: The Potential Vorticity Structure and Dynamics of African Easterly Waves. *J. Atmos. Sci.*, **77**, 871–890, https://doi.org/https://doi.org/10.1175/JAS-D-19-0019.1.
——, ——, and J. Dylan White, 2020: African Easterly Wave Dynamics in Convection-Permitting Simulations: Rotational Stratiform Instability as a Conceptual Model. *J. Adv. Model. Earth Syst.*, **12**, e2019MS001706, https://doi.org/https://doi.org/10.1029/2019MS001706.
Van Sang, N., R. K. Smith, and M. T. Montgomery, 2008: Tropical-cyclone intensification and predictability in three dimensions. *Q. J. R. Meteorol. Soc.*, **134**, 563–582, https://doi.org/10.1002/qj.235.
Sawada, Y., K. Okamoto, M. Kunii, and T. Miyoshi, 2019: Assimilating Every-10-minute Himawari-8 Infrared Radiances to Improve Convective Predictability. *J. Geophys. Res. Atmos.*, **124**, 2546–2561, https://doi.org/10.1029/2018JD029643.
Schecter, D. A., and D. H. E. Dubin, 1999: Vortex Motion Driven by a Background Vorticity Gradient. *Phys. Rev. Lett.*, **83**, 2191–2194, https://doi.org/10.1103/PhysRevLett.83.2191.
Schmid, J., 2000: The SEVIRI Instrument. *Proceedings of the 2000 EUMETSAT meteorological satellite data user's conference, Bologna, Italy*, 13–32.
Schmit, T. J., M. M. Gunshor, W. P. Menzel, J. J. Gurka, J. Li, and A. S. Bachmeier, 2005: Introducing the Next-Generation Advanced Baseline Imager on GOES-R. *Bull. Am. Meteorol. Soc.*, **86**, 1079–1096, https://doi.org/10.1175/BAMS-86-8-1079.
Schreck, C. J., 2015: Kelvin Waves and Tropical Cyclogenesis: A Global Survey. *Mon. Weather Rev.*, **143**, 3996–4011, https://doi.org/https://doi.org/10.1175/MWR-D-15-0111.1.
——, 2016: Convectively Coupled Kelvin Waves and Tropical Cyclogenesis in a Semi-Lagrangian Framework. *Mon. Weather Rev.*, **144**, 4131–4139, https://doi.org/https://doi.org/10.1175/MWR-D-16-0237.1.
Schwartz, C. S., G. S. Romine, R. A. Sobash, K. R. Fossell, and M. L. Weisman, 2015: NCAR's Experimental Real-Time Convection-Allowing Ensemble Prediction System. *Weather Forecast.*, **30**, 1645–1654, https://doi.org/https://doi.org/10.1175/WAF-D-15-0103.1.
Sellwood, K. J., J. A. Sippel, and A. Aksoy, 2023: Assimilation of Coyote Small Uncrewed Aircraft System Observations in Hurricane Maria (2017) Using Operational HWRF.

Weather Forecast., **38**, 901–919, https://doi.org/https://doi.org/10.1175/WAF-D-22-0214.1.
Selz, T., and G. C. Craig, 2015: Upscale Error Growth in a High-Resolution Simulation of a Summertime Weather Event over Europe. *Mon. Weather Rev.*, **143**, 813–827, https://doi.org/https://doi.org/10.1175/MWR-D-14-00140.1.
Shen, F., J. Min, and D. Xu, 2016: Assimilation of Radar Radial Velocity Data with the WRF Hybrid ETKF–3DVAR System for the Prediction of Hurricane Ike (2008). *Atmos. Res.*, **169**, 127–138, https://doi.org/https://doi.org/10.1016/j.atmosres.2015.09.019.
——, D. Xu, J. Min, Z. Chu, and X. Li, 2020: Assimilation of Radar Radial Velocity Data with the WRF Hybrid 4DEnVar System for the Prediction of Hurricane Ike (2008). *Atmos. Res.*, **234**, 104771, https://doi.org/https://doi.org/10.1016/j.atmosres.2019.104771.
Shin, S., and R. K. Smith, 2008: Tropical-cyclone intensification and predictability in a minimal three-dimensional model. *Q. J. R. Meteorol. Soc.*, **134**, 1661–1671, https://doi.org/10.1002/qj.327.
Sieron, S. B., E. E. Clothiaux, F. Zhang, Y. Lu, and J. A. Otkin, 2017: Comparison of using distribution-specific versus effective radius methods for hydrometeor single-scattering properties for all-sky microwave satellite radiance simulations with different microphysics parameterization schemes. *J. Geophys. Res. Atmos.*, **122**, 7027–7046, https://doi.org/https://doi.org/10.1002/2017JD026494.
——, F. Zhang, E. E. Clothiaux, L. N. Zhang, and Y. Lu, 2018: Representing Precipitation Ice Species With Both Spherical and Nonspherical Particles for Radiative Transfer Modeling of Microphysics-Consistent Cloud Microwave Scattering Properties. *J. Adv. Model. Earth Syst.*, **10**, 1011–1028, https://doi.org/https://doi.org/10.1002/2017MS001226.
Simpson, J., E. Ritchie, G. J. Holland, J. Halverson, and S. Stewart, 1997: Mesoscale Interactions in Tropical Cyclone Genesis. *Mon. Weather Rev.*, **125**, 2643–2661, https://doi.org/10.1175/1520-0493(1997)125<2643:MIITCG>2.0.CO;2.
Sippel, J. A., and F. Zhang, 2008: A Probabilistic Analysis of the Dynamics and Predictability of Tropical Cyclogenesis. *J. Atmos. Sci.*, **65**, 3440–3459, https://doi.org/https://doi.org/10.1175/2008JAS2597.1.
——, and ——, 2010: Factors Affecting the Predictability of Hurricane Humberto (2007). *J. Atmos. Sci.*, **67**, 1759–1778, https://doi.org/https://doi.org/10.1175/2010JAS3172.1.
——, J. W. Nielsen-Gammon, and S. E. Allen, 2006: The Multiple-Vortex Nature of Tropical Cyclogenesis. *Mon. Weather Rev.*, **134**, 1796–1814, https://doi.org/10.1175/MWR3165.1.
——, S. A. Braun, and C.-L. Shie, 2011: Environmental Influences on the Strength of Tropical Storm Debby (2006). *J. Atmos. Sci.*, **68**, 2557–2581, https://doi.org/https://doi.org/10.1175/2011JAS3648.1.
Skamarock, W. C., J. B. Klemp, J. Dudhia, D. O. Gill, D. Barker, M. G. Duda, and J. G. Powers, 2008: A Description of the Advanced Research WRF Version 3 (No. NCAR/TN-475+STR). University Corporation for Atmospheric Research. https://doi.org/10.5065/D68S4MVH.
Skofronick-Jackson, G., and Coauthors, 2017: The Global Precipitation Measurement (GPM) Mission for Science and Society. *Bull. Am. Meteorol. Soc.*, **98**, 1679–1695, https://doi.org/https://doi.org/10.1175/BAMS-D-15-00306.1.
Smith, A. B., 2020: U.S. Billion-dollar Weather and Climate Disasters, 1980 - Present (NCEI Accession 0209268). *NOAA Natl. Centers Environ. Inf.*, Dataset, https://doi.org/10.25921/stkw-7w73.

Smith, R. K., and M. T. Montgomery, 2012: Observations of the convective environment in developing and non-developing tropical disturbances. *Quart. J. Roy. Meteor. Soc.,*.
Snyder, C., and F. Zhang, 2003: Assimilation of Simulated Doppler Radar Observations with an Ensemble Kalman Filter. *Mon. Weather Rev.*, **131**, 1663–1677, https://doi.org/https://doi.org/10.1175//2555.1.
Sun, Y. Q., and F. Zhang, 2016: Intrinsic versus Practical Limits of Atmospheric Predictability and the Significance of the Butterfly Effect. *J. Atmos. Sci.*, **73**, 1419–1438, https://doi.org/https://doi.org/10.1175/JAS-D-15-0142.1.
Surcel, M., I. Zawadzki, and M. K. Yau, 2015: A Study on the Scale Dependence of the Predictability of Precipitation Patterns. *J. Atmos. Sci.*, **72**, 216–235, https://doi.org/https://doi.org/10.1175/JAS-D-14-0071.1.
Tan, Z.-M., F. Zhang, R. Rotunno, and C. Snyder, 2004: Mesoscale Predictability of Moist Baroclinic Waves: Experiments with Parameterized Convection. *J. Atmos. Sci.*, **61**, 1794–1804, https://doi.org/https://doi.org/10.1175/1520-0469(2004)061<1794:MPOMBW>2.0.CO;2.
Tang, B. H., and Coauthors, 2020: Recent advances in research on tropical cyclogenesis. *Trop. Cyclone Res. Rev.*, **9**, 87–105, https://doi.org/10.1016/j.tcrr.2020.04.004.
Tang, X., and F. Zhang, 2016: Impacts of the Diurnal Radiation Cycle on the Formation, Intensity, and Structure of Hurricane Edouard (2014). *J. Atmos. Sci.*, **73**, 2871–2892, https://doi.org/https://doi.org/10.1175/JAS-D-15-0283.1.
Tao, D., and F. Zhang, 2014: Effect of environmental shear, sea-surface temperature, and ambient moisture on the formation and predictability of tropical cyclones: An ensemble-mean perspective. *J. Adv. Model. Earth Syst.*, **6**, 384–404, https://doi.org/https://doi.org/10.1002/2014MS000314.
——, and ——, 2015: Effects of vertical wind shear on the predictability of tropical cyclones: Practical versus intrinsic limit. *J. Adv. Model. Earth Syst.*, **7**, 1534–1553, https://doi.org/https://doi.org/10.1002/2015MS000474.
Tarantola, A., 1987: *Inverse Problem Theory*. Elsevier, 613 pp.
Taraphdar, S., P. Mukhopadhyay, L. R. Leung, F. Zhang, S. Abhilash, and B. N. Goswami, 2014: The role of moist processes in the intrinsic predictability of Indian Ocean cyclones. *J. Geophys. Res. Atmos.*, **119**, 8032–8048, https://doi.org/https://doi.org/10.1002/2013JD021265.
Thompson, G., P. R. Field, R. M. Rasmussen, and W. D. Hall, 2008: Explicit Forecasts of Winter Precipitation Using an Improved Bulk Microphysics Scheme. Part II: Implementation of a New Snow Parameterization. *Mon. Weather Rev.*, **136**, 5095–5115, https://doi.org/10.1175/2008MWR2387.1.
Thompson, T. E., L. J. Wicker, X. Wang, and C. Potvin, 2015: A Comparison between the Local Ensemble Transform Kalman Filter and the Ensemble Square Root Filter for the Assimilation of Radar Data in Convective-scale Models. *Q. J. R. Meteorol. Soc.*, **141**, 1163–1176, https://doi.org/https://doi.org/10.1002/qj.2423.
Tiedtke, M., 1989: A Comprehensive Mass Flux Scheme for Cumulus Parameterization in Large-Scale Models. *Mon. Weather Rev.*, **117**, 1779–1800, https://doi.org/10.1175/1520-0493(1989)117<1779:ACMFSF>2.0.CO;2.
Tong, M., and Coauthors, 2018: Impact of Assimilating Aircraft Reconnaissance Observations on Tropical Cyclone Initialization and Prediction Using Operational HWRF and GSI

Ensemble–Variational Hybrid Data Assimilation. *Mon. Weather Rev.*, **146**, 4155–4177, https://doi.org/10.1175/MWR-D-17-0380.1.
Torn, R. D., 2010: Ensemble-Based Sensitivity Analysis Applied to African Easterly Waves. *Weather Forecast.*, **25**, 61–78, https://doi.org/https://doi.org/10.1175/2009WAF2222255.1.
——, and D. Cook, 2013: The Role of Vortex and Environment Errors in Genesis Forecasts of Hurricanes Danielle and Karl (2010). *Mon. Weather Rev.*, **141**, 232–251, https://doi.org/https://doi.org/10.1175/MWR-D-12-00086.1.
Tory, K. J., M. T. Montgomery, and N. E. Davidson, 2006a: Prediction and Diagnosis of Tropical Cyclone Formation in an NWP System. Part I: The Critical Role of Vortex Enhancement in Deep Convection. *J. Atmos. Sci.*, **63**, 3077–3090, https://doi.org/10.1175/JAS3764.1.
——, ——, ——, and J. D. Kepert, 2006b: Prediction and Diagnosis of Tropical Cyclone Formation in an NWP System. Part II: A Diagnosis of Tropical Cyclone Chris Formation. *J. Atmos. Sci.*, **63**, 3091–3113, https://doi.org/10.1175/JAS3765.1.
Uhlhorn, E. W., and P. G. Black, 2003: Verification of Remotely Sensed Sea Surface Winds in Hurricanes. *J. Atmos. Ocean. Technol.*, **20**, 99–116, https://doi.org/10.1175/1520-0426(2003)020<0099:VORSSS>2.0.CO;2.
Ventrice, M. J., C. D. Thorncroft, and M. A. Janiga, 2012a: Atlantic Tropical Cyclogenesis: A Three-Way Interaction between an African Easterly Wave, Diurnally Varying Convection, and a Convectively Coupled Atmospheric Kelvin Wave. *Mon. Weather Rev.*, **140**, 1108–1124, https://doi.org/https://doi.org/10.1175/MWR-D-11-00122.1.
——, ——, and C. J. Schreck, 2012b: Impacts of Convectively Coupled Kelvin Waves on Environmental Conditions for Atlantic Tropical Cyclogenesis. *Mon. Weather Rev.*, **140**, 2198–2214, https://doi.org/https://doi.org/10.1175/MWR-D-11-00305.1.
Wang, C., L. Lei, Z.-M. Tan, and K. Chu, 2020: Adaptive Localization for Tropical Cyclones With Satellite Radiances in an Ensemble Kalman Filter. *Front. Earth Sci.*, **8**, https://doi.org/10.3389/feart.2020.00039.
Wang, S., A. H. Sobel, F. Zhang, Y. Q. Sun, Y. Yue, and L. Zhou, 2015: Regional Simulation of the October and November MJO Events Observed during the CINDY/DYNAMO Field Campaign at Gray Zone Resolution. *J. Clim.*, **28**, 2097–2119, https://doi.org/10.1175/JCLI-D-14-00294.1.
Wang, Z., 2012: Thermodynamic Aspects of Tropical Cyclone Formation. *J. Atmos. Sci.*, **69**, 2433–2451, https://doi.org/10.1175/JAS-D-11-0298.1.
——, 2018: What is the Key Feature of Convection Leading up to Tropical Cyclone Formation? *J. Atmos. Sci.*, **75**, 1609–1629, https://doi.org/10.1175/JAS-D-17-0131.1.
——, M. T. Montgomery, and T. J. Dunkerton, 2010: Genesis of Pre–Hurricane Felix (2007). Part I: The Role of the Easterly Wave Critical Layer. *J. Atmos. Sci.*, **67**, 1711–1729, https://doi.org/10.1175/2009JAS3420.1.
Weng, F., 2007: Advances in Radiative Transfer Modeling in Support of Satellite Data Assimilation. *J. Atmos. Sci.*, **64**, 3799–3807, https://doi.org/10.1175/2007JAS2112.1.
Weng, Y., and F. Zhang, 2012: Assimilating Airborne Doppler Radar Observations with an Ensemble Kalman Filter for Convection-Permitting Hurricane Initialization and Prediction: Katrina (2005). *Mon. Weather Rev.*, **140**, 841–859, https://doi.org/10.1175/2011MWR3602.1.
——, and ——, 2016: Advances in Convection-Permitting Tropical Cyclone Analysis and

Prediction through EnKF Assimilation of Reconnaissance Aircraft Observations. *J. Meteorol. Soc. Japan*, **94**, 345–358, https://doi.org/10.2151/jmsj.2016-018.
Whitaker, J. S., and T. M. Hamill, 2002: Ensemble Data Assimilation without Perturbed Observations. *Mon. Weather Rev.*, **130**, 1913–1924, https://doi.org/10.1175/1520-0493(2002)130<1913:EDAWPO>2.0.CO;2.
Wing, A. A., 2022: Acceleration of Tropical Cyclone Development by Cloud-Radiative Feedbacks. *J. Atmos. Sci.*, **79**, 2285–2305, https://doi.org/https://doi.org/10.1175/JAS-D-21-0227.1.
Ying, Y., and F. Zhang, 2017: Practical and Intrinsic Predictability of Multiscale Weather and Convectively Coupled Equatorial Waves during the Active Phase of an MJO. *J. Atmos. Sci.*, **74**, 3771–3785, https://doi.org/10.1175/JAS-D-17-0157.1.
——, and ——, 2018: Potentials in Improving Predictability of Multiscale Tropical Weather Systems Evaluated through Ensemble Assimilation of Simulated Satellite-Based Observations. *J. Atmos. Sci.*, **75**, 1675–1698, https://doi.org/10.1175/JAS-D-17-0245.1.
Zawislak, J., and E. J. Zipser, 2014: A Multisatellite Investigation of the Convective Properties of Developing and Nondeveloping Tropical Disturbances. *Mon. Weather Rev.*, **142**, 4624–4645, https://doi.org/10.1175/MWR-D-14-00028.1.
——, and Coauthors, 2022: Accomplishments of NOAA's Airborne Hurricane Field Program and a Broader Future Approach to Forecast Improvement. *Bull. Am. Meteorol. Soc.*, **103**, E311–E338, https://doi.org/https://doi.org/10.1175/BAMS-D-20-0174.1.
Zhang, F., and J. A. Sippel, 2009: Effects of Moist Convection on Hurricane Predictability. *J. Atmos. Sci.*, **66**, 1944–1961, https://doi.org/https://doi.org/10.1175/2009JAS2824.1.
——, and D. Tao, 2013: Effects of Vertical Wind Shear on the Predictability of Tropical Cyclones. *J. Atmos. Sci.*, **70**, 975–983, https://doi.org/https://doi.org/10.1175/JAS-D-12-0133.1.
——, and Y. Weng, 2015: Predicting Hurricane Intensity and Associated Hazards: A Five-Year Real-Time Forecast Experiment with Assimilation of Airborne Doppler Radar Observations. *Bull. Am. Meteorol. Soc.*, **96**, 25–33, https://doi.org/10.1175/BAMS-D-13-00231.1.
Zhang, F., C. Snyder, and R. Rotunno, 2002: Mesoscale Predictability of the "Surprise" Snowstorm of 24–25 January 2000. *Mon. Weather Rev.*, **130**, 1617–1632, https://doi.org/https://doi.org/10.1175/1520-0493(2002)130<1617:MPOTSS>2.0.CO;2.
——, ——, and ——, 2003: Effects of Moist Convection on Mesoscale Predictability. *J. Atmos. Sci.*, **60**, 1173–1185, https://doi.org/https://doi.org/10.1175/1520-0469(2003)060<1173:EOMCOM>2.0.CO;2.
——, ——, and J. Sun, 2004: Impacts of Initial Estimate and Observation Availability on Convective-Scale Data Assimilation with an Ensemble Kalman Filter. *Mon. Weather Rev.*, **132**, 1238–1253, https://doi.org/10.1175/1520-0493(2004)132<1238:IOIEAO>2.0.CO;2.
Zhang, F., A. M. Odins, and J. W. Nielsen-Gammon, 2006: Mesoscale Predictability of an Extreme Warm-Season Precipitation Event. *Weather Forecast.*, **21**, 149–166, https://doi.org/https://doi.org/10.1175/WAF909.1.
——, N. Bei, R. Rotunno, C. Snyder, and C. C. Epifanio, 2007: Mesoscale Predictability of Moist Baroclinic Waves: Convection-Permitting Experiments and Multistage Error Growth Dynamics. *J. Atmos. Sci.*, **64**, 3579–3594, https://doi.org/https://doi.org/10.1175/JAS4028.1.
——, Y. Weng, J. A. Sippel, Z. Meng, and C. H. Bishop, 2009: Cloud-Resolving Hurricane

Initialization and Prediction through Assimilation of Doppler Radar Observations with an Ensemble Kalman Filter. *Mon. Weather Rev.*, **137**, 2105–2125, https://doi.org/10.1175/2009MWR2645.1.

——, ——, J. F. Gamache, and F. D. Marks, 2011: Performance of Convection-Permitting Hurricane Initialization and Prediction during 2008–2010 with Ensemble Data Assimilation of Inner-Core Airborne Doppler Radar Observations. *Geophys. Res. Lett.*, **38**, L15810, https://doi.org/https://doi.org/10.1029/2011GL048469.

——, M. Minamide, and E. E. Clothiaux, 2016: Potential Impacts of Assimilating All-Sky Infrared Satellite Radiances from GOES-R on Convection-Permitting Analysis and Prediction of Tropical Cyclones. *Geophys. Res. Lett.*, https://doi.org/10.1002/2016GL068468.

——, S. Taraphdar, and S. Wang, 2017a: The role of global circumnavigating mode in the MJO initiation and propagation. *J. Geophys. Res. Atmos.*, **122**, 5837–5856, https://doi.org/https://doi.org/10.1002/2016JD025665.

——, M. Minamide, R. G. Nystrom, X. Chen, S.-J. Lin, and L. M. Harris, 2019a: Improving Harvey Forecasts with Next-Generation Weather Satellites: Advanced Hurricane Analysis and Prediction with Assimilation of GOES-R All-Sky Radiances. *Bull. Am. Meteorol. Soc.*, **100**, 1217–1222, https://doi.org/10.1175/BAMS-D-18-0149.1.

Zhang, J. A., 2018: *Evaluating the Impact of Model Physics on HWRF Forecasts of Tropical Cyclone Rapid Intensification*. 16 pp. https://dtcenter.org/sites/default/files/visitor-projects/DTC_project_final_report_JunZhang-final.pdf.

——, R. F. Rogers, and V. Tallapragada, 2017b: Impact of Parameterized Boundary Layer Structure on Tropical Cyclone Rapid Intensification Forecasts in HWRF. *Mon. Weather Rev.*, **145**, 1413–1426, https://doi.org/10.1175/MWR-D-16-0129.1.

Zhang, Y., F. Zhang, D. J. Stensrud, and Z. Meng, 2015: Practical Predictability of the 20 May 2013 Tornadic Thunderstorm Event in Oklahoma: Sensitivity to Synoptic Timing and Topographical Influence. *Mon. Weather Rev.*, **143**, 2973–2997, https://doi.org/https://doi.org/10.1175/MWR-D-14-00394.1.

——, ——, and D. J. Stensrud, 2018: Assimilating All-Sky Infrared Radiances from GOES-16 ABI Using an Ensemble Kalman Filter for Convection-Allowing Severe Thunderstorms Prediction. *Mon. Weather Rev.*, **146**, 3363–3381, https://doi.org/10.1175/MWR-D-18-0062.1.

——, D. J. Stensrud, and F. Zhang, 2019b: Simultaneous Assimilation of Radar and All-Sky Satellite Infrared Radiance Observations for Convection-Allowing Ensemble Analysis and Prediction of Severe Thunderstorms. *Mon. Weather Rev.*, **147**, 4389–4409, https://doi.org/https://doi.org/10.1175/MWR-D-19-0163.1.

——, and Coauthors, 2021a: Ensemble-Based Assimilation of Satellite All-Sky Microwave Radiances Improves Intensity and Rainfall Predictions for Hurricane Harvey (2017). *Geophys. Res. Lett.*, **48**, e2021GL096410, https://doi.org/10.1029/2021GL096410.

——, D. J. Stensrud, and E. E. Clothiaux, 2021b: Benefits of the Advanced Baseline Imager (ABI) for Ensemble-Based Analysis and Prediction of Severe Thunderstorms. *Mon. Weather Rev.*, **149**, 313–332, https://doi.org/10.1175/MWR-D-20-0254.1.

——, E. E. Clothiaux, and D. J. Stensrud, 2022: Correlation Structures between Satellite All-Sky Infrared Brightness Temperatures and the Atmospheric State at Storm Scales. *Adv. Atmos. Sci.*, **39**, 714–732, https://doi.org/10.1007/s00376-021-0352-3.

Zhu, L., and Coauthors, 2015: Prediction and Predictability of High-Impact Western Pacific Landfalling Tropical Cyclone Vicente (2012) through Convection-Permitting Ensemble Assimilation of Doppler Radar Velocity. *Mon. Weather Rev.*, **144**, 21–43, https://doi.org/10.1175/MWR-D-14-00403.1.

VITA

Christopher Hartman

Education:

Doctor of Science in Meteorology and Atmospheric Science,
The Pennsylvania State University, May 2024

Master of Education in Curriculum and Instruction,
The Pennsylvania State University, May 2006

Master of Science in Meteorology,
The Pennsylvania State University, May 2003

Bachelor of Science in Meteorology with a Mathematics Minor,
The Pennsylvania State University, May 2003

First-authored Publications:

Hartman, C.M., F. Judt, and X. Chen (*under review*): Influence of Local Water Vapor Analysis Uncertainty on Ensemble Forecasts of Tropical Cyclogenesis Using Hurricane Irma (2017) as a Testbed. *Mon. Weather Rev.*

Hartman, C.M., X. Chen, and M.-Y. Chan, 2023: Improving Tropical Cyclogenesis Forecasts of Hurricane Irma (2017) through the Assimilation of All-Sky Infrared Brightness Temperatures. *Mon. Weather Rev.*, **151**, 837-859, https://doi.org/10.1175/MWR-D-22-0196.1.

Hartman, C.M., X. Chen, E.E. Clothiaux, and M.-Y. Chan, 2021: Improving the Analysis and Forecast of Hurricane Dorian (2019) with Simultaneous Assimilation of *GOES-16* All-Sky Infrared Brightness Temperatures and Tail Doppler Radar Radial Velocities. *Mon. Weather Rev.*, **149**, 2193-2212, https://doi.org/10.1175/MWR-D-20-0338.1.

Hartman, C.M., and J.Y. Harrington, 2005: Radiative Impacts on the Growth of Drops within Simulated Marine Stratocumulus. Part I: Maximum Solar Heating. *J. Atmos. Sci.***, 62**, 2323-2338, https://doi.org/10.1175/JAS3477.1.

Hartman, C.M., and J.Y. Harrington, 2005: Radiative Impacts on the Growth of Drops within Simulated Marine Stratocumulus. Part II: Solar Zenith Angle Variations. *J. Atmos. Sci.*, **62**, 2339-2351, https://doi.org/10.1175/JAS3478.1.